Scuola Normale Superiore

Nanoscience PhD Program

Academic Year 2022/2023

Ph.D. Thesis

Photodetectors at Terahertz frequencies based on one-dimensional and two-dimensional nano systems

Candidate

Mahdi Asgari

Supervisor

Prof. Miriam Serena Vitiello

Contents

Introduction

Terahertz (THz) frequency radiation, loosely defined in the 0.1 – 10 THz range (wavelength 3 mm – 30 μm), falls in a broadly investigated gap of the electromagnetic (EM) spectrum, in between the range of interest of electronic and photonic devices. This frequency range lacks the variety of sources and detectors systems that are available in other regions of EM spectrum, such as the microwave, the visible and the infrared.

Terahertz-frequency technology has become of large interest over the last years since THz rays are nonionizing and provide considerable advantages for many appealing imaging applications if compared to sub-THz frequency radiation, mainly the possibility to detect substance-specific spectroscopic features and a sub-millimeter diffraction-limited lateral resolution. In this context, the development of a breakthrough solid-state technology for fast, room-temperature, THz detectors integrated in high-speed multipixel arrays is highly desired. Several approaches have been followed so far to develop THz and sub-THz detection systems. Among them, bolometric systems display the best detectivity and can reach high modulation bandwidths (superconducting hot-electron bolometers), but at the cost of deep cryogenic cooling. On the other hand, high-temperature THz detectors are either not very sensitive, or extremely slow, or operate well only at frequencies lower than ∼1 THz. Matrix arrays technologies are even more complex to implement [1]. Commercial THz focal plane arrays are presently based on microbolometer elements and provide moderate sensitivities and response speed. From a technological point of view, Schottky diodes [2] are the prototypical electronic components for room-temperature detection of high-frequency radiation. The operating principle exploits the nonlinearity and asymmetry of the current−voltage characteristic to generate, through rectification, a continuous signal out of the oscillating incident electromagnetic field. Despite this simple idea, practical implementations are often sophisticated, since electric transport in the device must be able to “follow” the radiation frequency, requiring minimization of the RC time constant. State-of-the-art technologies are based on vertical transport, featuring metallic air-bridges for contacting. However, these structures are typically delicate and very demanding for array geometries. Furthermore, performances drop rapidly with frequency above 1 THz. More recently, fast electronic devices, based on the gate modulation of the conductance channel by the incoming radiation, have been realized in both high-electron-mobility transistors (HEMT) [3], field-effect transistors (FET) [4], and complementary metal-oxide semiconductors (CMOS) [5] architectures and show fast response times in the gigahertz range [6].These technologies, in principle easily scalable to even large arrays, are still limited by detection cut-off frequencies of few hundred gigahertz, above which responsivity drops and cryogenics are required. The operating mechanism of a HEMT or a FET detector is not trivial [1], but it can intuitively be interpreted as deriving from the nonlinear dependence of the FET channel current on the gate voltage at the pinch-off point. These devices have the advantage that the responsivity can be maximized with the gate bias, while measuring the output at the drain with no source − drain bias applied, thus dramatically improving the signal-to-noise ratio.

To reply to the present need of highly sensitive (NEP $\leq$ 1nWHz$^{-1/2}$), and fast (response time $\leq$ 1nS) photodetectors operating in the 0.3-4 THz range, the present thesis focuses on the study of interaction between THz frequency radiation and different systems based on one dimensional (1D) or bi-dimensional (2D) nanomaterials, such as InAs nanowires (NWs) and InAs/InAsP heterostructure quantum dot (QD) NWs or large area single layer graphene (SLG) and layered van der Waals heterostructure of SLG and hexagonal boron nitride (hBN), grown by chemical vapor deposition (CVD), all embedded in antenna coupled FET for the efficient detection of THz frequency light.

The present thesis is organized as follows:

- In **chapter 1**, a general introduction of generation and detection mechanisms in the far-infrared is provided, with introduction on the basics of light detection. The different types of photodetectors are described, together the main figures of merit characterizing their performances. In the final part, the comparison between different types of detectors is made and detectors exploiting field effect transistor (FET) architectures are introduced.
- In **chapter 2**, the main physical principle controlling the photodetection dynamics in a FET-based photodetector are discussed, such as plasma wave oscillation (PWO), photovoltaic effect (PV), photo-thermoelectric effect (PTE), and bolometric effect (BE).
- **Chapter 3**, focuses on the development of large area graphene photodetectors (GPDs) and other two-dimensional van der Waals heterostructures-based photodetectors grown by chemical vapour deposition (CVD), engineered to work as low noise, fast, zero bias, zero dark current and room-temperature PTE THz photodetectors.
- **Chapter 4,** is dedicated to state-of-the-art characterization methods for FET THz detector based on InAs nanowires (NWs) via scattering type scanning

near field optical microscopy (s-SNOM) which in turn yields to be an appropriate approach for devising several design architectures that allow to selectively activate PTE or BE for THz detection.

- In **chapter 5,** I will report on the first demonstration of quantum dot nanowires (QD NWs) InAs/InAsP single electron transistors (SET) as highly sensitive low temperature THz detector. A full discussion on a proposed PTE model for transport and THz photodetection in QD SET is made.
- **Chapter 6** focuses on the initial experimental tests for double photon detection in a QD in a NW, at THz frequencies.

Finally, a perspective and conclusion session highlights the future developments expected in this vibrant research field, and the follow-up goals of the work performed in the present thesis.

Chapter 1: THz detectors

1.1. THz range

The ‘terahertz (THz) gap’ is conventionally identified as the region of the electromagnetic spectrum with frequencies lying above the microwaves and below infrared (considered from 0.1 THz to 10 THz), which correspond to wavelengths of 3 mm to 30 μm respectively) [7]. The ‘gap’ refers to the relative technological underdevelopment of devices operating in this spectral region, in contrast to the sophisticated electronic and optical technologies available in the regions that bracket it (figure 1.1). Present technologies for THz sources include electronic and photonic devices. The limits of these technologies in the 0.1-10 THz range are [8] are discussed in the paragraphs below.

- Limitations to the Electronic Approach: a fundamental limit is set by the speed at which electrons move. There comes a point when the electrons do not travel far enough for a device to work before the polarity of the voltage changes and the electrons change direction. In addition, high frequency alternating fields cause unwanted resistances and capacitances that reduce device power. Technological limits also include miniaturisation (for instance the size of antenna is matched with the wavelength of the generated electromagnetic radiation, hence decreasing wavelengths has required ever smaller devices) and the need to dissipate the heat that is generated by rapidly oscillating electrons.
- Limitations to the photonic approach: Photons at THz frequencies are emitted via electronic intersubband transitions that take place entirely within the conduction band, where the wavelength is chosen by engineering the well and barrier widths in multiple-quantum-well heterostructures. Fabrication of such long wavelength lasers has traditionally been challenging, since it is difficult to obtain a population inversion between such closely spaced energy levels, and because traditional dielectric waveguides become extremely lossy due to free carrier absorption.

1.2. Sources

Microwave sources usually rely on electronic devices. Present radio architectures contain downconverters that translate a RF or microwave frequency band down to an intermediate frequency for baseband processing. Regardless of the end application, whether it is communications, aerospace and defence, or instrumentation, the frequencies of interest are pushing higher into the RF and microwave spectrum [9].

Sources based on harmonic generation are characterized by a medium having a substantial nonlinear susceptibility [10] followed by one or more stages of harmonic generation can reach frequencies of hundreds of gigahertz. Each stage of harmonic generation comes with an efficiency penalty, thus at high frequencies the total available power and the efficiency are low and metal waveguides are lossy. Integration with waveguides are being explored [11], although long-distance transmission will be limited by the finite conductivity of metals and the absorption coefficient of dielectric materials. The tuning range of each harmonic generation chain (less important for communications applications than for spectroscopy applications) is usually limited to about a 20% bandwidth. The leader in commercial development is Virginia Diodes, Inc. (Charlottesville, Virginia), which has offered sources based on microwave harmonic generation chains that reach 1.2 THz [12].

Vacuum tube technologies, developed for radio and microwave applications, have been extended to the THz frequency range using micromachining techniques [12]. Amongst the most performing tubes there is the backward wave oscillator (BWO), so named because the direction of radiation amplification is opposite to the direction in which the electron beam travels. The disadvantages of BWOs include the need for a large external magnetic field, for a highly stable high-voltage power supply, and, since it cannot be directly modulated, for a separate high-speed THz modulator or mixer.

Resonant tunnelling diodes (RTDs) are another kind of available sources. They rely on a resonant-tunneling structure in which electrons can tunnel through some resonant states at certain energy levels. The current–voltage characteristic often exhibits negative differential resistance region, causing the diode to “resonate” and produce waves in the THz band (hundreds of gigahertz (GHz)) [13]. The main disadvantage of RTDs is their frequency limitation in THz and sub-THz regime [14].

The post powerful THz frequency source developed to date is the quantum cascade laser (QCL). QCLs require a very sophisticated fabrication process of several quantum wells (QWs). Electrons cascade from localized states in wells, and as they fall from one well to the next, a THz photon is then emitted. Lasing action is indeed achieved through intersubband transition in the conduction band of semiconductor heterostructures [15] which form multiple QWs, along with suitable optical feedback, provided by an optical waveguide. So far, THz QCLs could achieve maximum operating temperature of 250 K in pulsed mode [16] and 150 K in continuous-wave (CW) mode [17], an output power of 2 W [18], intrinsic linewidth of 90 Hz [19], frequency tunability of around 20% of central frequency [20], octave spanning/1.9 THz [21], and can have a spectral coverage of 1.2 THz – 5.9 THz [22]. Moreover, the advantages of QCLs include high brilliance, large quantum efficiencies, and compact size. Active development aims to reduce the disadvantages: the need of cooling, the limited tuning range and high unit costs.

In summary, the viable sources of terahertz radiation are [23,24]: the gyrotron, the backward wave oscillator (“BWO”), the far infrared laser (“fir laser”), quantum cascade laser, the free electron laser (FEL), synchrotron light sources, photomixing sources, single-cycle sources used in terahertz time domain spectroscopy such as photoconductive, surface field, photo-Dember and optical rectification emitters.

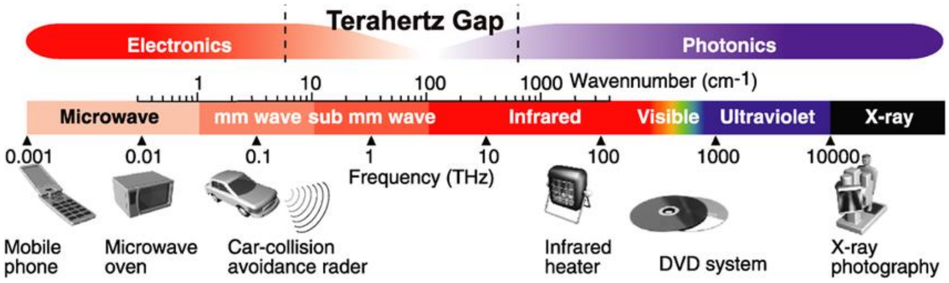

Figure 1.1: THz gap, a simple schematic of THz frequency domain (roughly considered from 0.1 THz to 10 THz) along entire spectrum range [25].

The field of THz science and technology has expanded exponentially over the last decades [7] with enormous progresses over the microwave regime. This is due to the several advantageous properties of THz radiation [26,27] over the microwave regime.

- Penetration: THz radiation can pass through the different media with different levels of the attenuation. In fact, the most important THz transparent materials which are widely used in the optical applications are: (1) Crystals such as silicon, quartz, sapphire, and diamonds, and (2) Polymers such as TPX (polymethylpentene), polyethylene (PE), and polytetrafluoroethylene (PTFE or Teflon).
- Safety: Because of the relatively low energy, THz waves produce negligible ionization effect on biological tissues, and thus they cause less detrimental impact on human body than higher energetic wave in the spectrum such as x-ray and ultraviolet [28].
- Spectroscopy: Various solid and gaseous materials present spectroscopic fingerprints in the 0.5–3 THz range, therefore THz waves can be used for material identification and for probing vibrational, rotational and roto-vibrational transitions in atoms and molecules.
- Resolution: as the resolution of an image will increase with a reduction in the wavelength of the wave, the resolution in the THz domain is better than that of the microwave band of the spectrum.
- Scattering: since the scattering is reciprocally proportional to the wavelength, wave dissipation is lower in the THz band as compared to visible light.

1.3. Photodetectors

A photodetector is a device capable to convert an optical signal into an electrical signal. THz photodetectors are sensitive to the THz frequency light and enables the detection via an electrical signal as an output (figure 1.2).

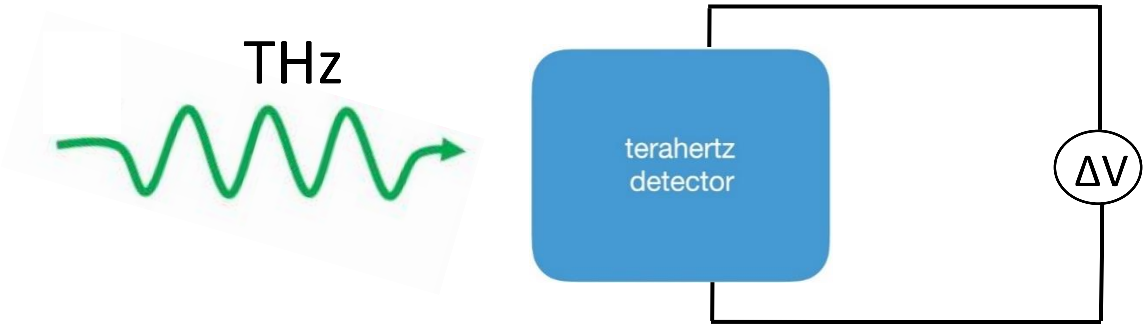

Figure 1.2**:** THz detector: transducer that converts THz radiation into a photovoltage or photocurrent.

1.3.1. Coherent and incoherent detectors

THz frequency receivers can be divided into two categories [29]:

- incoherent detection systems (with direct[1] detectors), that allow only the signal amplitude detection and have, as a rule, broadband detection nature (figure. 1.3(a)). As an example, a subcategory in the class of direct detectors is represented by thermal detectors.
- coherent detection systems, which allow detecting not only the amplitude of the signal, but also its phase (figure 1.3(b)). In fact, in such devices the detection of light is realized in a non-linear medium, by being able to mix two impinging light signals, of which one is the "local oscillator".

Direct photodetectors (also known as *square-law detectors* [30]) respond to the power or intensity, rather than the field amplitude, of an optical signal. In a square-law detector, the electrical signal generated by an optical signal is either a photocurrent or a photovoltage that is proportional to the power of the optical signal. In imaging applications where phase information is not necessary, the incoherent approach is advantageous owing to its compactness and simplicity. In the coherent detection scheme, since the amplitude of the generated signal depends on the relative phase between source and local oscillator (which are detuned slightly as respect to each other), a time domain reconstruction of the impinging fields can be realized. This comes at the price of a very complicated setup, and a more demanding data analysis with respect to incoherent direct detection schemes. Moreover, coherent signal detection systems rely on heterodyne circuit design, as shown in figure 1.3b. The detected signals are transferred to much lower electronic frequencies (intermediate Frequency (IF), typically from 1 GHz to 30 GHz) where they are amplified by low-noise amplifiers. These systems are selective (narrow-band) detection systems [1].

---

[1] A direct detector is a system based on detecting modulated optical power (also referred to as the optical field intensity or simply the optical intensity) [31].

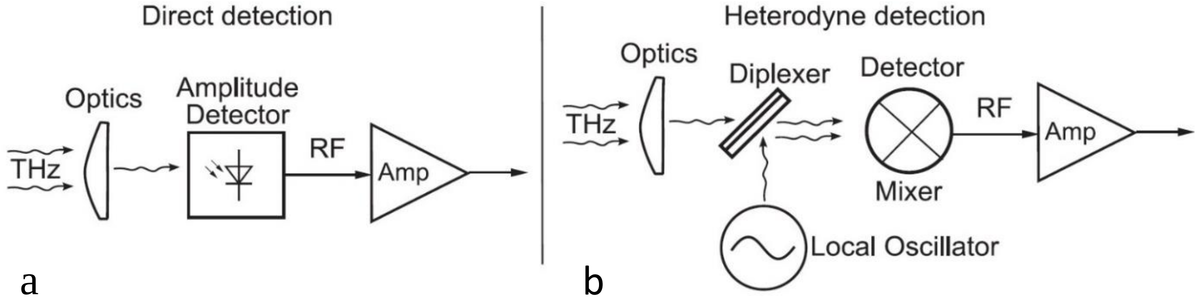

Figure 1.3: a) Incoherent detection system. b) Coherent detection system. IF is the intermediate frequency signal.

1.4. Figures of merit

The first characteristic of a THz detector is the sensitivity to photons of THz frequencies. A detector, operating at THz frequencies, is usually described in terms of THz frequencies to which it responds. Essentially, the detector will be more responsive to some frequencies than others, and not responsive to frequencies outside the detector optical bandwidth. The operating frequency range is also conventionally named as spectral range, or frequency bandwidth. If detector discerns photons of different frequencies, then this ability of the detector to do so is described by the frequency resolution. Detectors that do not distinguish photons of different frequencies may be coupled with a frequency-selective component (such as a diffraction grating). In general, a broad frequency response is desirable, even though in some applications (like refractive index sensing application [31]) a detector which responds only to a narrow frequency band is sufficient or even desirable. The different figures of merit can be then classified as follows:

- Responsivity: the responsivity defines the ratio between magnitude of the output signal and the power of the input signal. Thus, a voltage responsivity is defined as:

$$R_v = \frac{dV}{dP} \tag{1.1}$$

where V is photovoltage and P is optical input power into the detector.

Alternatively, the output may be a current, I (expressed in amperes). The current responsivity is defined as:

$$R_I = \frac{dI}{dP} \tag{1.2}$$

In general, large responsivities are desired. Furthermore, responsivity is often cited as a single figure, which supposes that the relationship between output and input is constant, which is, $dV/dP = V/P$ (or $dI/dP = I/P$). If such a relationship holds, which means the ratio between the output electrical signal and the input optical power does not depend on the size of the input, the detector has a linear behaviour. In specific cases a detector will either become more responsive (superlinear) or less responsive (sublinear) as the terahertz power incident on it increases.

- Noise equivalent power (*NEP*): It quantifies the background noise of the detector through an equivalent impinging light power. *NEP* is a measure of the sensitivity of a photodetector . It is defined as the signal power that gives a unitary signal-to-noise ratio (*SNR*) in one hertz output bandwidth [32]. The units of *NEP* are watts per square root hertz.

  In principle, noise is an inherent characteristic of electronic devices and then also detection systems. In photodetectors, noise can arise from the optical source, the detector element, and amplification circuit. The main noise sources are:

  - Johnson Noise: Johnson Noise (also known as thermal noise or Nyquist noise) results from the thermal motion of charged particles in a resistive element [33]. This is the most common noise source in electronics and is present in all conductors. The only parameters in an electronic system within the designer's control that influence Johnson noise are the resistance, the bandwidth, and the temperature. The noise generated has no relation to the type of conductor – equal value carbon composition and metal film resistors make the same noise contribution. The following equations are used for calculating Johnson noise.

$$P_J\left(rms\right) = k_B T\ \Delta f \tag{1.3}$$

$$V_J\left(rms\right) = \sqrt{4k_B TR\ \Delta f} \tag{1.4}$$

$$I_J\left(rms\right) = \sqrt{\frac{4k_B T\ \Delta f}{R}} \tag{1.5}$$

    where P_J *(rms)*, V_J *(rms)*, and I_J *(rms)* are Johnson noise power, voltage, and current respectively, k_B is the Boltzmann constant, T is the temperature, R is the resistance, and Δf is the effective noise bandwidth. Johnson noise is "white noise" meaning that it is frequency independent. The amplitude of Johnson noise has a zero mean Gaussian distribution, and it is therefore difficult to be directly measured owing to the internal noise in voltmeter or oscilloscope. However, it can be measured in the presence of gain i.e. in an amplifier.

- Shot Noise: Shot noise results from the flow of current across a potential barrier [34]. This is a statistical effect of the random emission of electrons (and holes) or the production of photoelectrons. It is found in vacuum tubes, transistors, and diodes. Shot noise is given by:

$$I_{Sh}(rms) = \sqrt{2qI_{DC}\Delta f} \tag{1.6}$$

I_{DC} can be due to the signal, bias currents, background radiation (photodetectors [35]), and leakage. Like thermal noise, the shot noise is proportional to $(\Delta f)^{1/2}$ meaning that there is constant noise power per Hz bandwidth, i.e.

-1/*f* Noise*:* Also referred to as contact noise (when found in detectors), excess noise (resistors), or flicker noise (vacuum tubes). It has been measured at frequencies as low as 6×10^{-5} Hz (~ 5 cycles/day). Note that while noise density approaches infinity, total noise does not because the decades keep getting narrower. If an amplifier is 1/*f* noise limited, measurement accuracy cannot be improved by increasing the length of the measurement (averaging); conversely, with white noise, the precision increases with the square-root of the measurement time. In detectors, it is usually related to the quality of the ohmic contacts and surfaces states. It also appears in composition-type resistors, carbon microphones, switch and relay contacts, transistors, and diodes and therefore all amplifiers. The equations vary depending on how the noise was modelled for the application. For a detector we have:

$$I_{RMS} = \kappa\sqrt{\frac{i_b^{\alpha}}{f^{\beta}}} \tag{1.7}$$

where κ is proportionality constant, i_b current through detector, f is frequency, α typically equal to 2, and $\beta \sim 1$. While 1/*f* noise is often ignored in noise computations where the system bandwidths are high, it is the dominant noise source in low-frequency applications.

- Generation-recombination noise: This noise is due to the fluctuations in current carrier generation and recombination. It normally occurs in photoconductors.

$$I_{G-R\,RMS} = 2e_0G(\eta E_p\ A\ \Delta f)^{1/2} \tag{1.8}$$

where G is photoconductive gain, e_0 is elementary charge, η is quantum efficiency, E_p is photon irradiance, and A is detector area.

- Detectivity: For a detector of area A and spectral bandwidth Δf, the detectivity is defined as:

$$D^* = \sqrt{A\Delta f} \,/\, NEP \tag{1.9}$$

  The larger the photodetector detectivity, more suitable it is for revealing weak signals, that compete with the detector noise.
- Electrical bandwidth: the electrical bandwidth of a detector accounts for the detector ability to follow time changes in the optical signal. It is usually quantified as a maximum operating frequency of the detector in pulsed mode, f_{max}. The frequency f_{max} is strongly dependent on the physics of the single detector system, and can be limited by several factors, such as: thermal time constant in the case of thermal detectors, RC circuital time constant in general, and carrier recombination lifetime in photoconductors. It accounts for the rate of modulation at which a detector can respond to, and is obtained through the relation [36]:

$$f_{\max} = \frac{1}{2\pi\tau} \tag{1.10}$$

  where τ is the detector’s time constant. The modulation bandwidth refers to the range of modulation frequencies to which a given detector can correspond (and should be distinguished from the spectral bandwidth of terahertz photon frequencies to which the detector responds).
- External and internal quantum efficiencies: the external quantum efficiency, EQE, is the ratio between the number of photo-induced charges collected per second divided by the number of incident photon per second: $EQE = (PC/e_0)/\phi$, where e_0 represents the elementary charge and ϕ is the photon flux. The internal quantum efficiency, IQE, is calculated by considering the number of photons absorbed: $IQE = (PC/e_0)/\phi_{abs}$.
- Polarization: a detector might be inherently sensitive to the polarization of the terahertz incoming photons. For example, the detector may detect all photons polarized in the horizontal plane but not those polarized in the vertical plane. As a further characteristic, some detectors have a polarization sensitivity that varies with frequency.

In addition to the figures of merit, there are also other important parameters to be taken into consideration for the assessment of a detector such as power requirement and cost effectiveness. Typically, detectors can operate from normal general power outlets. However, some might require more involved supplies (for instance, three-phase or high-current supply) and others only need something simpler (e.g. battery operation). Most essentially, the power consumption of a detector matters. In fact, the less power-consuming the detectors are, the more preferred and commercially versatile they are. Moreover, one of the most significant feasible considerations is the cost of ownership: both the cost to produce or to purchase the detector in the first place and the cost to run or to maintain the detector over its lifetime.

1.5. Architectures for far-infrared photodetectors

Electromagnetic radiation conventionally impinges on a detector element from the free space. Appropriate coupling structures (antennas) should be designed and fabricated to funnel millimetre and sub-millimetre radiations to the subwavelength-sized (~1μm) detector element.

THz frequency photodetectors can be classified in thermal detectors, electronic detectors, and quantum-engineered detectors.

- Thermal detectors absorb the radiation, their temperature is enhanced, and consequently provide an output electrical signal. There are several types of them, defined according to the physical mechanism that converts the temperature changes to a resultant electrical signal. **Golay cells** are room-temperature detectors made of a gas-filled chamber that varies its volume according to the incident radiation (the heating process). These type of detectors provide high sensitivity ($\sim$ 0.2 nW/$\sqrt{}$Hz) [37] over the THz range, but they have the disadvantages of being fragile and having a slow response ($\tau \sim$ 1ms) [37]. **Pyroelectric detectors** are made of materials that change their dielectric constant as a function of the temperature of the active absorbing element (like $LiTiO_3$, TGS crystal, and $NaNO_2$ [38]) which increases with an incident radiation. Besides working at room temperature, pyroelectric detectors offer an advantage of being small, portable, and less expensive than Golay cells [37]. On the other hand, they still have a slow response time (≥10μs) [39], which hampers possible applications. In bolometers, the incident radiation power is absorbed directly by free carriers, the crystal lattice temperature remaining essentially constant. Note that this mechanism differs from photoconductivity. For instance, in hot electron bolometer, the free-electron mobility is changed rather than electron number is created by incident light, as it is held for the photoconductivity. However, in both cases the detector resistance is changed [40]. **Semiconductor microbolometers** have shown the sensitivity of $\sim$ 30 pW/$\sqrt{}$Hz and τ $\sim$ 30ms in room temperature [41]. However, their performances in the low temperature can be improved compared to room temperature devices as the resistance changes are larger at low temperatures, and the heat capacity are substantially smaller at temperatures lower than the

Debye temperature Θ_D [37]. Present performances are $NEP \sim 10^{-16}$ W/$\sqrt{\text{Hz}}$ and $\tau \sim$ 11ms at T = 300 mK [42].

- Electronic detectors can usually be applied for both direct and heterodyne detection. Schottky barrier diodes (SBD) are the most used semiconductor devices in coherent (heterodyne) systems operating at frequencies above 0.5 THz. The main reason is that the nonlinear current-voltage characteristics depend (to the first order) only on majority carrier transport; hence, recombination rates are irrelevant to determine of the high-frequency cut-off [43]. As a result, temperature has only a minor effect on the SBD properties, allowing it to work at room temperature – a relevant feature for applications [44]. The nonlinear properties derive from electrons crossing a single metal/semiconductor interface; therefore, the SBD displays very low-capacitance [45]. The SBD detectors are usually single pixel detectors [46]. However, recently CMOS implementations have been successfully done including on-chip signal amplification and compact (up to 1000 pixels) arrays [47]. A promising approach is the use of field-effect transistors (FETs) as THz power detectors with frequencies higher than the typical FET cut-off frequency, achieving THz values in deep-submicron transistors. More details are given in the next section.
- Quantum detectors exploit quantum confinement of individual electrons. They usually consist of multiple semiconductor structures, which form wells or dots, where the electron is confined restricting its energy to discrete levels (energy sub-bands) [48]. The most developed technologies are quantum well infrared photodetectors (QWIPs) and quantum dot infrared photodetectors (QDIPs), respectively. In these kind of detectors, the detection mechanism is intrinsically narrow-band as determined by the confined structure parameters; but by adjusting the intersubband transition energy a wide frequency range might be spanned [44]. Furthermore, short carrier lifetime (~ 5ps) [49] means the detection can potentially be very fast. However, the applicability of such approach in the THz region is hindered by the small photon energies involved which also constrain their operation at cryogenic temperatures. [29].

A summary of the state-of-the-art THz detectors is shown in Table 1.1, through the comparison of their operation frequency and noise equivalent power. Furthermore, different types of detectors are discussed in details in Ref. [29,40].

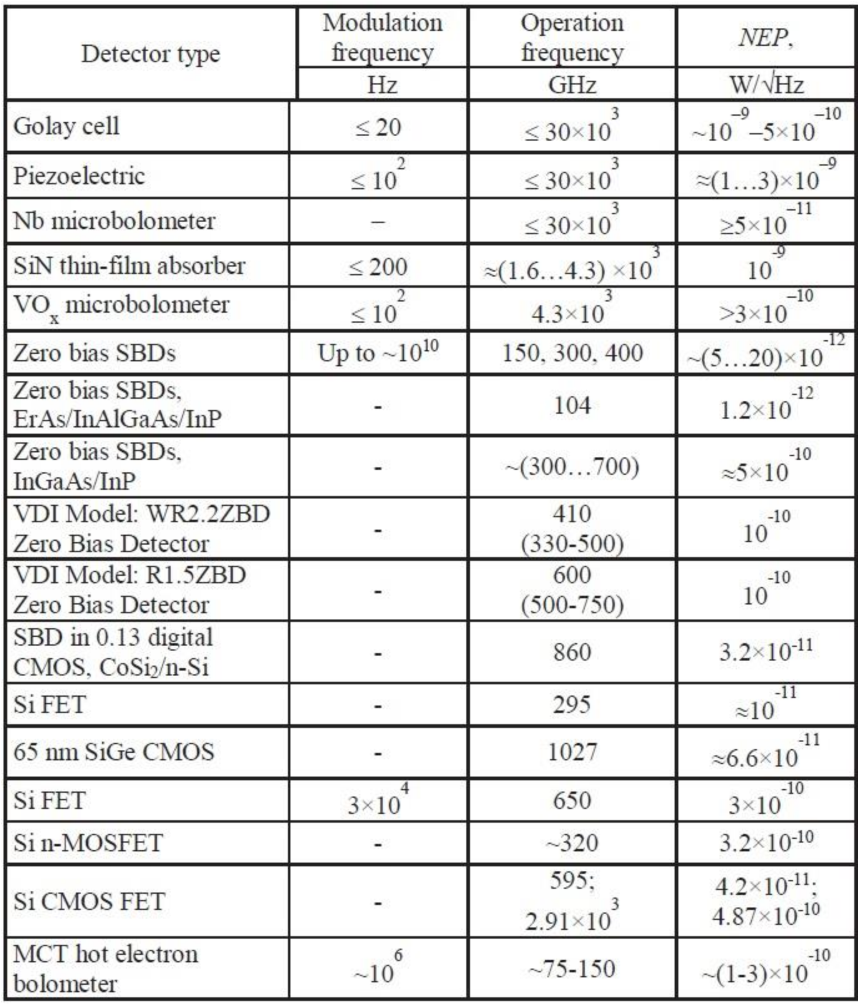

Detector type	Modulation frequency	Operation frequency	NEP,
	Hz	GHz	W/√Hz
Golay cell	≤ 20	$\leq 30\times10^{3}$	$\sim10^{-9}-5\times10^{-10}$
Piezoelectric	$\leq 10^{2}$	$\leq 30\times10^{3}$	$\approx(1\ldots3)\times10^{-9}$
Nb microbolometer	–	$\leq 30\times10^{3}$	$\geq5\times10^{-11}$
SiN thin-film absorber	≤ 200	$\approx(1.6\ldots4.3)\times10^{3}$	10^{-9}
VO_x microbolometer	$\leq 10^{2}$	4.3×10^{3}	$>3\times10^{-10}$
Zero bias SBDs	Up to $\sim10^{10}$	150, 300, 400	$\sim(5\ldots20)\times10^{-12}$
Zero bias SBDs, ErAs/InAlGaAs/InP	-	104	1.2×10^{-12}
Zero bias SBDs, InGaAs/InP	-	~(300…700)	$\approx5\times10^{-10}$
VDI Model: WR2.2ZBD Zero Bias Detector	-	410 (330-500)	10^{-10}
VDI Model: R1.5ZBD Zero Bias Detector	-	600 (500-750)	10^{-10}
SBD in 0.13 digital CMOS, $CoSi_2$/n-Si	-	860	3.2×10^{-11}
Si FET	-	295	$\approx10^{-11}$
65 nm SiGe CMOS	-	1027	$\approx6.6\times10^{-11}$
Si FET	3×10^{4}	650	3×10^{-10}
Si n-MOSFET	-	~320	3.2×10^{-10}
Si CMOS FET	-	595; 2.91×10^{3}	4.2×10^{-11}; 4.87×10^{-10}
MCT hot electron bolometer	$\sim10^{6}$	~75-150	$\sim(1\text{-}3)\times10^{-10}$

Table 1.1: Comparison of the detection performances of the most common uncooled direct detectors [50].

1.6. Field effect transistors

The theory of plasma wave oscillation for THz detection in field-effect transistors (FETs) was initially proposed by Dyakonov-Shur [8]. When THz radiation is coupled between gate and source of a FET, the THz alternating current (*AC)* voltage modulates simultaneously carrier density and carrier drift velocity. THz *AC* signal is then rectified and leads to a direct current (*DC)* photoresponse between source and drain (it is worth noting that the related physics of nonlinear rectification will be described in the second chapter where I also discuss the FETs as efficient photothermoelectric and bolometric detectors in THz regime, and then unveil several physical dynamics that will be further considered in this thesis). For high carrier mobility devices (III–V devices at cryogenic temperatures), the THz field can induce plasma waves which propagate in the channel and resonant plasma modes can be excited yielding to the voltage tunable detection [51,52].

At room temperature, THz radiation can lead to a carrier density perturbation that decays exponentially with the distance from the source with a characteristic length L_0 which is normally of the order of a few tens of nanometers [53].

At room temperature, the broadband detection process can be alternatively described by the model of distributed resistive self-mixing [54,55]. Even though not treating all plasma related physics rigorously, the resistive mixing model allows a rather reliable detector design [54].

Furthermore, in a FET detector photoresponse exhibits sensitivity to radiation helicity [56] making FETs promising tools for the all-electric detection of the radiation Stokes parameters.

In a FET several physical dynamics of photodetection can play a role as plasma wave oscillation (PWO), photovoltaic effect (PV), photo-thermoelectric effect (PTE), and bolometric effect (BE) in FET based THz photodetectors and will be further discussed in the next chapter.

Chapter 2: Physical dynamics in THz photodetectors based on FETs

2.1. Introduction

The conversion of absorbed photons into an electrical signal is the key process through which a photodetector operates. This process is driven by the excess energy contained in the electronic system. The photodetection mechanisms in FETs operating in THz regime are usually divided into different classes, depending to the fact that the extra energy results in electrical rectification or in excess electronic heat.

In the present chapter, I discuss the main photodetection dynamics that have so far been reported for THz photodetectors based on FETs. The goal is to introduce the physical and technical concepts that underpin the photodetection and noise studies presented in the rest of the thesis, that have been recently subject of many review articles [37,51,57–59].

2.2. Dyakonov and Shur theory: shallow water analogy in a gated electrons

In their seminal paper in 1993, Dyakonov and Shur [60] predicted that the electrons in a ballistic FET could behave as a liquid similar to shallow water. This liquid-like behaviour of the electrons in a gated system can be successfully exploited in a detecting operation scheme, as illustrated in figure 2.1, following the theory developed by Dyakonov and Shur which will be further discussed below.

In the presence of THz light, a finite *DC* voltage can be generated in a FET in response to an oscillating radiation field (figure 2.1). This is based on the fact that a FET hosting a 2D electron gas can act as a cavity for plasma waves[2] (collective density oscillations). When these plasma waves are weakly damped (that is, when a plasma wave launched at the source can reach the drain in a time shorter than the momentum relaxation time) the detection of radiation exploits constructive interference of the plasma waves in the cavity, which results in a resonantly enhanced response. This is the so-called resonant regime of plasma-wave photodetection, and can give rise to a signal that is 5–20 times stronger than the broadband non-resonant signal [59]. Broadband detection occurs when

---

[2] Plasma waves are the oscillations of electron density in space and time, and their properties depend on the electron density and on the dimensions and geometry of the electronic system. Unlike in a three-dimensional case, where the plasma oscillation frequency is nearly independent of the wave length, in a gated two-dimensional electron gas (2DEG), the plasma wave have a linear dispersion law similar to that of sound waves or light in vacuum. In this case, the plasma wave velocity, s, is proportional to the square root of the electron sheet density. The velocity of the plasma waves can be easily tuned by the gate bias that controls the 2DEG density. In plasma physics, waves in plasmas are an interconnected set of particles and fields which propagate in a periodically repeating fashion. A plasma is a quasineutral, electrically conductive fluid. In the simplest case, it is composed of electrons and a single species of positive ions, but it may also contain multiple ion species including negative ions as well as neutral particles. Due to its electrical conductivity, a plasma couples to electric and magnetic fields [8].

plasma waves are overdamped: that is, when plasma waves launched at the source decay before reaching the drain.

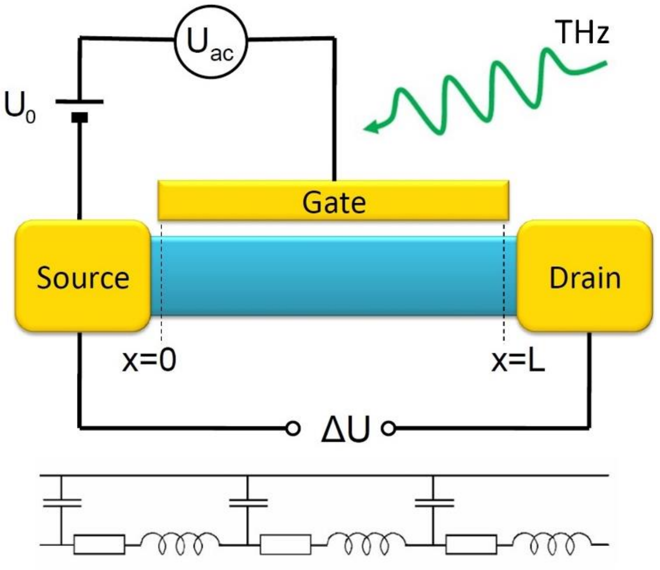

Figure 2.1: Schematics of a FET as a THz detector (above) and the equivalent circuit (below) [61].

2.2.1. Modelling high frequency and low frequency regime

The most important mechanism in the FETs is the nonlinearity mechanism which yields to the modulation of the electron density in the channel, and thus of the channel resistance, by the local *AC* gate-to-channel voltage, as described by Eq. 2.1. Owing to this phenomenon, in the expression for the electric current $j = e_0nv$, both the density n and the drift velocity v will be modulated at the radiation frequency. As a result, a *DC* current will appear: $j_{DC} = e_0 <n_1(t)v_1(t)>$, where $n_1(t)$ and $v_1(t)$ are the modulated components of n and v, and the angular brackets denote averaging over the oscillation period $2\pi/\omega$. Under open circuit conditions, a compensating *DC* electric field will arise, resulting in the photoinduced source-drain voltage ΔU. Obviously, some asymmetry between the source and drain is required to induce such a voltage. There might be various reasons for such an asymmetry. One of them is the difference in the source and drain boundary conditions due to some external (parasitic) capacitances. Another one is the asymmetry in feeding the incoming radiation, which can be achieved either by using a special antenna, or by an asymmetric design of the source and drain contact pads. Therefore, the radiation may predominantly create an *AC* voltage between the source and the gate (or between the drain and the gate) contacts. Finally, the asymmetry can naturally arise if a *DC* current is passed between source and drain, creating a depletion of the electron density on the drain side of the channel [62]. Theoretically, we will consider the case of an extreme asymmetry, where the incoming radiation creates an *AC* voltage with amplitude U_{ac} only between the source and the gate (figure 2.1). We will also suppose that there is no *DC* current between the source and drain.

In general, the FET might be described by an equivalent circuit (see figure 2.1), including the distributed gate-to-channel capacitance and the channel resistance, which depends on the gate voltage through the electron concentration in the channel:

$$e_0 n = CU \tag{2.1}$$

where n is the electron density in the channel, C is the gate-to-channel capacitance per unit area, and U is the gate to channel voltage. Note, that Eq. 2.1 is valid locally, as long as the scale of the spatial variation of $U(x)$ is larger than the gate-to-channel separation (the gradual channel approximation) [61]. Under static conditions and in the absence of the drain current, $U = U_0 = V_g - V_{th}$, where U_0 is the voltage swing, V_g is the gate voltage, and V_{th} is the threshold voltage at which the channel is completely depleted. The inductances in figure 2.1 represent the so called kinetic inductances, which are due to the electron inertia and are proportional to m, the electron effective mass. Depending on the frequency ω, one can distinguish two regimes of operation, and each of them can be further divided into two sub-regimes depending on the gate length L.

- (1) High frequency regime: It happens when $\omega\tau > 1$, where τ is the electron momentum relaxation time, determining the conductivity in the channel $\sigma = ne_0^2\, \tau/m$. In this case, the kinetic inductances in figure 2.1 are dominant, and the plasma waves analogous of the waves in an *RLC* transmission line, will be excited. The plasma waves have a velocity $s=(e_0U/m)^{1/2}$ [60] and a damping time τ. Hence their propagation distance is $s\tau$ (figure 2.2).
    - 1.a. Short gate, $L< s\tau$: The plasma wave reaches the drain side of the channel, is then reflected, and forms a standing wave with an enhanced amplitude, in which the channel serves as a resonator for plasma oscillations. The fundamental mode has the frequency ~ s/L, with a numerical coefficient depending on the boundary conditions.
    - 1.b. Long gate, $L>>s\tau$. The plasma waves excited at the source will decay before reaching the drain, so that the *AC* current will exist only in a small part of the channel adjacent to the source.
- (2) Low frequency regime: It occurs when $\omega\tau <<1$. The plasma waves are overdamped at the channel edge. At these low frequencies, the inductances in figure 2.1 become simply short-circuits and the circuit is then a simple RC line. Its properties further depend on the gate length, the relevant parameter being $\omega\tau_{RC}$, where τ_{RC} is the *RC* time constant of the whole transistor. Since the total channel resistance is $L\rho/W$, and the total capacitance is CWL (where W is the gate width and $\rho = 1/\sigma$ is the channel resistivity), one finds $\tau_{RC} = L^2 \rho C$.
    - 2.a. Short gate $L < (\rho C\omega)^{-1/2}$. This means that $\omega\tau_{RC} <1$, so that the *AC* current goes through the gate-to-channel capacitance practically as well as uniformly on the whole length of the gate. This is the so-called "resistive mixer" regime [63]. For the THz

frequencies this regime can apply only for transistors with extremely short gates (for instance smaller than 70 nm at 1 THz in silicon).

- 2.b. Long gate, $L >> (\rho C\omega)^{-1/2}$. Now $\omega\tau_{RC} >> 1$, and the induced *AC* current will leak to the gate at a small distance l from the source, so that the resistance $R(l)$ and the capacitance $C(l)$ of this piece of the transistor channel satisfy the condition $\omega\tau_{RC}(l) = 1$, where $\tau_{RC}(l) = R(l)C(l) = l^2\rho C$. This condition gives the value of the "leakage length" l on the order of $(\rho C\omega)^{-1/2}$ (that can also be rewritten as $s(\tau/\omega)^{1/2}$). If $l << L$, then neither *AC* voltage, nor *AC* current will exist in the channel at distances beyond l from the source.

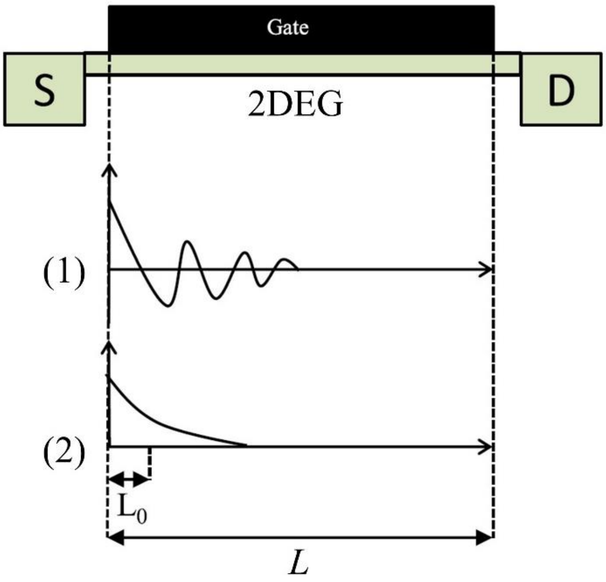

Figure 2.2: Qualitative space dependence of electron oscillations excited by THz waves for (1) high frequency, high mobility detector where $\omega\tau > 1$ and (2) lower frequency, lower mobility detector where $\omega\ \tau < 1$. L_0 is the characteristic length of the decay of the plasma wave excited at source side of the channel; S, D and L indicate the source and drain electrodes, and the gated area of the transistor respectively [50].

Therefore, the characteristic length where the *AC* current exists is $s\tau$ for $\omega\tau > 1$, and $s(\tau/\omega)^{1/2}$ for $\omega\tau < 1$ [8]. For instance, for $\tau = 30$ fs ($\mu = 300$ cm^2 /(Vs) in Si MOSFET[3]) and $s = 108$ cm/s the regime (1) will be realized for the radiation frequencies, ω greater than 5 THz; the regime 1.a. for $L <$ 30 nm. For $\omega = 0.5$ THz (the regime (2)), one finds the characteristic gate length distinguishing regimes 2.a. and 2.b. to be around 0.1 µm. If the conditions of the case 1.a. are satisfied, the

---

[3] Metal-Oxide-Semiconductor Field Effect Transistor

photoresponse will be resonant, corresponding to the excitation of discrete plasma oscillation modes in the channel. Otherwise, the FET will operate as a broad-band detector.

2.2.2. Simplified theory of hydrodynamic approach

Electron (holes) in a 2D gas can be considered as a liquid, following hydrodynamics laws if the electron-electron scattering time is shorter than impurities scattering, phonons scattering, and the characteristic time of the dynamics of the electrons (in THz regime ~1ps).

The most important case is that of a long gate (the regimes 1.b. and 2.b.) when, independently of the value of the parameter ωτ, the *AC* current excited by the incoming radiation at the source cannot reach the drain side of the channel. For this case, within the hydrodynamic approach the following result for the photoinduced voltage was derived [64]:

$$\Delta U = \frac{1}{4}\frac{U_{ac}{}^2}{U_0}\left(1+\frac{2\omega\tau}{\sqrt{1+(\omega\tau)^2}}\right) \tag{2.2}$$

As it is obtained from Eq. 2.2, the photoresponse changes only by a factor of 3, as the parameter ωτ increases from low to high values, even though the physics becomes different: at ωτ>1 plasma waves are excited, while at ωτ<1 they are not. The basic equations can be written as [60]:

$$\frac{\partial U}{\partial t}+\frac{\partial(Uv)}{\partial x}=0 \tag{2.3}$$

$$\frac{\partial v}{\partial t}=-\frac{e_0}{m}\frac{\partial U}{\partial x}-\frac{v}{\tau} \tag{2.4}$$

Here, Eq. 2.3 is the continuity equation, at which the carrier density *n* is replaced by using Eq. 2.1, while Eq. 2.4 is the Drude equation for the drift velocity *v* [65]. The boundary condition for gate-to-channel voltage at the source side of the channel ($x = 0$) is: $U(0,t) = U_0 + U_{ac}\cos(\omega t)$. For a long gate, the boundary condition at the drain is $v(\infty) = 0$.

The inertial term $\partial v/\partial t$ is accounted for by the kinetic inductances in figure 2.1. Here, we will consider only the simple case ωτ<1 when the inertial term can be neglected. Then $v = -\mu\partial U/\partial x$, and then:

$$\frac{\partial U}{\partial t}=\mu\frac{\partial}{\partial x}\left(U\frac{\partial U}{\partial x}\right) \tag{2.5}$$

where $\mu = e_0\tau/m$ is the electron mobility. We find the solution of the nonlinear Eq. 2.5 as an expansion in powers of U_{ac}: $U = U_0 + U_1 + U_2$, U_1 is the *AC* voltage, proportional to U_{ac}, and U_2 is the time independent contribution proportional to U_{ac}^2 (the photovoltage). In the first order in U_{ac} we obtain the diffusion equation for U_1 [25]:

$$\frac{\partial U_1}{\partial t} = s^2\tau\frac{\partial^2 U_1}{\partial x^2} \tag{2.6}$$

with the boundary conditions $U_1(0,t) = U_{ac}\cos(\omega t)$, $U_1(\infty,t) = 0$. The solution of this equation becomes:

$$U_1(x,t) = U_{ac}\, exp(-x/L_0)\, cos(\omega t - x/L_0) \tag{2.7}$$

where the characteristic length L_0 for the decay of the *AC* voltage (and current) away from the source is given by:

$$L_0 = s(2\tau/\omega)^{1/2} \tag{2.8}$$

This length justifies the size of certain part of transistor's channel adjacent to the source, whose resistance and the capacitance can be obtained such that $\omega\tau_{RC}(L_0) \sim 1$, as explained above.

In the second order in U_{ac}, Eq. 2.5 gives rise to:

$$U_0\frac{\partial U_2}{\partial x} + \left\langle U_1\frac{\partial U_1}{\partial x}\right\rangle = 0 \tag{2.9}$$

Which simply means the absence of the *DC* current. By integrating this equation, we can obtain:

$$U_2(x) = \frac{1}{2U_0}\left[\left\langle U_1^2(0,t)\right\rangle - \left\langle U_1^2(x,t)\right\rangle\right] \tag{2.10}$$

where the time averaged quantity $<U_1^2(x,t)> = (1/2)U_{ac}^2\, exp(-2x / L_0)$ can be found from Eq. 2.7. Hence, the photovoltage $\Delta U = U_2(\infty)$ coincides with Eq. 2.2, provided that $\omega\tau<<1$. Figure 2.3 demonstrates the *AC* voltage U_1 and the build-up of the *DC* voltage U_2 as functions of the distance from the source. The maximum photovoltage is achieved at U_0 close to 0V, where the relative *AC* modulation of the electron density in the channel is the strongest (we note that Eq. 2.1 is not valid in the vicinity of U_0 = 0V). Moreover, given the above-mentioned assumptions, Eq. 2.2 can be eventually given for $x = L$ by $\Delta U = \frac{U_{ac}^2}{4}\left(\frac{1}{\sigma(U_0)}\frac{d\sigma(V_g)}{dV_g}\right)_{U_0}$ where σ is *DC* conductivity.

This formula is practically useful when experimental data must be compared with theory, since it allows assessing the photoresponse of a device with the theoretical prediction based on the simple *DC* conductivity measurement of σ.

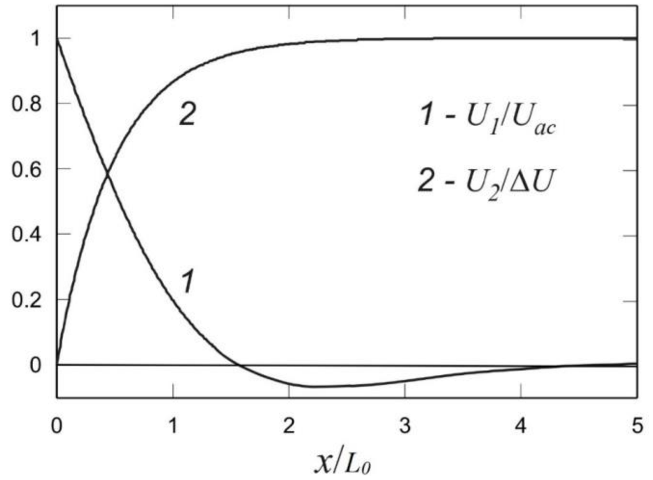

Figure 2.3: Dependence of the *AC* voltage U_1/U_a at $\omega t = 2\pi n$ and of the *DC* photoinduced voltage $U_2/\Delta U$ on the distance from the source x for a long gate [65].

It is also instructive to compare the FET detector with the well-known Schottky diode detector. In both devices, the detection process is based on a rectification of an incident THz field by a nonlinear element. However, there are some significant differences. The nonlinearity in the photoresponse, expected in a Schottky diode, is due to the nonlinear I-V characteristic of the potential barrier between the metal and the semiconductor. The physical origin of the nonlinearity in the case of the FET transistor is very different. As discussed above, it is due to the fact that the incident THz radiation modulates both the carrier drift velocity and the carrier density. The static I-V dependence has no direct relevance to the detection properties of the FET.

2.3. Photodetection enabled by photovoltaic effect

In a photovoltaic (PV) detector, the separation and transport of the photocarriers is due to the presence of an internal (built-in) electric field inside the photoactive material. This internal electric field can be generated, for example, at the interface between semiconductors with different doping levels (p-n junction) or at the interface between a metal and a semiconductor (Schottky junction). When operated in PV mode, the detector is unbiased, i.e., the external voltage applied is zero. While illuminating the detector under a short-circuit condition, an internal electric field is created. The photocurrent measured in this configuration is also called short-circuit current I_{sc}. In the open-circuit configuration, photocarriers with different polarities accumulate to counterbalance the internal electric field (figure 2.4b), hence generating a photovoltage. The forward bias voltage required to compensate this photovoltage is called open-circuit V_{oc}.

In-plane *p-n* junctions can be realized by doping the semiconductor with local split gates, which allows controlling of the built-in electric field across the depletion region (figure 2.4a,b).

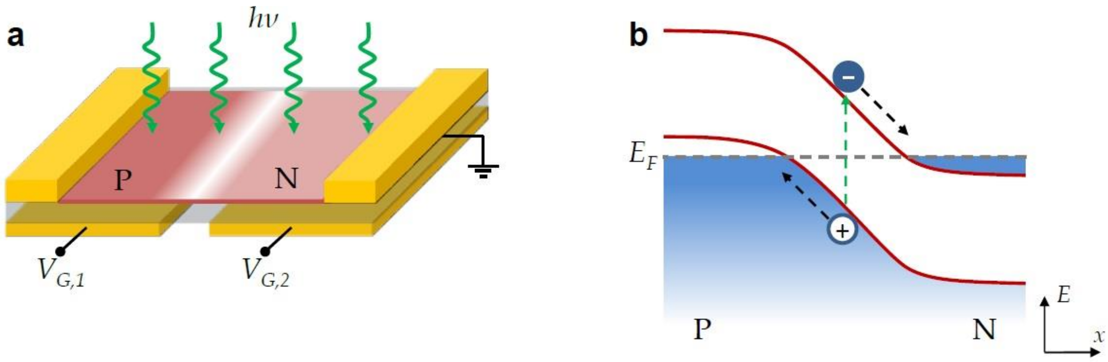

Figure 2.4: a) Schematic of a planar p-n junction achieved by locally doping the semiconductor channel (red) with split gates V_{G1} and V_{G2}. b) Band diagram of the p-n junction under illumination, depicting the photocurrent generation process.

2.4. Photodetection enabled by hot carriers

One of the possible ways for the photoexcited carriers to relax is to redistribute their energy among other carriers, which leads to an increase of the electron temperature T_e (figure 2.5). In photovoltaic (PV) cells, this process transforms the excess photon energy into electronic heat and leads to a loss of power conversion efficiency. However, the increment in the average carrier temperature can, in turn, drive a photocurrent or photovoltage through two main processes: the thermoelectric (or Seebeck) effect and the bolometric effect. These photodetection mechanisms can be divided in three steps:

- Free carrier absorption: unlike photocarrier-driven detectors, thermally-driven detectors do not need the excited and ground states of the optical transition to be separated by an energy gap ΔE. Both intraband and interband transitions can contribute to the photodetection process. Owing to this absence of photon energy threshold, thermal photodetectors usually have a broad spectral responsivity.
- Generation of a hot-carrier distribution: photocarriers thermalize with the surrounding carriers, typically through carrier-carrier scattering (for instance in graphene it lies in the time scale of <100fs [66]). Once carriers have reached thermal equilibrium, they form a so-called hot carrier distribution, which can be well-explained by a Fermi-Dirac distribution with an elevated temperature T_e.
- Transport and cooling of the hot carriers: the creation of a local or global hot carrier distribution can have several effects on carrier transport. The temperature gradient resulting from local heating may lead to the generation of photocurrent or photovoltage through the thermoelectric effect. Homogenous heating can also alter the resistance of the photoactive

material (bolometric effect), causing a change in voltage or current. The electric signal persists until the hot carrier distribution cools down to the ambient (lattice) temperature (figure 2.6) typically via optical and acoustic phonon emissions[67].

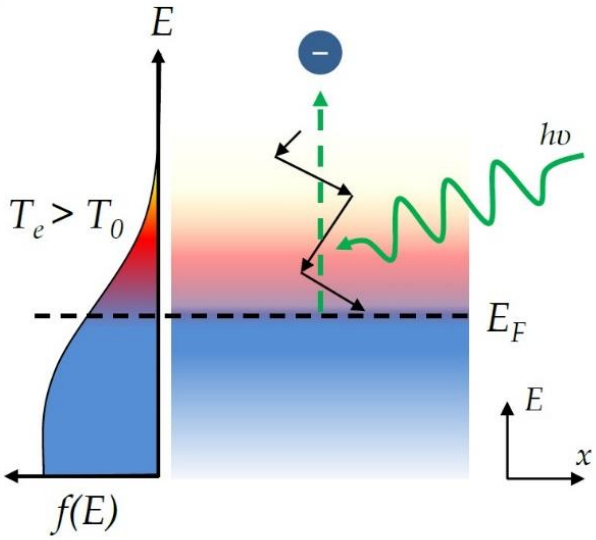

Figure 2.5: Photodetection mechanism by the excess heat contained in the electronic bath generated by the thermalization of photoexcited carriers with the surrounding carriers. This process, described by the black arrows, leads to an electronic Fermi-Dirac distribution *f(E)* with a temperature T_e larger than the ambient or lattice temperature T_0.

2.4.1. Transport and heat dissipation dynamics

Thermoelectric equations governing the energy flux and current density J in an electronic system can be described as follows [68]:

$$C_e \frac{\partial T_e}{\partial t} = \kappa \nabla^2 T_e - \nabla . (V + \prod) J + \dot{Q}_{ext} \tag{2.11}$$

$$J = \sigma \, (-\nabla V - S \, \nabla T) \tag{2.12}$$

where T_e is the local carrier temperature, S is the local Seebeck coefficient of material, V is the local voltage, C_e is the electronic heat capacity, κ is the thermal conductivity, Π is the local Peltier coefficient of the material and $\dot{Q}_{ext}$ is the rate at which heat is added (or removed) by an external source (cooling channel). The first term of Eq. 2.11 implies to Fourier's law, while the second term is the energy carried by the electrical current density. Since J is typically small, this latter term can be neglected.

2.4.2. Photo-thermoelectric effect

In the photo-thermoelectric (PTE) effect, light absorbed in a region of the photoactive material heats up the local carrier temperature T_e, which creates a temperature gradient ∇T_e between the two ends of the material. Because of the variations in the carrier drift velocity and chemical potential with temperature, the thermal diffusion of carriers generates a net charge imbalance, and thus a potential gradient ∇V between the hot and cold ends. According to Eq. 2.12, the conversion of ∇T_e into ∇V is proportional to the Seebeck coefficient, or thermopower, S:

$$\nabla V = S \nabla T_e \tag{2.13}$$

The Seebeck coefficient can be assessed by using the well-known Mott formula:

$$S = -\frac{\pi^2 k_B^2 T_e}{3e_0} \frac{1}{\sigma(E_F)} \frac{\partial \sigma(E)}{\partial E}\bigg|_{E=E_F} \tag{2.14}$$

where $\sigma(E)$ is the energy-dependent conductivity. We should also note that this formula is derived considering the Sommerfeld expansion, that is only valid for $T_e \ll E_F / k_B$.

The PTE effect has been shown to contribute to the zero-bias photoresponse of several 2D materials, such as graphene [69–79], WSe_2 [80], and black phosphorus [81]. Xu *et al.* [69] confirmed that this effect happens at the interface of graphene with different Fermi energies, in agreement with theoretical predictions [82]. In the following chapters, we illustrate that the PTE effect has been exploited for the zero-biased as well as zero dark current detection purpose, specifically in the case of graphene.

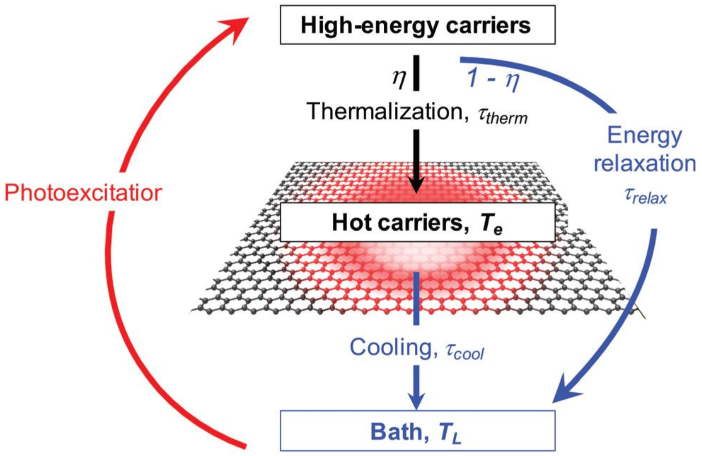

Figure 2.6: Schematic illustration of the formation of hot carriers via photoexcitation, followed by thermalization of high-energy carriers. Since high-energy carriers can also directly relax to their environment, the branching ratio between these two processes determines the heating efficiency η [66].

2.4.2.1. PTE photodetectors

In a PTE photodetector, a photovoltage (or photocurrent) is created by impinging light into the junction of regions with different Seebeck coefficients (S_1 and S_2), which can be made by using two different materials or by changing the doping level in two distinct regions of the same material (figure. 2.7a). In the short-circuit configuration, the total photovoltage generated by the PTE effect is given by:

$$\begin{aligned}\Delta V &= \frac{1}{W}\iint S\,\nabla T_e\,dx\,dy \\ &= (S_2 - S_1)(T_{e,hot} - T_{e,0}) = \Delta S\,\Delta T_e\end{aligned} \tag{2.15}$$

where W is the width of the junction, $T_{e,hot}$ is the enhanced carrier temperature at the junction and $T_{e,0}$ is the carrier temperature in the absence of illumination (normally equal to the ambient temperature). In this latter configuration, the photovoltage acts as an electromotive force, generating a photocurrent:

$$PC = \frac{\Delta S\,\Delta T_e}{R} \tag{2.16}$$

where R is the total resistance of the device.

The efficiency and response time of PTE detectors are highly influenced by the heat transport in the device that governs ΔT. In the simplest case, a light beam (with power P and area A) heats carriers at a rate corresponding to the optical power absorbed in the material, while heat is lost at a rate $\Gamma\Delta T_e$. We also reckon that heat conduction in the material is negligible. In this case, Eq. 2.11 will become:

$$C_e \frac{\partial T_e}{\partial t} = P_{in} - \Gamma\Delta T_e \tag{2.17}$$

where $P_{in} = P_{abs} / A$ is the absorbed power density.

Under pulsed excitation, and assuming that C_e and Γ are constant, the solution to this equation is:

$$\Delta T_e(t) = \Delta T_e(0)\,exp\left(-\frac{t}{\tau_{cool}}\right) \tag{2.18}$$

where $\Delta T_e(0)$ is the initial raise in the carrier temperature and $\tau_{cool} = C_e / \Gamma$ is the characteristic carrier cooling time. Since photocurrent generation is driven by ΔT_e, τ_{cool} governs the photoresponse time of the photodetector. Moreover, under steady-state conditions, Eq. 2.17 gives rise to:

$$\Delta T_e = \frac{P_{in}}{\Gamma} = \frac{P_{in}\,\tau_{cool}}{C_e} \tag{2.19}$$

By combining Eqs. 2.16 and 2.19, we will achieve:

$$PC = \frac{\Delta S}{R}\frac{P_{in}\,\tau_{cool}}{C_e} \tag{2.20}$$

$$IQE = \frac{h\nu}{e_0}\frac{\Delta S}{AR}\frac{\tau_{cool}}{C_e} \tag{2.21}$$

In sum up, there are multiple parameters to be taken into account for engineering a well-performing PTE photodetector. Most significantly, these parameters will be linked to the material properties such that the materials with a large Seebeck coefficient S, high absorption coefficient α (in our application particularly in THz range), small electronic heat capacity C_e and small resistance of R can be certainly tailored for this application. Moreover, even though a small characteristic carrier cooling time τ_{cool} yields to a fast response time, it affects the photocurrent as well as *IQI* in a destructive way. Since τ_{cool} dependent of the optical, acoustic and substrate phonon scattering, choosing a proper substrate is an essential requirement for an efficient PTE photodetector. Additionally, an appropriate design and engineering for the device fabrication is another key of success to exploit PTE for high detection performance.

2.4.2.2. Graphene based PTE photodetector

Several conclusions can be drawn from this simple PTE model. First, it shows that the PTE efficiency depends directly on two important properties of the photoactive materials: the electron heat capacity C_e and the seebeck coefficient S. Graphene is an excellent PTE material due to the fact that it combines a small C_e (~2000 $k_B\mu\text{m}^{-2}$ at 300K) [83] and a relatively large S (~ 100 (T/300[K]) µV/K) [84] simultaneously, in particular close to the Dirac point. Considering that the carrier mobility is independent of E_F (which is the case when charged impurity scattering is the dominant process), Mott formula (Eq. 2.14) yields:

$$S = -\frac{2\pi^2 k_B^2 T_e}{3e_0 E_F} \tag{2.22}$$

Furthermore, the dependence of C_e as the heat capacity of a degenerate 2D electron gas on E_F is given by:

$$C_e = \frac{1}{3}\left(\frac{k_B}{hv_F}\right)^2 E_F\, T_e \tag{2.23}$$

where v_F is the carrier Fermi velocity.

Eqs. 2.22 and 2.23 indeed exhibit that S increases and C_e decreases as E_F approaches to the charge neutrality point. However, both equations cannot be applied when $E_F/k_\mathrm{B} \ll T_e$ and a more detailed theory is needed in this regime [82,85]. It is also interesting to note that $S = C_e / (e_0\, n)$, where n is the charge carrier density.

The difference in Seebeck coefficient ΔS also yields to a distinct six-fold pattern in the PTE photocurrent when the Fermi level of both regions are varied simultaneously (figure 2.7b). In fact, Song *et al.* [82] first predicted that the PTE photocurrent should vanish when the Fermi energies of both the regions are equal ($E_{F,1} = E_{F,2}$) and when they satisfy the relation $E_{F,1}\, E_{F,2} = \Delta^2$, where Δ represents the width of the charge neutrality point, also known as charge-puddle width. The last condition holds since both electrons and holes contribute to the PTE effect and cancel each other. This is in complete contrast with the photovoltaic (PV) effect, where the polarity of the photocurrent depends on the direction of the electric field. In this case, the PV photocurrent dependence on the Fermi energies changes polarity only once, when $E_{F,1} = E_{F,2}$. Thus, measuring the photocurrent as a function of both Fermi energies provides a clear and simple way to distinguish between the PV and PTE effect and identify the dominant photocurrent generation mechanism [86].

The PTE model mentioned above will also highlight the significant effect of the cooling time τ_{cool} on the *IQE* and the response time of the photodetector. In other words, in PTE mechanism a longer cooling time leads to a large *IQE* but results in a slower response time, and vice versa. In the case of graphene, the cooling time of hot carriers depends on various carrier relaxation processes regarding the experimental conditions (defects, substrate, temperature, etc). In general, its cooling time at room temperature is of the order of ~ few ps, which is governed by several mechanisms including optical phonon emissions [87], simultaneous optical phonon emissions and re-thermalization of carriers [88], acoustics phonon emissions [66], disorder-assisted acoustic phonon scattering [89], anharmonic coupling of optical and acoustic phonons [66], and coupling to substrate phonons [90], that implies a large theoretical bandwidth (~ 500 GHz [91]) but gives rise to a moderate *IQE* values (1 to 20%) [59,92].

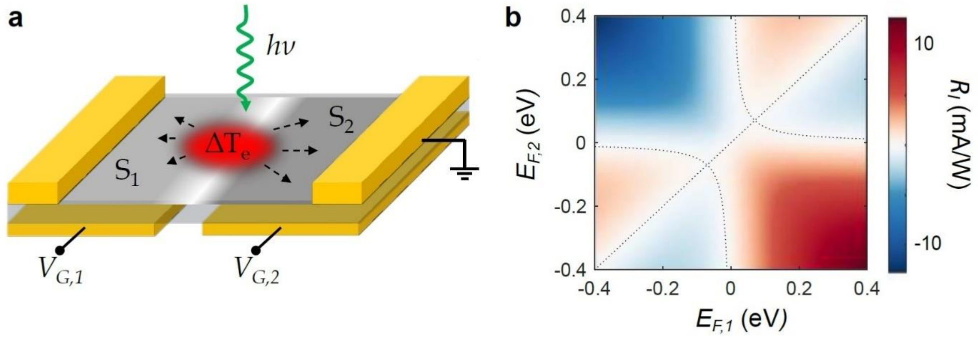

Figure 2.7: a) Schematic of a PTE photodetector based on a p-n junction. Photocurrent or photovoltage is generated by locally heating up (ΔT_e, red region) the interface between regions with different Seebeck coefficients (S_1 and S_2). Here, this interface is considered by locally doping each region with split gates ($V_{G,1}$ and $V_{G,2}$). b) PTE responsivity R_I of graphene calculated as a function of the Fermi energies $E_{F;1}$ and $E_{F;1}$ in the two distinct regions depicted in a. Calculations are performed applying a conductivity model similar to the one presented by Song *et al*. [82], with a constant temperature difference ΔT_e = 4K and charge-puddle width Δ = 70 meV. The dotted lines determine the regime in which the responsivity vanishes. The PTE response map displays a well-known phenomenon called sixfold pattern.

As discussed above, PTE detectors inherently do not require threshold photon energy to operate, as opposed to PV detectors. Therefore, they can detect light over a larger spectral range and are only limited by the absorption spectrum of the photoactive material.

2.4.3. Bolometric effect

The bolometric effect is associated with the change in the transport conductance G_e, produced by heating associated with the incident photons (figure 2.8). The photocurrent generated via this process is therefore obtained by:

$$PC = \frac{\partial G_e}{\partial T} V \, \Delta T_e \tag{2.24}$$

A bolometer measures the power of electromagnetic radiation by absorbing the incident radiation (dP) and reading out the resulting temperature increase dT. Bolometers are mainly made of semiconductor [93] or superconductor absorptive materials [32] and are widely used in the submillimetre (THz) wave-length range [59], where they are among the most sensitive detectors. The key parameters of a bolometer are the thermal resistance R_h = dT/dP, which ultimately defines its sensitivity, and the heat capacity C_e , which determines its response time $\tau = R_h\, C_e$ [32]. For instance, graphene has small volume for a given area and low density of states, which results in low C_e, thus a fast device response. The cooling of electrons by acoustic phonons is inefficient, owing to the small Fermi surface, and cooling by optical phonons requires high T_e ($k_B T_e$ > 0.2 eV) [59]. Hence, R_h is relatively high, giving rise to high bolometric sensitivity. Since this effect relies on a change in the transport properties of the material (as explained above, this photodetection mechanism is based on a light-induced change in conductance as opposed to the transport of charges), bolometers cannot drive a photocurrent and require an external bias (*V*) to operate. Moreover, unlike the PTE effect, the bolometric effect can happen in a homogeneous photoactive material and do not require any type of p-n junction.

In fact, this conductance change induced by the incident light can be owing to two mechanisms: (1) a change in carrier mobility due to the associated temperature change; or (2) a change in the number of carriers contributing to the current [59]. We note that (2) coincides with the PV effect, with the electric field generated by the external bias. The photo-bolometric effect has been measured several times in graphene [74,94,95] and black phosphorus [81,96]. Since both PTE and bolometric photodetectors rely on the photo-induced heating of carriers, many of their photodetection metrics are similar. The responsivity reported for graphene devices at room temperature is, however, relatively low, on the order of 0.2 mA/W [94].

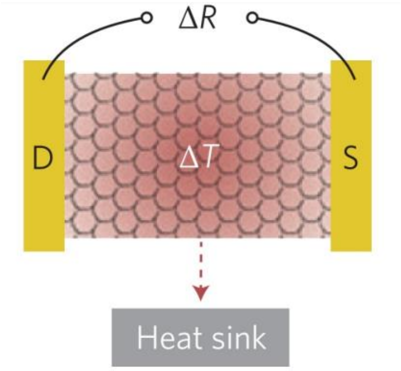

Figure 2.8: Schematic representation of bolometric effect. Red shaded area indicates elevated electron temperature with ΔT the temperature gradient and ΔR the resistance across the channel where S and D indicate source and drain.

Chapter 3: Scalable THz photodetectors based on two-dimensional nanomaterials and Van der Waals heterostructures

3.1. Photodetectors based on single layer graphene

The advent of grain-of-rice-size THz lasers on a chip, operating at 250 K [16], a temperature reachable with a plug-in cooler, and of chip-scale THz frequency combs [97], has recently triggered the development of compact and technologically relevant THz systems. However, producing low-cost (<10k$) and scalable multi-pixel THz detectors operating at room temperature (RT), with noise equivalent powers (NEP) < 1 $nWHz^{-1/2}$, suitable for real-time detection or quantum applications, is still elusive, in particular for operating frequencies > 2THz, appealing for broadband integrated systems comprising miniaturized quantum cascade laser (QCL) combs [97].

Focal plane arrays, the most commonly employed architectures for multipixel tomography, are currently based on either microbolometers [98], or complementary metal-oxide-semiconductor (CMOS) image sensors. Commercially available microbolometers have a low NEP ~30 $pWHz^{-1/2}$[10], with a slow response time (τ) in the range~10-1000 μs [98]. CMOS-based field effect transistors (FETs) show τ <1 μs [99] and their NEP decreases (63 $pWHz^{-1/2}$ at 2.5 THz) when reducing the gate lengths to 90 nm [100]. However, this hampers the device cost-effectiveness, in particular for high (>2.5 THz) frequencies [100].

An option to overcome these limitations is to integrate large area (cm^2) single layer graphene (SLG) with existing CMOS readout integrated circuit (ROIC) architectures [101,102], taking advantage of well-established, high-volume and low-cost silicon technology.

SLG is an intriguing material in optoelectronics, and, due to its vanishing bandgap [103] (figure 3.1b), which results in a broadband absorption, has often been considered as a key material in nanoelectronics and photonics. Besides the interband absorption, driven by optical transitions between the valence and conduction bands, light–matter interaction in graphene is also characterized by strong intraband absorption [104], which makes it promising for the detection, generation, and modulation of THz waves.

Specifically, the absorption of THz radiation is accompanied by the heat transfer toward the electronic sub-system. The record low electronic specific heat (∼2000 $k_B$$\mu m^{-2}$ at 300K) [105], stemming from the light-like linear energy dispersion, entails ultrafast carrier thermodynamics [106] which yields in large thermal gradients and vast non-linear response to THz transients [107]. Together with high room temperature (RT) carrier mobilities (∼105 $cm^2V^{-1}s^{-1}$) [108] and high breakdown current density (∼108 Acm^{-2}) [109], the ultrafast photoresponse enables high-speed device operation. These unique properties, combined with the possibility of tuning via electrostatic gating, are driving a noticeable surge of research efforts to merge the physics of graphene with device principles across the THz.

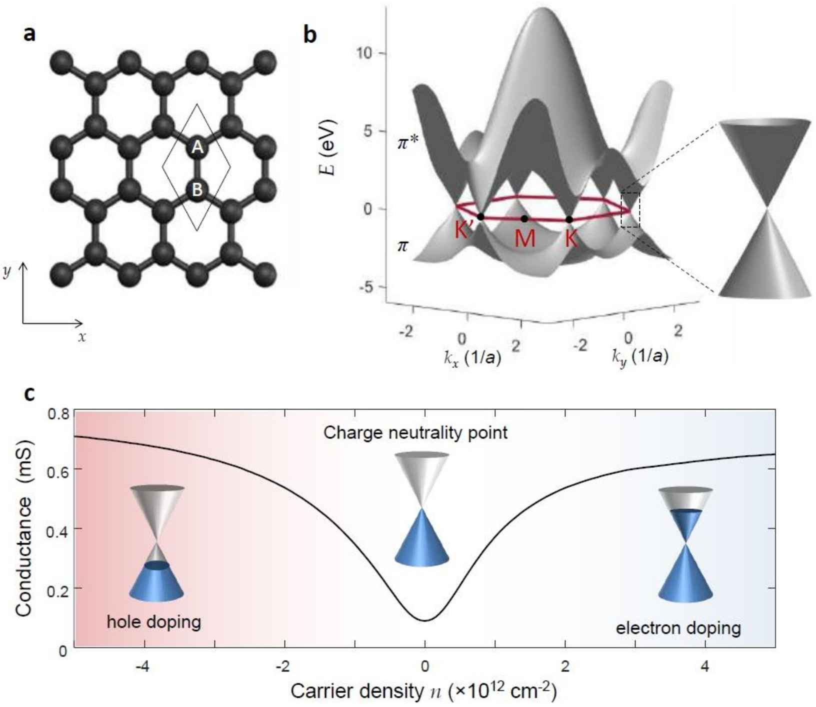

Figure 3.1: Structural and electronic properties of graphene. a) The hexagonal lattice of graphene. The elementary cell (solid black line) contains two carbon atoms belonging to sublattices A and B. Each atom in sublattice A has 3 nearest neighbours in sublattice B, and vice-versa. b) Band structure of graphene. Left: Electronic dispersion of the valence π-band and conduction π*-bands calculated using the tight-binding approximation [103]. The k_x and k_y are normalized by the lattice constant a. The Brillouin zone and the high symmetry points are shown in red. Right: Zoom on the linear dispersion (Dirac cone) close to one of the Dirac points. c) Ambipolar conductance of a graphene device as a function of the charge carrier density n. Inset: Dirac cones with different doping levels. The blue region corresponds to the states filled by electrons.

Graphene-CMOS integration is now feasible thanks to the progresses in scalable SLG production and transfer [110]. Broadband image sensor arrays operating from ultraviolet (4-400nm) to short-wave infrared (SWIR, 900-2000 nm) have been realized by integrating large area CVD graphene with CMOS [102]. The integration of CVD SLG with lithium niobate, a thermally polarizable material, resulted in mid-infrared pyroelectric bolometers with state-of-the-art temperature coefficient of resistance [111]. Single-crystal (SC) CVD SLG, coupled to photonic waveguides, was used for ultrafast, zero-dark-current telecom photodetectors (PDs) for datacoms [112], and wafer scale integration of electro-absorption modulators with state of the art performance, employing ~12000 SC SLG matrices was also achieved [113].

The hot-carrier-assisted PTE effect is a very efficient detection mechanism in SLG (figure 3.2) [78,79,114–116]. Efficient carrier heating, which stems from the low specific heat of SLG’s electrons and high SLG optical phonon energy (~0.2 eV [117]), can result in large electronic temperature (T_e ~1000 K [118]) gradients, ΔT_e, under photoexcitation, pushing T_e far above the lattice temperature [119–121]. The ultrafast electron dynamics [83], combined with the absence of a bandgap, enables broadband and high-speed PTE detection. Unlike photovoltaic or bolometric effects [59], PTE can be activated in asymmetric [116] or asymmetrically coupled FETs [78] under zero-bias operation (i.e. zero dark current), thus ensuring low power consumption and flicker noise [122].

In a FET designed to operate as a detector, at THz frequencies, CVD SLG can help relaxing the geometrical and technical constraints (e.g. gate length ≤ 90 nm [100]) while preserving compatibility with wafer-level scalable CMOS technology.

Single pixel PTE-GPDs, based on high-mobility (μ up to 53.000 $cm^2V^{-1}s^{-1}$) graphene encapsulated in hexagonal boron nitride (hBN), are the state-of-the-art when it comes to RT THz and mid infrared (MIR) PDs [79,116,123], when compared to any other technology. Ref.[124] reported mm-wave (300- 600 GHz) RT GPDs exploiting cm^2 area CVD SLG with $\mu < 2000$ $cm^2V^{-1}s^{-1}$. However, the performance in the sub-THz range was well below the state-of-the-art, with NEP ~ 0.5 $nWHz^{-½}$ at 600 GHz, almost one order of magnitude larger than achieved with micro-mechanically exfoliated [114] or hBN-encapsulated [79,116] SLG at much larger frequencies (~3THz), where usually a drop in performance is expected [79,114–116]. The response time was not reported [124].

In this chapter, I will present PTE GPDs operating at 2.8 THz exploiting state-of-the-art large area (~1cm^2) single crystal CVD SLG, with mobility μ ranging from 500 $cm^2V^{-1}s^{-1}$ up to 20.000 $cm^2V^{-1}s^{-1}$, combined with a planar antenna, on-chip radio frequency circuitry, and coplanar striplines (CPS) that reach the bonding pads from the electrodes, through an adiabatically matched transition [71,79]. Subsequently, we propose the use of layered material heterostructures (LMHs) as for substrate treatment [125] or large-area encapsulation [126] to reach stable and repeatable state-of-the-art performances at RT. We then develop RT GPDs based on large-area (∼1 cm^2) CVD SLG with and without large-area (∼1 cm^2) CVD hBN capping.

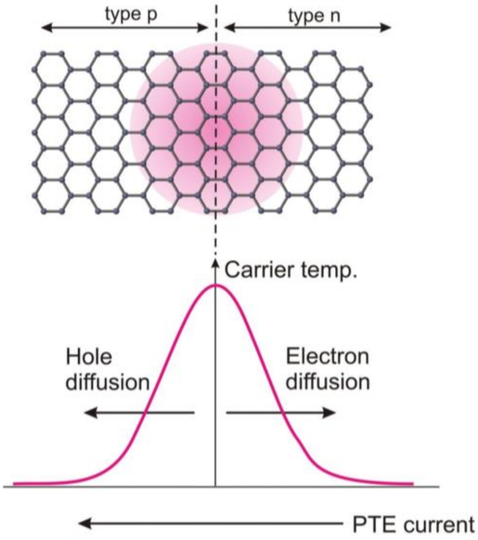

Figure 3.2: Photocurrent generation in a graphene p-n junction photodetector: profile of carrier concentrations due to light intensity distribution driven by PTE effect [29].

3.1.1. THz nonlinear interaction and conductivity in graphene

The optical response of graphene at visible and infrared (IR) frequencies is independent of incident light frequency and can be well-defined by universal conductivity $G = e_0^2/4\hbar$ where $\hbar$ is $h/2\pi$. As compared to other semiconductor or metallic materials with the same atomic layer thickness, monolayer graphene has an extreme optical absorption (with $\pi\alpha = 2.3\%$) [127]. In contrary with its absorption, the reflection (<0.1%) is almost negligible in the visible light spectrum. The opacity is determined only by the precision structure constant $\alpha = E^2/ \hbar c$ [128]. Without inter-layer electron coupling, the optical absorption of uniform multilayer graphene relies on the layers, and the opacity increases linearly by 2.3% with the stacking of layers.

Both electrical transport and optical properties of graphene are governed by conductivity σ [129]. Graphene conductivity is given by sum of intraband and interband conductivity, which are induced by electron–phonon scattering relaxation and interband electron transition, respectively. When $|\mu_c| \square\ k_B T$, intraband conductivity is expressed by the Drude–Boltzmann model [130] similar to metal, and it is controlled by chemical energy μ_c. In the case of interband conductivity, there is a critical frequency ω_c which is related to chemical energy $h\omega_c = \mu_c$. In fact, if the wave associated frequency is lower than ω_c, the interband conductivity contribution is almost negligible in the total conductivity.

In contrast to IR and visible light, THz waves oscillate on a (sub-picosecond) timescale, considerably longer than the typical electron momentum scattering time in graphene which is on the order of 10–100 fs [131]. Therefore, in the THz range, the carrier transport typically occurs in the diffusive regime (figure 3.2), where electrons undergo several momentum scattering events within the duration of the THz wave oscillation period, and the microscopic motion of electrons is generally incoherent with the driving electric field [131]. Furthermore, the nonlinearity mechanism in graphene only requires THz fields of the order of 10s of $\mathrm{kVcm^{-1}}$, which is ~ 3 orders of magnitude smaller (i.e., requiring about one million times less peak power) than that required for the optical or IR nonlinearity in graphene via coherent Bloch oscillations [132,133].

At THz frequencies, with the relatively low photon energy, interband transition can only occur at low temperature and with undoped graphene ($E_F \approx 0$) [131]. Hence, compared to IR and visible light, the incident THz field could generally induce the intraband transition of graphene carriers, as shown in figure 3.3a,b. For the THz field from free space into the substrate with graphene, the THz field transmission could be described by the Tinkham equation [134]:

$$\vec{E}_t(\omega) = \frac{2}{1 + n_s + Z_0\,\sigma(\omega)}\vec{E}_{in}(\omega) \tag{3.1}$$

where $E_{in}(\omega)$ is the incident THz field, n_s is the refractive index of the substrate, Z_0 is the free-space impedance, and $\sigma(\omega)$ is the intraband conductivity of graphene at THz band. Considering the incident THz field, the intraband conductivity $\sigma(\omega)$ is nonlinear, and could be expressed by solving the Boltzmann equation as [134,135]:

$$\sigma(\omega)=\frac{-e_0^{\,2}v_F^2}{2}\int_0^\infty D(E)\frac{\tau(E)}{1-i\omega\tau(E)}-\frac{\partial f_{FD}(E,\mu_c,T_e)}{\partial\varepsilon}dE \tag{3.2}$$

where v_F is the Fermi velocity of the relativistic Dirac fermions in graphene, $\tau(E)$ is the energy-dependent electron scattering time, $D(E)$ is the density of states, and $f_{FD}(E, \mu_c, T_e)$ is the Fermi–Dirac distribution function for chemical potential μ_c and electron temperature T_e as below:

$$f_{FD}(E,\,\mu_c,T_e)=\frac{1}{\left[exp\left(\frac{E-\mu_c}{k_B T_e}\right)+1\right]} \tag{3.3}$$

According to Eq. 3.2, we could find that the intraband transition conductivity of graphene is determined by μ_c, electron temperature T_e, and density of states of the graphene energy bands $D(E)$. Also, as shown in figure 3.3c, the energy of the incident THz is transferred to electrons in graphene, yielding to an enhancement in T_e, and the concomitant decrease of σ.

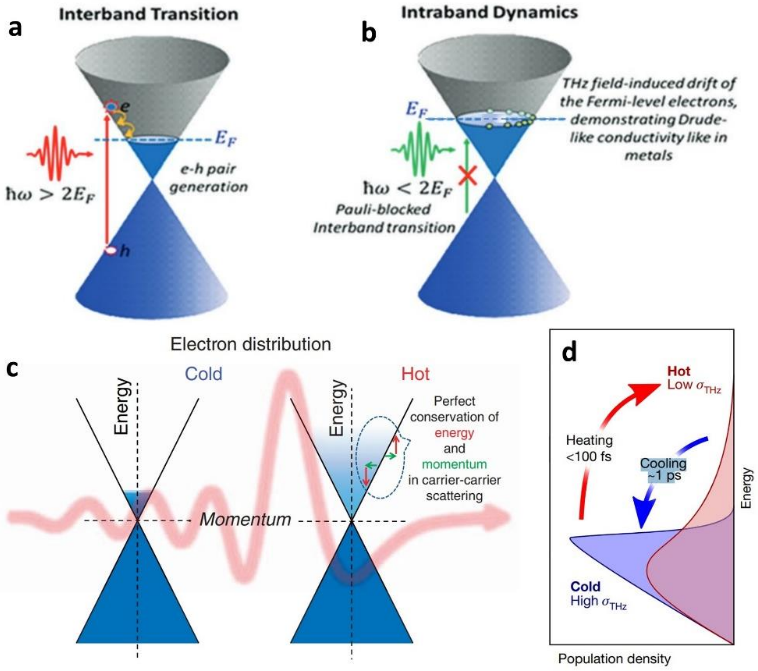

Figure 3.3: Interaction of graphene with a light field: Schematic of the band structure with a) interband transition due to absorption of a photon of energy larger than twice the Fermi energy, $\hbar\omega > 2E_F$, leading to electron–hole pair generation, followed by the energy and momentum exchange with the Fermi sea electrons via electron–electron scattering, and b)

intraband dynamics when $\hbar\omega < 2E_F$, which exhibits Drude-like conductance [131]. c) Cold and hot-carrier distribution in graphene, before and after interaction with the strong-field THz signal, respectively. The illustration of perfect energy and momentum conservation in electron–electron scattering, resulting in fs order thermalization of the electron gas in graphene. d) Energy dependence and conservation of the free carrier density for the cold and hot-carrier distributions illustrated in c. The elevated electron temperature leads to a smeared-out carrier distribution, and accordingly lowered chemical potential [136].

3.1.2. Graphene growth and transfer techniques

SLG SCs are grown via CVD on Cu (figure 3.4a) in an Aixtron Black Magic on 35 μm-thick Cu foil, electro-polished using a solution containing [137] 450 ml deionized (DI) water, 225 ml orto-phosphoric acid 85% (H_3PO_4), 225 ml ethanol, 45 ml isopropanol and 7.2 g urea. 60 ml of this solution are poured in a staining jar. Next, a Cu foil is placed in the filled jar and connected to the positive terminal of a current generator. A thicker (~0.7mm) Cu plate is placed in the jar parallel to the Cu foil at a distance~2.5 cm and connected to the negative terminal of the current generator. A current~1.5A is then passed for 90s to smoothen and clean the Cu foil surface. The foil is then loaded in the furnace to perform the CVD growth [138]. This is done by raising T from RT to ~1000°C in Ar. The pressure is kept constant~25mbar throughout the whole process. These conditions are then held for 30mins to anneal the Cu foil. 50 sccm H_2 and 30 sccm 0.01% diluted CH_4 in Ar are then added to the chamber to trigger the growth of SLG, which lasts ~3h. The sample is then cooled to RT and unloaded from the furnace. A4-950K poly(methyl-methacrylate) polymer (PMMA) is spin-coated at 4000 rpm on the SLG+Cu surface. This is then placed on a solution of 3g of ammonium persulfate in 100 ml DI water to etch Cu. Once Cu is etched, PMMA+SLG is transferred to a beaker with DI water for rinsing, then lifted with the target over a Si substrate (350μm, resistivity > 10000 Ωcm) covered with SiO_2 (300 nm) and left to dry overnight. This substrate choice is technologically attractive thanks to its scalability and affordability. The PMMA is finally removed with acetone, leaving SLG on SiO_2/Si.

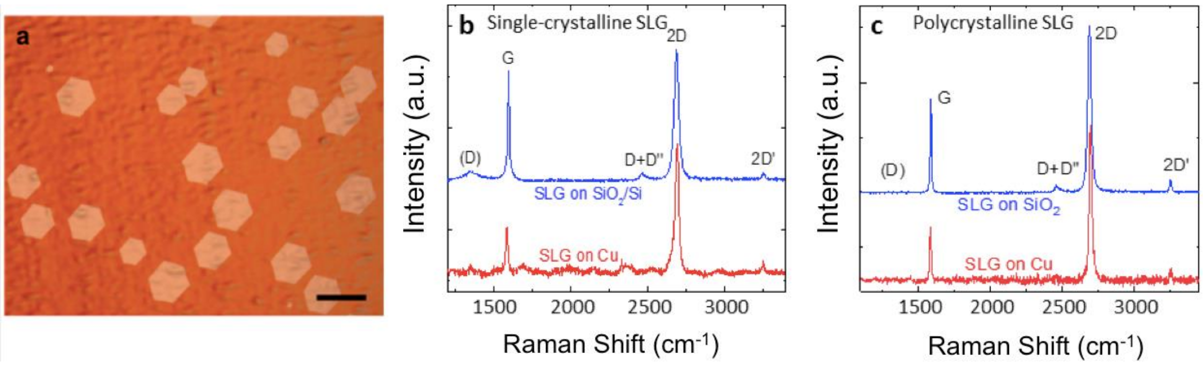

Figure 3.4: a) Representative optical image of SLG grains grown on Cu, with contrast enhanced by heating in air for 1 min at 250°C [138]. Scale bar 100 μm. b) Representative Raman spectra, measured at 532 nm of as-grown SLG SC on Cu (blue) and SLG after transfer on SiO_2/Si (red). The single-crystalline nature of the samples has been deduced from their hexagonal shape and from the fact that they all show an identical orientation. c) Raman spectra at 514.5nm of polycrystalline SLG as grown (red) on Cu and transferred SLG (blue) on SiO_2/Si.

Raman spectroscopy is used to monitor the SLG quality [139,140] with a Renishaw inVia spectrometer at 514 and 532 nm and a 100× objective lens. The blue curve in figure 3.4b shows the Raman spectrum of SLG on Cu after subtracting the Cu photoluminescence [141]. The single Lorentzian (2D peak) at ~2691.3±0.1 cm^{-1} with full-width-at-half-maximum (FWHM) ~27.3±0.4 cm^{-1} is consistent with SLG [139,140]. The G peak position is Pos(G)~1585.1±0.2 cm^{-1} and FWHM(G)~16.4±0.7 cm^{-1}. The 2D to G area and intensity ratios are A(2D)/A(G)~4.67±0.22 and I(2D)/I(G)~3.6±0.4. We then wet transfer SLG on SiO_2/Si. Next, we re-check the SLG quality to confirm this is not affected by the transfer process. The red curve in Fig.5b is a representative Raman spectrum of SLG on SiO_2/Si. The position of the 2D peak, Pos(2D), is~2685.3±0.3 cm^{-1}, with FWHM(2D)~36.9±0.2 cm^{-1}, Pos(G)~1595.2±0.1 cm^{-1}, FWHM(G)~11.8±0.2 cm^{-1}. The 2D to G area and intensity ratios are A(2D)/A(G) ~4.39±0.04, I(2D)/I(G) ~1.49±0.08. These indicate ~250±50meV *p*-type doping [142]. The D peak at 1352.8±0.6 cm^{-1} has an intensity ratio with respect to the G peak I(D)/I(G) ~0.046±0.003, indicating a small defect density ~1.7±0.4 ×10^{10}cm^{-2}[64,65].

Continuous polycrystalline SLG is grown on a~30 μm thick Cu foil by low pressure CVD (LPCVD). Before growth, the foil is annealed at 1050°C for 2h under H_2 (100sccm) atmosphere at 1atm and cooled to RT. For the growth, the system is heated to 1050°C with 50sccm H_2 at 0.4 torr and the Cu foil is annealed for 2h. 5 sccm CH_4 are introduced to initiate growth and the CH_4 flow is stopped after 30 mins to terminate it. The system is cooled to RT under 50 sccm H_2 in 60mins. To transfer SLG, the top side of SLG/Cu is spin coated with PMMA (A4 950) at 1000 rpm for 60s. PMMA/SLG/Cu is then baked on hot plate at 80^0 for 10mins. SLG on the Cu back side is removed by O_2 plasma. Electrochemical delamination is carried out by applying voltage to a Pt anode and PMMA/SLG/Cu cathode in a NaOH aqueous solution (1 M). A voltage potential of 2V is held in the two-electrode system. Delamination completes within few s and the PMMA/SLG stack floats on electrolyte. The stack is then transferred into DI water and scooped out onto SiO_2/Si, dried overnight, then baked at 80 °C for 10mins. PMMA is dissolved in acetone. The sample is rinsed in IPA and dried.

As grown and transferred SLG is characterized by Raman spectroscopy. A statistical analysis is performed to estimate doping and defect density. The errors are calculated from the standard deviation across different spectra, the spectrometer resolution (~1 cm^{-1}) and the uncertainty associated with the different methods to estimate the doping from Pos(G), FWHM(G), I(2D)/I(G), A(2D)/A(G) and Pos(2D). The Raman spectrum of as grown polycrystalline continuous SLG on Cu is in Fig. 5c, after Cu PL removal [139]. The 2D peak is a single Lorentzian with FWHM(2D)~24±3 cm^{-1}, signature of SLG [139]. Pos(G)~1585±2 cm^{-1}, FWHM(G)~16±2 cm^{-1}, Pos(2D)~2703±4 cm^{-1}, I(2D)/I(G)~3.6±0.4, A(2D)/A(G)~5.5±0.7. No D peak is observed, indicating negligible Raman active defects [143,144]. The Raman spectrum after transfer on SiO_2/Si is in figure 3.4c. The 2D peak retains its single-Lorentzian line shape with FWHM(2D)~27±1 cm^{-1}, Pos(G)~1591±2 cm^{-1}, FWHM(G)~9±2cm^{-1}, Pos(2D)~2691±2 cm^{-1}, I(2D)/I(G)~1.6±0.2, A(2D)/A(G)~4.7±0.4, indicating a p-doping with Fermi energy E_F=300±50 meV [142,145], corresponding to a carrier concentration n_0~5.7±1.8 × 10^{12} cm^{-2} [142,145]. I(D)/I(G)~0.01±0.02, corresponding to a defect density n_D~3.6±1.8×10^9 cm^{-2} for excitation energy 2.41eV and E_F=300±50 meV [143].

3.1.3. Device fabrication

For all GPDs we employ a common channel geometry, with channel length L_c = 4 μm. We vary the channel width W_c between 0.8 and 1.8 μm. The transferred large (cm^2) area SLG is etched in O_2 plasma to realize electron beam lithography (EBL) patterned U-shaped structures to increase the SLG-metal interface at the *s* and *d* electrodes (figure 3.6). This shape is chosen to avoid geometric overlap between top-gates and the underlying electrodes, thus allowing to use a thin (40 nm) oxide film as gate dielectric, maximizing the gate-to-channel capacitance per unit area (C_{Ga}), while reducing leakage currents and the chance of dielectric breakdown.

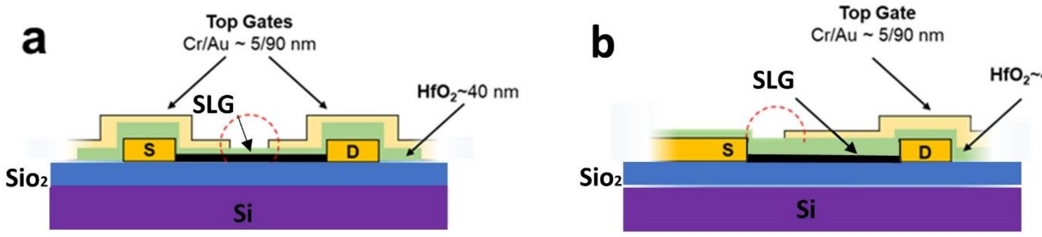

Figure 3.5: Schematic cross-section of the GFETs. a) double-gated SiO_2/SLG/HfO_2. b) single-gated SiO_2/SLG /HfO_2. Dashed red circles indicate the position of the THz-induced field enhancement.

The SLG channels are annealed in Ar at 280°C for 2h before starting the fabrication of the devices. This step reduces the *p*-doping leading to reduction of intrinsic charge carrier density, n_0, from 5×10^{12} to 0.5×10^{12} cm^{-2} with respect to non-annealed samples without degrading the material quality [146]. The *s* and *d* contacts are then realized by EBL and Cr/Au thermal evaporation (5/100 nm). The top-gate oxide layer (HfO_2, t_{ox} = 40 nm) is lithographically defined and grown by atomic layer deposition (ALD) in an OpAL reactor (Oxford Instruments). Considering the permittivity of Hafnium oxide $\varepsilon_r = 19.8$ [147], the resulting gate-to-channel capacitance per unit area is $C_{Ga} = \varepsilon_r\varepsilon_0/t_{ox}$ ~0.44 μFcm^{-2}. ALD is used because of its compatibility with wafer-scale processing. The top-gates are then defined by EBL and established by metallization (5/90 nm Cr/Au) and lift-off (figure 3.5). Scanning electron micrograph (SEM) images of two GPDs are in figure 3.6a,b, together with a summary of the relevant geometrical parameters.

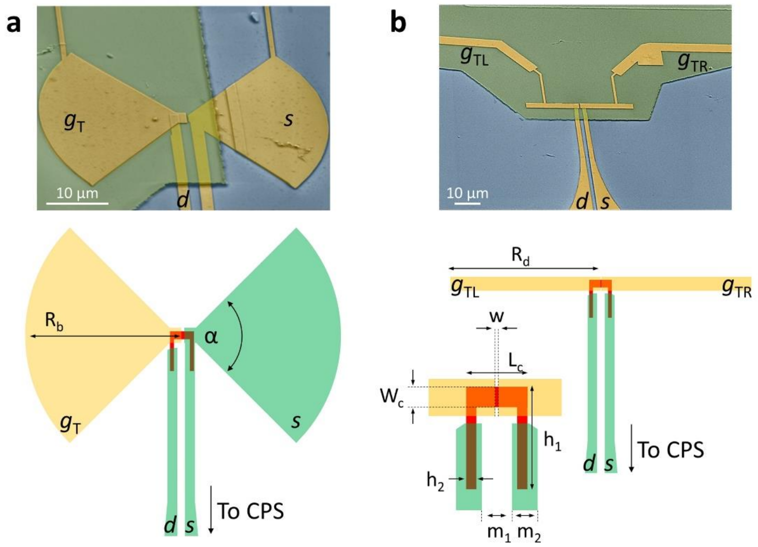

Figure 3.6: (a) Bow-tie coupled single-gated CVD GFETs, with an on chip bow-tie antenna. R_b is the antenna radius, α = 90° is the antenna flare angle. (b) Dual gated SLG *p-n* junction integrated in a linear dipole antenna. The half-length of the dipole R_d is indicated. Inset: layout of the *p-n* junction active element (a similar layout is used for the single-gated geometry) indicating the relevant geometrical parameters. L_c and W_c are the length and width of the gated area, *w* is the size of the gap between the two top-gates, $h_{1,2}$ are geometrical parameters defining the contact areas, $m_{1,2}$ define the CPS. False color SEM images show two GPDs.

Furthermore, large-area CVD graphene offers the possibility to fabricate multiple devices in parallel. Figure 3.7a shows the result of the simultaneous fabrication of 12 GFETs. As-fabricated samples are then mechanically cleaved and mounted on ceramic chip carriers for electrical and optical testing (figure 3.7b).

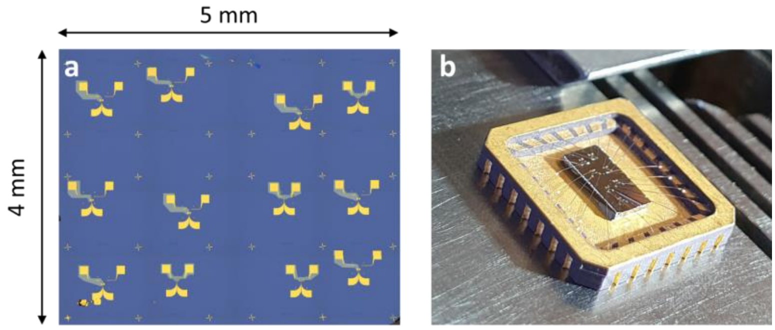

Figure 3.7: a) Optical microscope image of 12 devices fabricated on a Si/SiO$_2$ substrate. b) Photograph of a chip mounted on a ceramic carrier for *dc* electrical characterization.

3.1.4. Antenna simulation

We use two architectures to prepare single-top-gated GFETs, integrated in a planar bow-tie antenna (antenna radius R_b = 24μm, flare angle α = 90°) and a set of split-gate *p-n* junctions, integrated either in a planar bow-tie or in a linear dipole antenna (total antenna length $2R_d$ = 48 μm), as shown in figure 3.6a,b. The antenna dimensions are chosen based on the electromagnetic simulations shown in figure. 3.8a,b, where we use a commercial finite element method (FEM) software (COMSOL Multiphysics) by solving Maxwell's equations [148] to evaluate the electric field enhancement at the center of the antenna, as a function of R_b and R_d when a 2.8 THz wave impinges on the GPDs. We also evaluate the antenna response as a function of impinging radiation frequency, using an antenna half-length of 24μm, identical to the size used for the experiments (figure 3.6a,b). In the model, the THz wave, polarized parallel to the antenna axis, impinges on the detector from the air side. The simulation results (figure 3.8c,d) indicate that the two antenna geometries have different response bandwidths: the calculated percent bandwidth, defined as the ratio between the absolute bandwidth and the central frequency [149], is 44% for the bow-tie configuration, and 12.5% for the linear dipole one, respectively.

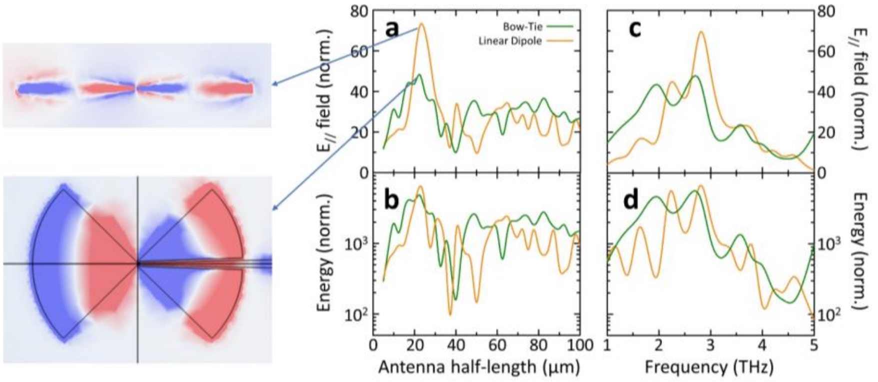

Figure 3.8: (a,b) Antennas simulations showing the field enhancement with respect to the antenna dimensions, for w = 200 nm. a) Enhancement of the electric field component parallel to the antenna axis ($E_{//}$) as a function of the antenna half-length (R_b, R_d) under 2.8 THz illumination (arrows are

pointing to the maps of the out-of-plane component of the electric field corresponding to the peak values of $R_d = R_b = 24\mu m$, top: linear, and down: bow-tie, under 2.8 THz illumination). b) Energy enhancement as a function of the antenna half-length. The bow-tie antenna has a smaller energy enhancement (a factor ~2). c) Energy enhancement as a function of radiation frequency. The percent bandwidth is 44% for the bow-tie antenna and 12.5% for the linear dipole antenna. d) In-plane field enhancement for bow-tie and linear dipole antennas *vs*. frequency. The results shown in (a,b,c,d) are obtained by evaluating a volume integral in the position of the GFET channel for both energy and in-plane electric field, when the metallic antenna is on the substrate and normalizing it to the case where there is no antenna on the substrate.

3.1.5. Optical setup and method

To test the optical response of the devised photodetector, we employ a 2.8 THz QCL driven in pulsed mode (repetition rate 40 kHz, duty cycle 4%). The laser pulses are modulated by a square wave envelope with frequency ranging from 1.334 to 43.33 kHz, simultaneously acting as reference for lock-in detection. The 40° divergent optical beam emitted from the QCL facet is first collimated, then focused by two TPX lenses, reaching a spot-size with FWHM~300 μm (figure 3.9). A set of motorized linear stages provides precise positioning of the detector in the focal point. The total power P_t over a $3\times5\ cm^2$ area around the beam spot is measured with an absolute THz power/energy meter (Thomas Keating). Since our GPDs active areas are much smaller than the beam waist, the fraction of optical power delivered to the GPDs, P_a, is estimated as $P_t \times S_t/S_\lambda$, where S_t is the beam spot area and $S_\lambda=\lambda^2/4$ is the diffraction limited area [78]. The photoresponse V_{LIA} is measured between the *s* and *d* electrodes with a lock-in (SR5210) over a voltage preamplifier (dlInstruments) having gain G = 1000. The photovoltage Δu and R_V are then calculated as $\Delta u=2.2\times V_{LIA}/G$ and $R_v=\Delta u/ P_a$. τ is determined by recording the time traces of Δu with an oscilloscope (Tektronix DPO5204, 2 GHz bandwidth), when the QCL is driven in the negative differential resistance region [78]. Δu is pre-amplified with a 1.1 GHz amplifier (Femto DUPVA) using a gain of 70 dB. The input impedance of the preamplifier (50 Ω) is much smaller than the GFET resistance (~10kΩ), thus producing a signal loss of ~200 through the corresponding voltage divider.

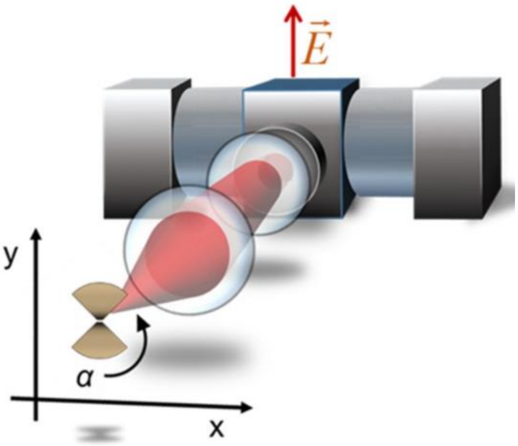

Figure 3.9: Schematic of the terahertz experiment: 2.8 THz radiation from a QCL mounted in Stirling engine cryostat is focused via a couple of optical lenses onto the GFET, whose position (*xy* plane) and orientation with respect to the laser polarization (angle α) can be controlled.

3.1.6. Sigle-gated device characterization

Electrical (transport) characterization

- From the characterization of the channel resistance (R) curve as a function of V_g, we extract the field-effect mobility (μ_{FE}), the contact resistance (R_0) and n_0 by using the fit function $R = R_0 + (L_C/W_C)(1/n_{2d}e\mu_{FE})$ [150], where n_{2d} is the gate-dependent charge density, given by $n_{2d} = \{n_0^2 + [C_{Ga}/e\ (V_G - CNP)]^2\}^{1/2}$. Figure 3.10a plots $R(V_g)$ for one of the single-top-gated bow-tie GPDs. The e/h branches asymmetry with respect to the CNP can be ascribed to their different scattering cross section in the vicinity of charged impurities [151].

  Using the GFET transconductance, it is possible to determine the physical mechanism underlying THz detection. In particular, we numerically evaluate the expected dependence of the photovoltage as a function of V_g in the cases of a detection dominated by the PTE or by the overdamped plasma wave (OPW) mechanisms. In the PTE case, the photovoltage amplitude (V_{PTE}) is proportional to the electronic temperature gradient along the graphene channel (ΔT_e) [78] and its dependence from V_g is determined by the difference between the Seebeck coefficients of the gated (S_{bg}) and ungated (S_{bu}) portions of the channel [78]: $V_{PTE} = \Delta T_e \cdot (S_{bg}\text{-}S_{bu})$. Interestingly, S_b can be extracted from $R(V_g)$ (figure 3.10a) by using the Mott equation [78]. In FETs operating at room temperature, the OPW mechanism typically interplays with the PTE response and their individual contributions are often not easy to disentangle in single gated geometries [152]. However, the dependence of the OPW response (V_{OPW}) with respect to V_g slightly differs from the PTE one. In particular, it is proportional to the F-factor of the FET, defined as [152] $F = -1/\sigma\times\partial\sigma/\partial V_g$, where σ is the static conductivity of the FET channel. For GFETs, both F and V_{OPW} cross zero at the charge neutrality point (CNP) [78,152], and are expected to be negative for *n*-doping and positive for *p*-doping

[78,152]. The curves in figure 3.10b are calculated from *R*(V_g) (figure 3.10a) and represent a direct comparison of the two mechanisms for the single-gated device. Importantly, the PTE mechanism entails a double sign-change of the photovoltage in proximity of the Dirac point [78], not expected in the plasma wave effect [152].

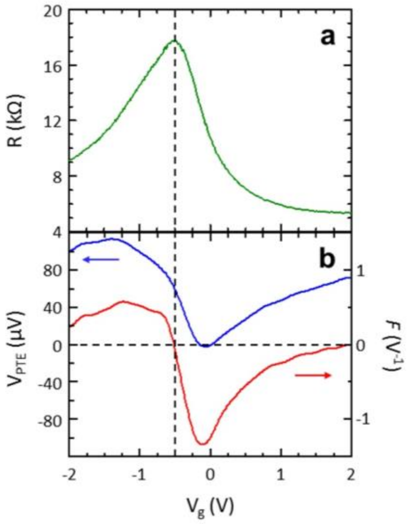

Figure 3.10: **Electrical properties of single-gated GFETs**. a) Channel resistance at RT as a function of V_g, showing the CNP at V_g = -0.48 V. For this device, the extrapolated e (h) μ_{FE}~1200 cm^{2}V^{-1}s^{-1} (900 cm^{2}V^{-1}s^{-1}) and n_0~4.1 ×10^{11} cm^{-2}. b) Comparison between the PTE and OPW models. Left vertical axis, blue curve: PTE photovoltage (V_{PTE}) obtained as the difference between the Seebeck coefficient under the gate electrode (S_{bg}) and in the ungated portion of the channel (S_{bu}), multiplied by ΔT_e=1K. S_{bg} is calculated from the GFET transconductance, using the Mott equation [78]. S_{bu} is assumed equal to S_{bg} at V_g = 0V. Right vertical axis, red curve: FET factor (*F*), calculated from the GFET transconductance [152].

- We then measure the photovoltage with a lock-in amplifier and calculate the voltage responsivity R_v. Figure 3.11a is the V_g dependent R_v collected while the QCL illuminates the detector from the air-side (blue curve). The sign of R_v changes twice across the V_g sweep, in agreement with previous findings on PTE-GFET THz GPDs [78,116]. We then collect the photoresponse when the QCL radiation impinges on the GPD from the substrate. This gives a photovoltage increase of a factor ~ 4 (light-blue curve, figure 3.11a), ascribed to the increased directivity of the bow-tie antenna towards the substrate [153]. The comparison between figure 3.10b with the experimental responsivity in figure 3.11a clearly shows that the measured photoresponse is dominated by the PTE mechanism and cannot be generated by a dominant overdamped plasma wave effect.

We estimate the gate bias dependent *NEP* (figure 3.11b), defined as the ratio between the GPD noise spectral density (NSD, noise voltage per unit bandwidth) and R_v. We approximate the NSD with the Johnson-Nyquist noise [78,116] $N_{JN} = (<V_{th}^2>)^{1/2} = (4k_B RT)^{½}$, where k_B is the Boltzmann constant and T=300K is the heat sink temperature. In order to prove the validity of this approximation, we directly measure the GPD NSD using a spectrum analyzer (figure 3.11c). At low frequencies (< 1kHz) the noise figure is dominated by the contribution of the flicker (1/f) contribution, in agreement with Ref. [154]. Above 5 kHz, the 1/f noise becomes negligible and noise is dominated by N_{JN}. *NEP* as a function of V_g is in figure 3.11b with a minimum ~3 $nWHz^{-½}$ for air-side illumination, and ~600 $pWHz^{-½}$ when illuminated from the substrate.

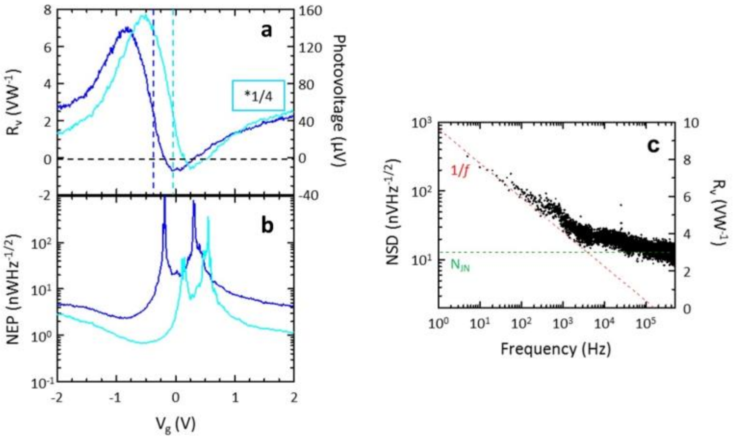

Figure 3.11: a) Left vertical axis: THz responsivity measured with a modulation frequency o kHz. The double sign change is compatible with a PTE-dominated response. Right vertic photovoltage measured when light impinges from the front and through a Si-lens substrate as a function of V_g. The improved optical coupling raises the photoresponse by a factor ~ 4. b) *NEP* as a function of V_g. c) Noise voltage per unit bandwidth while keeping V_g = 0 V.

Optical characterization

- The GPD speed is determined by fitting the time traces recorded with an oscilloscope using charge and discharge exponential equations [77]. When the pulsed QCL is operated in the negative differential resistance (NDR) regime, its emission becomes intermittent and transitions between off- and on-states occur with rise- and fall-times ~1 ns [78,79]. Thus, the dynamics of the source are faster than those of the detectors, and the intensity fluctuations can then be used to estimate the receiver response time. We then drive the QCL in pulsed mode in the NDR state. The GPD output is pre-amplified and monitored with a fast oscilloscope, with readout bandwidth=1.1GHz. The setup allows us to evaluate detector τ of ~1 ns, or larger (anything faster than that would be setup-limited). Figure 3.12 shows one of the QCL intensity fluctuations (*on-off-on*) retrieved by a single-gated GFET for V_g = -0.5V, giving τ ~ 6±0.3 ns.

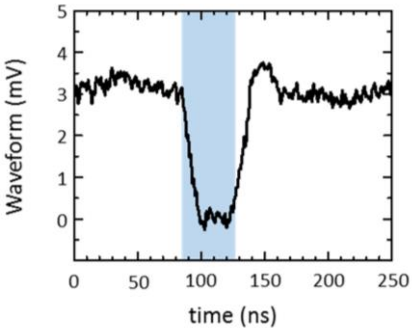

Figure 3.12: Black curve: photovoltage time trace recorded when the QCL is driven in the negative differential resistance regime. From the waveform we extract τ ~ 6±0.3 ns. The blue shaded area represents the time interval in which the laser emission is off.

3.1.7. Double-gated device characterization:

We then characterize the *p-n* junction devices by collecting resistance (figure 3.13a) and R_V (figure 3.13b) while sweeping V_{gL} and V_{gR}. The field effect is visible in the resistance map (figure 3.13a) of a representative *p-n* junction GPD, showing 4 regions, corresponding to the different doping in the two sides of the junction. Considering an horizontal line cut across the map of R and using the fitting procedure described in Ref. [150] gives $\mu_{FE}(e)$ = 480 cm^{2}V^{-1}s^{-1}, $\mu_{FE}(h)$ = 1080 cm^{2}V^{-1}s^{-1} and n_0 = 5 ×10^{11} cm^{-2}.

We then measure the R_V map by illuminating the sample from the air-side. In the case of hot-carrier-assisted photo-detection, the photoresponse is proportional to the S_b difference in the two differently doped regions of the junction. As a consequence of the non-monotonic nature of S_b, the photovoltage exhibits multiple sign switches, resulting in the characteristic six-fold pattern (figure 3.13b), signature of PTE-driven detection [86]. Under the assumption of a NSD dominated by thermal fluctuations (Johnson-Nyquist noise), we extract *NEP* following the procedure described before, reaching~1.3 nWHz$^{-1/2}$ for V_{gL} = -2V, V_{gR} = 1.7 V, which defines a *p-n* junction at the geometrical center of the SLG channel. The *NEP* map inherits the 6-fold pattern of the R_v map (figure 3.13c). Figure 3.13d presents a comparison between the responsivity measured when the *p-n* junction GPD is illuminated from the air-side and from the substrate, showing an increase of a factor ~2 in the latter case, in agreement with the expected increase in the antenna directivity towards the Si substrate as mentioned earlier.

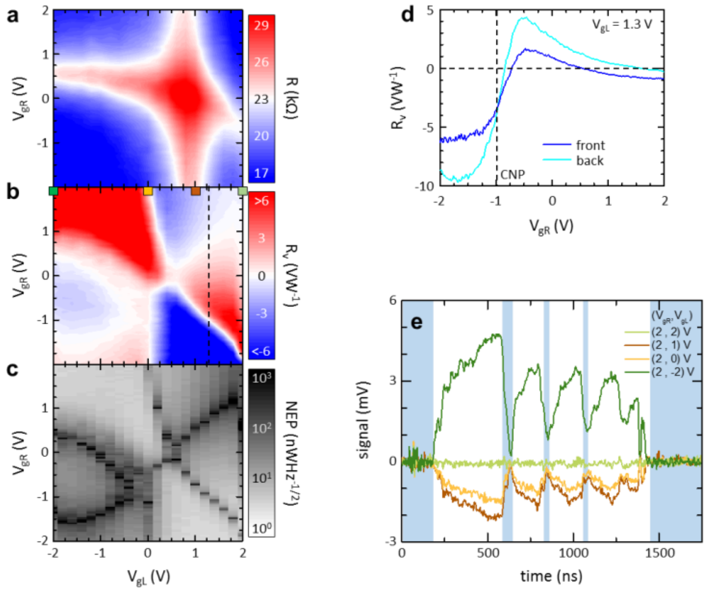

Figure 3.13: **Electrical and optical characterization of *p-n* junction GFETs.** a) Channel resistance map as a function of the bias applied on the split-gates. 4 transport regimes corresponding to *p−n*, *p−p*, *n−p*, and *n−n* doping are seen. b) R_V map. Sign reversal leads to additional *p−p′* and *n−n′* regions, thus a 6-fold symmetry, the hallmark of PTE [86]. The dashed vertical line indicates the line-cut in the map corresponding to panel (d). c) *NEP* map, showing a minimum of 1.3 nWHz$^{-1/2}$ for V_{gL}=-2V, V_{gR}=1.7V. d) Responsivity measured while irradiating the detector from substrate-side (light-blue) and air-side (blue), keeping V_{gL} = 1.3 V and while sweeping V_{gR} from -2V to +2V. e) Photovoltage time traces, recorded when the QCL is driven in the negative differential resistance regime, measured for different V_{gL}, V_{gR}. The extracted τ is ~ 5.2±0.4 ns. Shaded areas mark the time intervals where the laser output power is expected to vanish as a consequence of fluctuations.

We then characterize τ of the *p-n* junction devices, in analogy with the single-gated GFETs. Figure 3.13e plots the time traces of the optical response recorded for a representative GPD, for different gate configurations, while driving the QCL in the NDR regime. In agreement with the 6-fold patterns, the signal waveforms have different signs, corresponding to different S_b on the left and right sides of the junction. E.g., when V_{gL} = V_{gR} = 2V, the signal drops to zero, because S_b does not change across the junction. By fitting the measured time traces, we extract a minimum τ ~ 5.2±0.4 ns for V_{gL} = 2 V, V_{gR} = -2V, i.e. when the *p-n* junction is activated.

3.1.8. Statistical analysis of device performance

We then investigate 25 GPDs fabricated following the two architectures described above. Among them, 4 detectors were not working properly and showed a NEP > 10 μWHz$^{-1/2}$ and are then not considered in the following discussion. This gives a yield > 80%. The scatter-plot of the minimum *NEP* as a function of n_0 (figures 3.14a) shows a positive correlation between the two quantities, with a

Pearson correlation coefficient[4] ρ_p~ 0.8. Therefore, a lower intrinsic SLG doping is desirable to improve *NEP*. On the other hand, the scatter-plot of the minimum *NEP* as a function of μ has a negligible correlation ρ_p = -0.2 (figure 3.14b). Similarly, the contact resistance $R_0^* = R_0 \times W_c$ plays a minor role in determining the *NEP* (ρ_p = 0.1, figure 3.14c), with respect to n_0, which appears to be the dominant electrical factor in the optical performances. This can be intuitively related with the PTE mechanism. n_0, which depends on the material quality, strongly affects the magnitude of S_b. Beside this, ΔT_e is larger for lower n_0 because the heat capacity is smaller. Lower n_0 gives a lower *NEP* [116]. Since, from our findings, the dependence between *NEP* and μ is much weaker, n_0 is the decisive electrical parameter in the detector PTE performance. Figure 3.14a shows similar performance between GPDs with bow-tie or linear dipole antennas, consistent with the numerical simulations of figure 3.8. Single-gated GFETs show a slightly better NEP (a factor ~2 lower, on average) with respect to split-gate architectures. This makes single-gated GFETs more promising for the realization of large arrays of detectors, being easier to fabricate and more practical to operate, with only one electrode to be biased. A detailed statistical analysis of the device-to-device variability of optoelectronic parameters will be reported at the end of this chapter.

By analyzing the effect of W_c (0.8-2μm) on the detection performance, we conclude that, even though the dependence is weak, the *NEP* increases for narrower channels (figure 3.14f) as a consequence of the increased device resistance (figure 3.14d) that translates in an increase of NSD, not fully counterbalanced by R_V, figure 3.14e.

---

[4] **Correlation Analysis.** In order to characterize the correlation between our GPDs optical and electrical performances, we use the Pearson (product-moment) correlation coefficient, ρ_p, which can be considered a measure of the linear correlation between two variables [295]. Given the data sets p and q, each with N observations, ρ_p is defined as [295]:

$$\rho_p(p,q) = \frac{1}{N-1}\sum_{i=1}^{N}\left(\frac{p_i - \acute{p}}{\sigma_p}\right)\left(\frac{q_i - \acute{q}}{\sigma_q}\right)$$

Where $\acute{p}$ and $\acute{q}$ are the mean values and σ_p and σ_q are the standard deviations for p and q, respectively. As a result, ρ_p is a value in the range (-1,1), where ρ_p = 1 (ρ_p = -1) indicates a positive (negative) linear dependence and ρ_p = 0 indicates no linear correlation between the two variables.

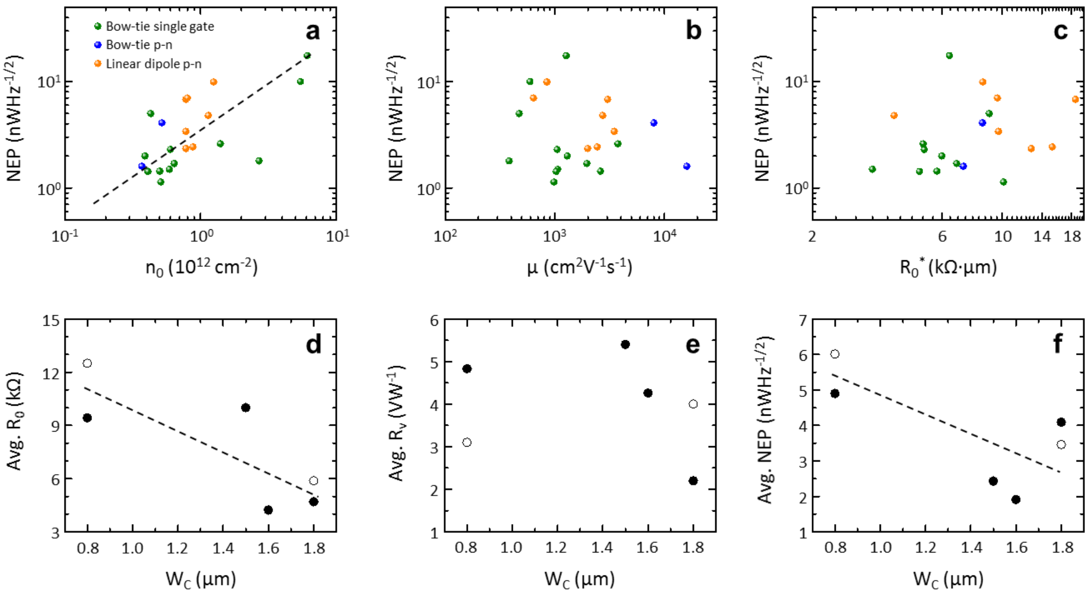

Figure 3.14: **Detection performance vs. electrical parameters and geometry.** a) Scatter plot of NEP (for air-side illumination) as a function of n_0. The dashed black line is a guide for the eye. Green points represent single-top-gated GFETs, yellow (blue) points indicate split-gate *p-n* junctions equipped with a linear dipole (bow-tie) antenna. b) *NEP vs* μ. c) *NEP vs.* R_0^*. (d-f) Device performance plotted as a function of W_c. Filled circles represent single top-gated GFETs, open circles *p-n* junction GPDs. d) Average contact resistance. e) Average R_v. f) Average *NEP*. Averages are calculated for each W_c and GPD type.

Moreover, we calculate the *NEP*'s statistical dispersion as the interquartile range (IQR) [155], defined as the difference between the upper and lower quartile of a dataset. The resultant *NEP* has a variability of 3.3 nWHz$^{-1/2}$, which is a large fraction of the mean *NEP* (4.3 nWHz$^{-1/2}$) and much larger than the minimum *NEP* (1.1 nWHz$^{-1/2}$). *NEP*'s variability then represents a critical aspect in the future development of multi-pixel arrays architectures.

To overcome this issue, we conceive a different architecture, employing ad adequate substrate treatment as well as the capping of the large area SLG by large area hexagonal boron nitride (hBN), described in the following section.

3.2. Large area SLG and SLG/ hBN heterostructures for photodetection

Here we will discuss about employment of different dielectric configurations of SLG on aluminium oxide (Al_2O_3) with and without large-area CVD hBN capping to investigate their effect on SLG thermoelectric properties underpinning photodetection.

hBN is a layered material with an atomic structure very similar to that of graphene: boron and nitrogen atoms are arranged in a honeycomb lattice with a lattice constant only 1.8% larger than graphene [156]. Because of the different on-site energies of B and N atoms, few-layer hBN has a large indirect bandgap of ~ 6 eV [157] (figure 3.15b), which makes it electrically insulating. Due to its chemical and mechanical stability, hBN is an ideal material to encapsulate or support other 2D materials, providing an atomically flat surface free of dangling bond and charge traps [158]. Indeed, hBN substrates reduces disorder and charge inhomogeneity in graphene and greatly improves its carrier mobility [158].

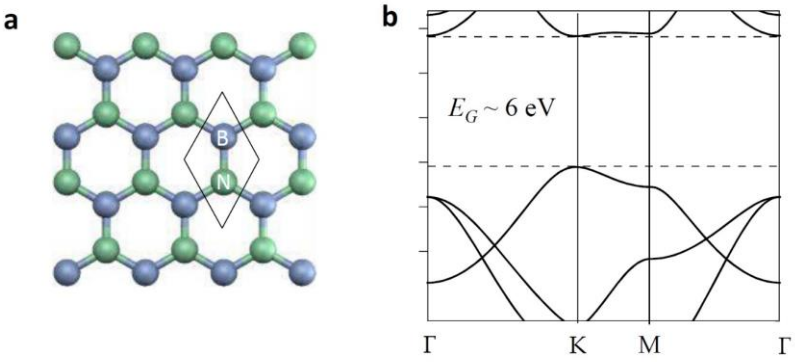

Figure 3.15: **Structural and electronic properties of hBN.** a) hexagonal lattice of monolayer hBN. The unit cell (solid black line) contains one boron atom and one nitrogen atom. b) Band structure of monolayer hBN showing a bandgap E_G of 6 eV [159].

3.2.1. Device fabrication

A ~10 nm thick layer of Al_2O_3 is deposited on SiO_2/Si substrate (resistivity~10kΩ·cm) by atomic layer deposition (ALD) (see Supplementary Information). SLG is grown in a hot wall CVD system using ~30 μm thick Cu foil as substrate. The foil, suspended on a quartz holder and loaded into the CVD system, is annealed at 1050 ^oC for 2h under H_2 gas (100 sccm) at 760 Torr and cooled down to RT. For the growth, the foil is annealed at 1050 ^oC with 50 sccm hydrogen flow at 0.4 Torr for 2h. 5 sccm CH_4 is introduced to start growth, which is completed in 30mins by stopping the CH_4 flow. The system is then naturally cooled down to RT under 50 sccm H_2 flow. As-grown SLG/Cu is spin-coated with poly (methyl methacrylate) (PMMA) (A4-950) at 1000 rpm for 1 min and baked at 80^oC for 10 mins. PMMA-coated SLG/Cu is kept in water overnight to oxidize Cu foil. PMMA/SLG is then electrochemically delaminated by applying 2 V between Pt anode and PMMA/SLG/Cu cathode in a NaOH aqueous electrolyte (~1M). The PMMA/SLG stack is cleaned in water and transferred on $Al_2O_3/SiO_2/Si$ substrates, which are then baked at 80^oC for 10mins after ~10 h natural drying. PMMA is removed by soaking in acetone and isopropyl alcohol (IPA).

hBN is grown on c-plane Al_2O_3 (0001) at 1400^oC, 500 mbar for 30 minutes in an AIXTRON CCS 2D reactor. 10 sccm N_2 is used to transport the single-source precursor, borazine, to the reactor. Before hBN growth, the sapphire substrates are annealed in H_2 atmosphere for 5 mins, at 750 mbar and 1180^oC. As-grown hBN on *c*-plane sapphire is then spin-coated with PMMA (A4-950) at 1000 rpm for 1min and baked at 80 ^oC for 10 mins. PMMA-coated hBN on sapphire is kept in ~8% H_3PO_4 for ~10 h to delaminate PMMA/hBN. This is cleaned in water and transferred on $SLG/Al_2O_3/SiO_2/Si$.

After natural drying, this is baked at 80 ºC for 10 mins. PMMA is removed by soaking it in acetone and IPA.

As-grown and transferred SLG and hBN are characterized by Raman spectroscopy with a Renishaw InVia spectrometer equipped with 100× objective at 514.5 nm. A statistical analysis of 7 spectra on as-grown SLG on Cu, 27 spectra on SLG on $Al_2O_3/SiO_2/Si$, 36 spectra on hBN/$Al_2O_3/SiO_2/Si$ and 26 spectra on hBN/SLG/$Al_2O_3/SiO_2/Si$ is performed to estimate defect density and doping (figure 3.16b).

GFETs are fabricated by means of electron beam lithography (EBL) (Zeiss UltraPlus), ALD (Oxford, OpAL) and metal evaporation. We define U-shaped channels with length L_c= 2400 nm and width W_c= 1500 nm through reactive ion etching (O_2 for uncapped, CF_4/O_2 mixture for hBN-capped samples). We pattern source and drain contacts via EBL, and fabrication is finalized by depositing a 40nm thick Pd layer by thermal evaporation and lift-off. For hBN-capped devices, this results in edge-contacts to the SLG channel, showing contact resistance R_0~1 kΩ, similar to the case of uncapped samples. We then define the top-gate oxide (~40 nm HfO_2, grown by ALD) above the channel, and finalize the fabrication by depositing 5/90 nm Cr/Au to establish the top-gate electrodes. To reduce the detector shunt capacitance, *s* and *d* electrodes are connected to a coplanar strip-line [79]. A schematic cross-section of the fabricated devices is in figure 3.16a. For each material combination, Al_2O_3/SLG/HfO_2 and Al_2O_3/SLG/hBN/HfO_2, two distinct architectures are conceived, devised and investigated. The first is based on single-top-gated GFETs integrated with a planar bow-tie antenna, with radius 24 µm and flare angle 90° (figure 3.16c,d). The antenna arms are connected to the *s* and *g* electrodes. The second design features two top-gates, connected to the left and right arms of a 24 µm radius bow-tie antenna. The antenna dimensions are chosen to be resonant with a radiation frequency of 2.8 THz [71,160].

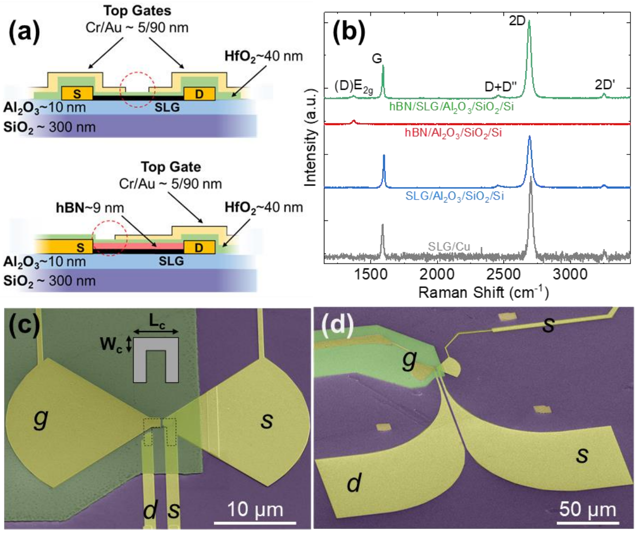

Figure 3.16: a) Schematic cross-section of the GFETs. Top: double-gated Al_2O_3/SLG/HfO_2. Bottom: single-gated Al_2O_3/SLG/hBN/HfO_2. Dashed red circles indicate the position of the THz-induced field enhancement. b) Raman spectra of as-grown SLG on Cu and SLG transferred on Al_2O_3 with and

without hBN capping. (c,d) False colour scanning electron micrographs of a single-gated device. The inset shows the U-shaped channel.

These geometries are selected to activate the PTE as dominant detection mechanism [66,79,152]. This requires a spatial asymmetry along the SD channel [59] as discussed earlier. In single-gated systems, the asymmetry is established by the spatial gradient of the electronic temperature (T_e) in the SLG channel, induced by the absorption of THz light in the antenna gap, which is located close to the *s* electrode [79]. Instead, in *p-n* junctions, the electronic distribution is symmetrically heated at the centre of the source-drain channel, where the antenna gap is located [116]. Here, the asymmetry is determined by the longitudinal variation of the SLG Seebeck coefficient (S_b), whose profile along the source-drain direction can be electrostatically defined by applying distinct V_g on the left and right sides of the junction.

3.2.2. Electrical characterization

We first characterize the devices electrically, by measuring the source-drain current (I_{sd}) as a function of V_g. The resistance (R) curve for a single-gated device is in figure 3.17a. Instead, figure 3.17b shows the resistance map of a *p-n* junction device, measured as a function of V_{gL} and V_{gR}. We extract the field-effect mobility (μ_{FE}) for electrons and holes and the residual carrier density (n_0). We get μ_{FE}=300-2000 cm^{2}V^{-1}s^{-1} for Al_2O_3/SLG-based GFETs and μ_{FE}=3000-9000 cm^{2}V^{-1}s^{-1} for hBN-capped ones.

Figure 3.17c plots n_0 as a function of μ for the complete batch of devices, where μ is the average field-effect mobility of electrons and holes: each GFET is represented by a coloured dot. From this comparison, hBN-capped samples show lower n_0 and higher μ with respect to Al_2O_3/SLG/HfO_2 devices. The field-effect measurements (figure 3.17a,b) can be used to evaluate S_b, which determines the PTE response of SLG-based PDs. This can be done starting from the experimental conductivity (σ) and using the Mott equation [78] as explained in the first section of this chapter, which, however, is not accurate at low carrier densities [85]. In fact, the Seebeck coefficient (S_b) extracted form semi-classical Mott formula fails to reproduce experimental evaluations of S_b close to the charge neutrality point (V_{CNP}), or when T_e approaches the Fermi temperature T_F (~1000 K) [85].

To study the transport properties and the thermopower (S_b) we used the linear Boltzmann equation [77,161,162], for which the Mott formula represents only a particular limit, corrected by considering the influence of electron-hole (*e-h*) puddles on the transport properties close to V_{CNP}.

Figure 3.17d shows the results of the EMT model applied to the device of figure 3.17a, for which we get a maximum thermopower S_{max}~70 μVK^{-1}.

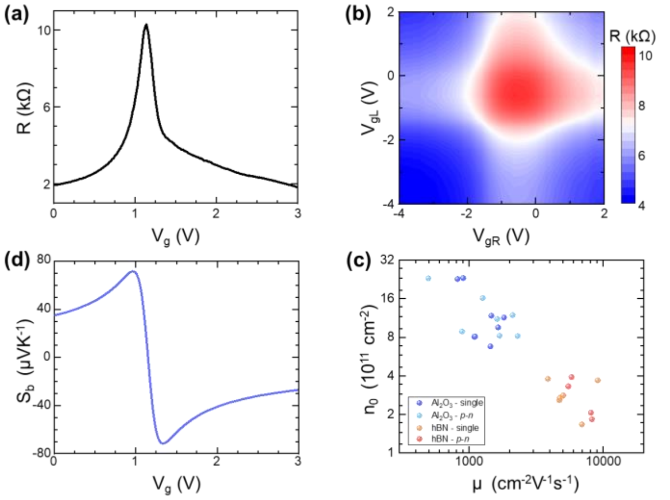

Figure 3.17: a) Channel resistance (R) *vs.* gate voltage (V_g) for an hBN-capped, single-gated GFET. b) Map of R as a function of gate voltage right (V_{gR}) and left (V_{gL}) for a hBN-capped *p-n* junction. c) Chart of carrier density (n_0) *vs.* mobility (μ_{FE}) for all the measured devices. Blue (light-blue) dots represent single-gated (double-gated) FETs without hBN-capping. Orange (red) dots represent hBN-capped single-gated (double-gated) FETs. (d) Seebeck coefficient (S_b) calculated withs the Boltzmann EMT [83,85,162] for the R curve in (a).

3.2.3. Optical characterization

We then evaluate the PDs optical figures of merit: voltage responsivity (R_v), *NEP* and τ. The detectors are illuminated by a 2.8 THz QCL, driven in pulsed mode (repetition rate 40 kHz, duty cycle 4%) delivering a peak power ~25 mW, corresponding to an average power ~1 mW. The antenna axis is oriented parallel to the linearly polarized electric field. The beam is focused by two TPX lenses onto a ~200 μm radius circular spot. We select an intermediate average power P_0=0.4 mW to characterize the PDs, to avoid QCL overheating. The corresponding average intensity in the focal point is I_0=0.32 Wcm^{-2}.

We measure the photovoltage (Δu) at the *d* electrode, while keeping *s* grounded. Δu is amplified by a voltage preamplifier (DL Instruments, M1201, gain γ=1000) and sent to a lock-in (Stanford Research, 5210). We use a square-wave envelope with frequency f_{mod}=1.333 kHz as lock-in reference and as triggering signal for the QCL pulse trains. We calculate the curve of R_v *vs.* V_g for each single-gated GFET and the map of R_v *vs.* V_{gL} and V_{gR} for each *p-n* junction. Typical examples of R_v *vs.* V_g plots are in figure 3.18a,b for a single-gated GFET and a *p-n* junction, respectively. The photoresponse in single-gated GFETs follows the profile of S_b, with an offset $S_{bu} \cong S_b$ (V_g=0 V), with PTE voltage [78] $V_{PTE}= \Delta T_e \cdot (S_b - S_{bu})$, where ΔT_e is the T_e gradient between *s* (hot) and *d* (cold) sides of the SLG channel, and S_{bu} the Seebeck coefficient of the ungated region between the *s* and *g* electrodes. Figure 3.18a compares the measured R_v *vs.* V_g and the theoretical PTE responsivity R_{PTE} *vs.* V_g, with R_{PTE} inferred from V_{PTE} by considering $\Delta T_e/P_0$ ~1.5 K/mW, showing good qualitative agreement between the two curves. The discrepancy between the theoretical and experimental responsivities at large positive V_g is ascribed to the fact that the adopted theoretical model only includes electron scattering with charged Coulomb impurities as dominant effect limiting the conductivity, possibly neglecting additional contributions, e.g. phonon scattering or carrier inhomogeneities at the contacts. A dominant PTE detection mechanism is also observed in *p-n* junctions. E_F in SLG can be tuned across the Dirac point by the electrostatic gating applied to the left and right sides of the junction. The non-monotonic dependence of S_b on E_F leads to multiple sign changes in R_v, resulting in a six-fold pattern [116] in the R_v map (figure 3.18b), a distinctive feature of PTE [124].

The sensitivity of THz detectors is evaluated through the *NEP* [116], defined as the ratio between noise figure and responsivity. Thus, we measure the GFETs NSD with a lock-in amplifier (Zurich Inst., UHFLI): the *s* electrode is grounded and the signal, demodulated by the lock-in, is collected at the *d* electrode, while a sweep of the modulation frequency is performed. The results are in figure 3.18c for a 50 Ω test resistor and for a prototypical SLG-based device. The white noise floor for the 50Ω resistor is dominated by the lock-in noise figure. The Johnson-Nyquist NSD formula gives [78] $N_J=(4k_BTR)^{½}=0.91$ nVHz$^{-½}$ for a 50Ω resistor operated at RT, whereas our instrumental noise floor is ~8 nVHz$^{-½}$, as expected for the noise level of the employed lock-in. The NSD of one of the GFETs (R=9 kΩ in figure 3.18c) is dominated by the 1/*f* component [154] for modulation frequency <1kHz and flattens at NSD <14 nVHz$^{-½}$ at higher frequencies, in agreement with the theoretically expected N_J=12.3 nVHz$^{-½}$. The GFET N_J is thus the main contribution to the overall noise figure in our setup (with pre-amplifier NSD~7 nVHz$^{-½}$). The measured NSD at 1.333kHz is then used to calculate *NEP* (figure 3.18d,e) as a function of the voltages applied to the gate electrodes.

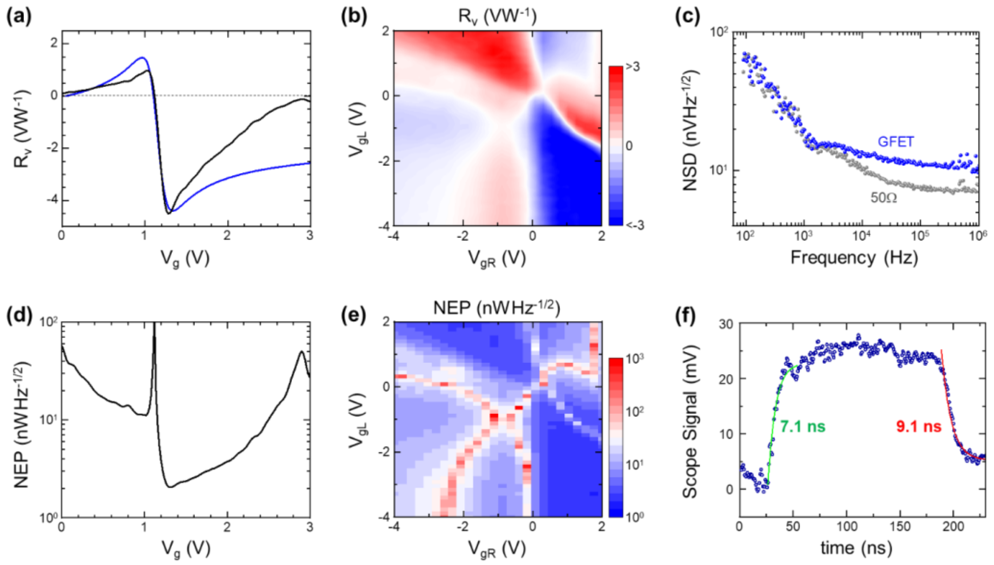

Figure 3.18: a) R_v as a function of V_g for an hBN-capped single-gated GFET. The experimental curve (black line) is compared with the theoretical PTE response (blue line), evaluated by EMT. (b) R_v map of an hBN-capped *p-n* junction, as a function of V_{gL} and V_{gR}. c) NSD of a GFET and of a 50 Ω

resistor, measured by sweeping the reference frequency of the lock-in from 100 Hz to 1 MHz. (d,e) *NEP* of a single-gated and a *p-n* junction GFETs as a function of gate voltage(s). f) Time trace of an intensity fluctuation of the QCL. The rising and falling edges are fitted with exponential functions to retrieve τ.

We then characterize the detection speed by recording the time trace of Δu with an oscilloscope (Tektronix DPO520-4B, bandwidth 2 GHz). We use a THz QCL operated in pulse mode and amplify the PD output with a high-bandwidth (1.1 GHz) voltage preamplifier (Femto, DUPVA-1-70) before the oscilloscope. We drive the QCL into the negative differential resistance regime [78], which results in electronic instabilities that correspond to an intermittent output power: the QCL undergoes intensity fluctuations with characteristic time constants τ_{qcl}~0.9 ns. This strategy allows us to test the bandwidth of our PDs up to a maximum $(2\pi\tau_{qcl})^{-1}$=180 MHz. Figure 3.18f shows the waveform recorded by a single-gated GFET during an intensity fluctuation of the pulsed QCL. We evaluate τ from exponential fits to the waveform. We get τ=7-20 ns, with a mean value ~12 ns, corresponding to a bandwidth ~15 MHz.

3.2.4. Statistical analysis of device performance

We then perform a statistical analysis on 28 devices to evaluate performance variability and identify correlations between electrical and optical properties. We first consider *NEP* variability. For Al_2O_3/SLG/HfO_2 devices, we get a mean value ~7.6 nWHz$^{-½}$ and an IQR ~4.0 nWHz$^{-½}$. For hBN-capped PDs, we have mean *NEP*~3.0 nWHz$^{-½}$ with IQR~1.4 nWHz$^{-½}$, which represents a variability improvement of a factor >2 with respect to SiO_2/SLG [147] and Al_2O_3/SLG PDs. We then evaluate correlations between *NEP*, S_b and n_0 using the Pearson coefficient (ρ) as a metric. We get $\rho(S_{max},n_0)$= −0.95 for both hBN-capped and uncapped architectures, where S_{max} is the maximum $|S_b|$ in the investigated V_g range, calculated with the EMT model. The scatter plot of S_{max} *vs*. n_0 in figure 3.19a shows that hBN/SLG/Al_2O_3 LMHs have slightly larger S_{max}, even though they have significantly smaller n_0. This is due to the different dielectric environment: the larger ε_r of HfO_2 (with respect to hBN) on top of SLG is beneficial in terms of thermopower [85]. This similarity in S_{max} is reflected in the detectors *NEP*, where the difference between the two material architectures is not as pronounced as the difference in n_0 (figure 3.19b). However, in agreement with results obtained on SiO_2/SLG/HfO_2 heterostructures, discussed in the last section of current chapter, *NEP* increases for larger n_0: $\rho(\log(NEP),\log(n_0))$=0.4. These correlations confirm that the physical mechanism underpinning THz detection is, as expected, PTE.

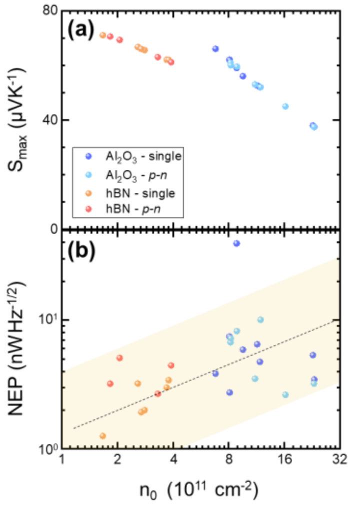

Figure 3.19: a) Scatter plot of S_{max} *vs.* n_0. Differently coloured dots identify different material/geometry combinations. S_{max} and n_0 have negative correlation. b) *NEP vs.* n_0 chart, showing positive correlation: ρ (log (*NEP*), log(n_0)) =0.4. The dotted line is a guide for the eye.

Thus, the Al_2O_3 termination alone does not show a significant performance improvement over SiO_2/Si substrates [71], whereas large-area HfO_2/hBN/SLG/Al_2O_3 LMHs present advantages both in terms of absolute optical performance (average *NEP*~3.0 nWHz$^{-½}$) and performance variability (IQR~1.40 nWHz$^{-½}$). It is worth mentioning that large area hBN-top-encapsulation significantly reduces the device performance variability by more than a factor 2 with respect to Ref. [71].

3.3. Discussion

In the beginning of this chapter I discussed on the preparation of antenna-coupled GPDs operating at 2.8 THz exploiting large area single crystal and polycrystalline CVD graphene. These combine high sensitivity (with a low *NEP*~nWHz$^{-1/2}$) and low response time (~5ns), enabled by the combination of PTE with fast readout electronics and on-chip high bandwidth architectures. These performances make them competitive with other room temperature technologies operating in the 3-6 THz range [37,98,99]. Zero-bias, zero-power consumption PTE detectors represent an undisputed advantage to meet the requirements of low cost and low SWaP (size, weight and power) of room-temperature THz cameras. The broadband nature of the PTE rectification can be exploited for multi-frequency detecting platforms. Optimization of thermoelectric properties could be achieved by transferring SLG on alternative dielectrics [59,112] to reduce the residual carrier concentration at the charge neutrality point and bring S_b in the 100 μVK^{-1} range. Indeed, the dielectric environment can strongly affect the charge inhomogeneity and the residual carrier concentration at the charge neutrality point, which, in turn, has influence on the Seebeck coefficient (and *NEP* as demonstrated in Fig. 4a). This correlation stems from the resulting graphene quality and from the different densities of free and trapped charges in the different substrates [59,112]. The possibility to combine the scalable large area CVD graphene with large area scalable hBN in scalable van der Waals heterostructures promises significant performance improvements.

In the second section of this chapter, I reported the results achieved on THz PDs realized with large-area graphene and large-area hBN in wafer-scale compliant processes, capable of mitigating material degradation with respect to the quality benchmark of hBN-encapsulated SLG [78,79,116]. We demonstrate THz detection in a layered material heterostructure obtained by consecutive transfer of CVD graphene and CVD hexagonal boron nitride, a fabrication technique that is still fully compatible with standard CMOS processing, with an average *NEP*~3.0 $\mathrm{nWHz^{-1/2}}$ and a mean value of τ ~12 ns, which reduces the device performance variability by more than a factor 2 with respect to the former reported work here.

Chapter 4: Exploitation of FETs based on InAs nanowire as photodetectors in THz regime

4.1. InAs nanowires for THz detection

Semiconductor nanowires (NWs) have proven to be efficient active materials for the development of state-of-the-art FETs operating as room-temperature THz-photo-detectors [58,163] thanks to the high electron mobility [164,165] (up to 6000 cm^{2}V^{-1}s^{-1}), the attofarad (aF) shunt capacitance [164,165], the high saturation velocity [166] (~1.3 10^7 cms^{-1} at a field of 16 kVcm^{-1}), which can easily enable high transconductance at low gate voltages and high cut-off frequency [166](~1 GHz). Moreover, the narrow bandgap and degenerate Fermi-level pinning allows for an easy formation of stable Ohmic contacts, which become increasingly important as the transistor is scaled down [167].

Furthermore, thanks to the degree of maturity achieved by growth techniques as thechemical beam epitaxy (CBE) (figure 4.1) and the molecular beam epitaxy (MBE), and the recent advancements in nano-manipulation techniques [168], semiconductor NWs can, in principle, be aligned in ordered arrays, opening the opportunity for device up-scaling toward multi-pixel THz detectors [169].

While, in the last few years, the dependence of the THz-detection performance of semiconductor NWs photo-detectors on material-related parameters (NW doping [170], carrier concentration, geometry, and/or material choice) has been widely investigated [171], a systematic study of the physical mechanisms at the base of the RT photodetection is still lacking.

Present assumptions indeed only rely on what can be indirectly inferred by mapping the gate tunable conductivity, through transport experiments or via the analysis of photo-response in antenna-integrated devices [172] or, alternatively, via an on-chip photocurrent pump-probe studies [173]. In this chapter, we first discuss about photocurrent mapping of THz radiation through scanning near-field optical microscopy (SNOM) which leads to the proper understanding of underpinned photodetection dynamics in InAs FETs, and later get advantage of these knowledges to engineer our devices in such a way that we can selectively activate different physical dynamics for THz detection.

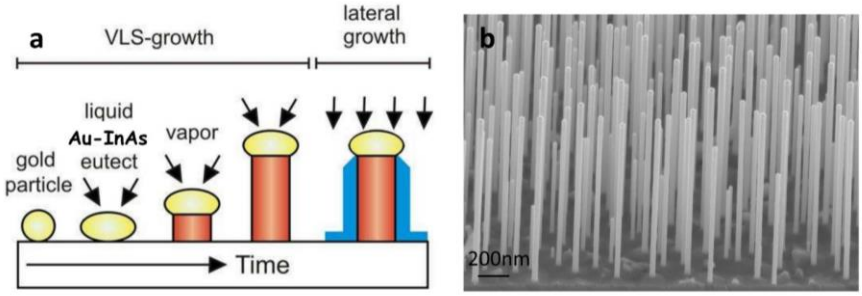

Figure 4.1: a) Schematic of gold nanoparticle-mediated epitaxy for the vapor-liquid-solid (VLS) growth of InAs nanowires via chemical beam epitaxy (CBE) technique. b) Scanning electron microscope (SEM) image of forest of grown nanowires through epitaxial approach.

4.1.1. Nanowire growth:

Semiconductor nanowires can be grown with different techniques as mentioned above. However, the devices investigated in this thesis are based on self-assembled InAs NWs, grown by CBE. The CBE technique is based on the VLS method [174] (figure 4.1), employing gold nanoparticles as catalysts for the growth [175]. For this purpose, a thin gold layer is evaporated on InAs (111)B substrates. Increasing the temperature of the chamber, small droplets of gold enucleate from the uniform bidimensional gold layer, with a typical size ranging between 3 and 150nm. The nanowires growth is then achieved by inserting the chemical precursors of the desired materials into the chamber. In the case of InAs nanowires with n-type Se doping, TriMethylIndium (TMIn) and TertiaryButylArsine (TBAs) are used as metal-organic chemical precursors, while DiTertiaryButylSelenide (DTBSe) is the source for selenium.

4.2. Scanning near field optical microscopy principle

Scattering-type scanning near-field optical microscopy (s-SNOM) is the most recently developed super resolution technique based on light scattering that is also capable of obtaining nanoscale images. SNOM is a photon-in photon-out nano-optical imaging technique that uses light to construct nanoscale images [176]. It delivers material-characteristic maps of chemical and optical properties of sample surface at the spatial resolution of an atomic force microscope (AFM). Tuning the illumination wavelength, i.e. „color“ of the light source used for measurements, provides spectroscopic information at the nanoscale. SNOM system consists of an AFM, where a sharp tip scans the sample to obtain topographical images, with added illumination of the tip-sample region. Although SNOM is a contactless technique that does not require any fluorophore labelling and is not subject to the issue of photo bleaching, it possesses other considerable challenges. Probing the near-field of a surface makes it necessary to bring a nanoscale object within the near-field of the surface. This requires finely machined tip that is able to move three dimensionally with nanometer resolution [176]. The radiation can then couple to the tip, having a nanometric radius, allowing to probe the local dielectric function of the volume of material beneath the apex through its evanescent field. Evanescent light experiences an exponential decay in the propagation direction away from the originating surface that has the consequence of localizing the near-field to a volume within ~100 nm nanometers of the originating emitter [176]. This localization produces a high intensity near-field very near the surface, which contains information about the surface properties beyond the diffraction-limited maximum resolution of the far-field. This information is encoded into the back-scattered radiation through the field component modulated by the dithering of the AFM tip at a frequency Ω. The radiation also illuminates a spot with size comparable or greater than the radiation wavelength, which leads to scattering from all objects at the focal point. This far-field contribution can be eliminated by demodulating the scattered radiation at a harmonic of Ω, as the near-field contribution is non-linearly dependent on the tip-sample distance, thus leading to the generation of a Fourier series of higher harmonics when it is decomposed from a harmonically oscillating tip (z = z0*sin(Ωt), z being the tip-sample distance) into its fourier components. Higher orders of the harmonics provide better background suppression but decrease the signal strength [177].

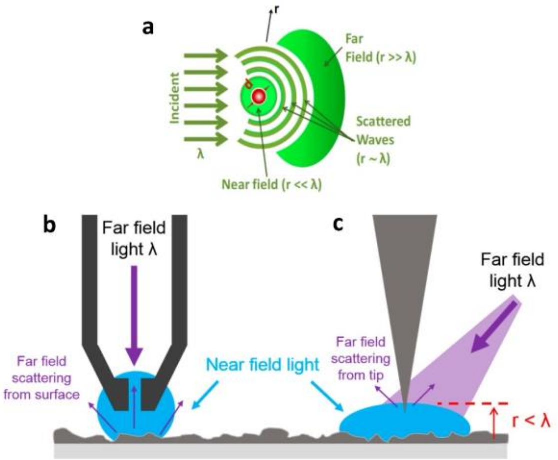

Figure 4.2: The near-field and types of SNOM tips. a) The far and near-field microscopy arrangements are defined by the proximity of the probe to the nano object being probed. When at a distance (*r*) from the emitting object that is much less than the wavelength of light used, evanescent light dominates the light field; b) Aperture SNOM where an evanescent light field created by a nanoscale opening at the end of a tip is scattered off of the surface. Light scattered from the surface is detected in the far-field. c) Apertureless SNOM utilizes near-field light emitted from the surface due to external illumination that is scattered off of a sharp tip into the far-field to be detected [176].

4.2.1. Photo-current nanoscopy

Mapping the spatial distribution of the photo-current, in the active material, represents an unambiguous way to discriminate the dominant process controlling photo-detection, since individual physical mechanisms should correspond to a distinctive profile of the light-induced photo-current. Scanning photo-current microscopy based on far-field optics has been successfully applied in the last few years to investigate local photocurrents induced by visible and near/mid infrared illumination in one-dimensional (1D) nanostructures such as NWs [178,179] and nanotubes [180–182]. Later, SNOM has been employed for inspecting charge carrier density [179,183–187], plasmons-polariton [188–191] and phonon-polariton [192–194] modes [195] with an unprecedented spatial resolution. Indeed near-field microscopy allows mapping the spatial variation and the bias dependence of local currents induced by light illumination, which enables tracking of photo-carrier transport and the electronic band bending in optoelectronic nanodevices [167].

Very recently, scattering near field optical microscopy (s-SNOM) has been exploited at THz frequencies to map photo-current in graphene [196] with sub-diffraction spatial resolution, exploiting lightning-rod effects in a metal-coated AFM tip illuminated by the THz output of a bulky, table-top, gas laser [197].

Here, we conceive and devise a compact, portable, scanning near-field system at THz frequencies capable of simultaneously perform photo-current nanoscopy [198–209] of a 1D InAs NW field-effect nanodetector, with ~35 nm of spatial resolution, corresponding to wavelength fraction < $\lambda/3000$. The system comprises a continuous-wave (CW) THz QCL coupled to a s-SNOM, and is here innovatively exploited to trace and map, unambiguously, the physical mechanisms inducing light-detection at THz frequency.

4.2.2. Device fabrication

Au-catalysed n-doped InAs NWs were grown by CBE on InAs (111) substrates (figure 4.1), using trimethylindium (TMIn) and tertiarybutylarsine (TBAs) and ditertiarybutylselenide (DtBSe) as metal-organic (MO) precursors. As-grown InAs NWs had average length of 2.3±0.5 µm and radius in the 40 -120 nm range. NW-FETs were realized with standard nano-fabrication methods. NWs were transferred from the growth substrate to the host substrate *via* dry transfer. The host substrate was a 350 µm thick intrinsic silicon wafer, capped by 500 nm of SiO_2. Individual NWs were then geometrically analysed with SEM imaging and electrical contacts were defined by aligned electron beam lithography (EBL). Before metal evaporation, a chemical wet passivation step was performed on the exposed NW areas. The ammonium polysulfide $(NH_4)_2S_x$ solution employed for this step removes the oxide layer that covers the NW before metallization, thus ensuring Ohmic metal-semiconductor contacts. The lateral-gated FETs were then finalized by the thermal evaporation of a 10/100 nm Cr/Au layer and *lift-off* (figure 4.3).

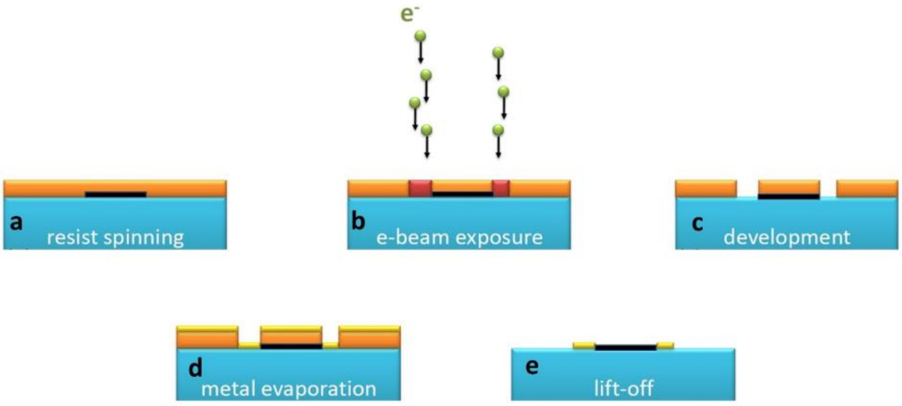

Figure 4.3: Schematic of the nanofabrication process for the finalization of InAs NW based FET. (a-e) show the consecutive processing steps of device fabrication subsequently.

4.2.3. Electrical characterization

Figure 4.4a shows the SEM images of two prototypical devices, each consisting in a single NW-FET, with source, drain and gate contacts as indicated. The two devices, labeled NW1 and NW2, differ for the gate-NW distance d (d^{NW1} = 210 nm, d^{NW2} = 267 nm) and for the channel length l (l^{NW1} = 1.95 µm and l^{NW2} = 0.86 µm). In both cases, the gate length W (W^{NW1}=1 µm and W^{NW2} = 328 nm) is smaller than the FET channel length. The FETs are preventively characterized through transport experiments, showing a stable Ohmic behavior, on-off current ratios higher than 10 (NW1) and 3 (NW2), and the lack of gate leakage through the SiO_2/Si substrate (figure 4.4c).

The conductivity σ of the two devices as a function of the V_G is reported in figure 4.4b. The resistivity ρ at V_G=0 V is equal to $\rho_0{}^{NW1}\sim$ 3 mΩ/m and $\rho_0{}^{NW2}\sim$ 1.2 mΩ/m and the transconductance g in the linear regime is g^{NW1} = 1.6 mS/m and g^{NW2} = 13 mS/m. We estimate the capacitance C between the lateral gate and the NWs for the two devices as C^{NW1}= 41 aF and C^{NW2}= 12 aF, by numerical simulation based on a finite element method (FEM) using the *AC/DC* module of a commercial software (Comsol Multiphysics). The carriers mobility µ in the two NWs can be extracted using the Wunnicke metrics [210] from the gate capacitance as $\mu = gl^2/(CV_{DS})$ giving μ^{NW1} = 740 $cm^2V^{-1}s^{-1}$ and μ^{NW2} = 505 $cm^2V^{-1}s^{-1}$ for the two devices. From the current dependence over the applied V_{DS}, we estimate the carrier density at zero gate voltage $n_e = (\mu e \rho_0)^{-1}$, where e is the electron charge, obtaining the following estimations for the two devices: n_e^{NW1} = 3×10^{16} cm^{-3} and n_e^{NW2} = 1×10^{17} cm^{-3}. The local modulation provided by the gate enables to investigate the photo-response as function of the carrier density with expected carrier density modulation of the order of 10^{16} cm^{-3}V^{-1}.

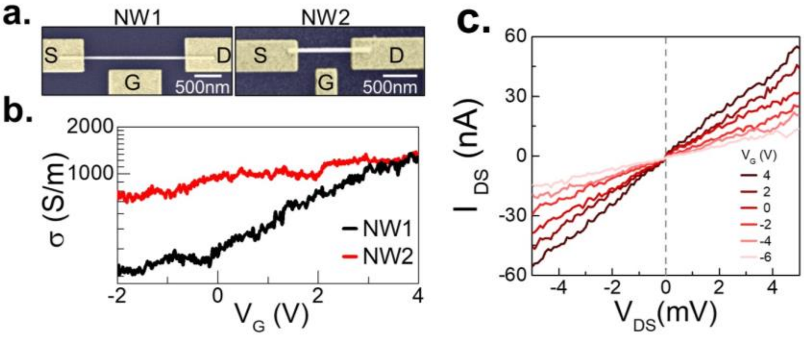

Figure 4.4: a) Scanning electron microscope (SEM) images of InAs NW field effect transistors labeled as NW1 and NW2, with source (S), drain (D) and gate (G) contacts indicated. b) Conductivity σ of NW1 (black line) and NW2 (red line) measured at room-temperature applying a drain to source voltage V_{DS}= 2 mV for NW1 and V_{DS}= 5 mV for NW2 reported as a function of gate voltage V_G. c) I-V curve of NW2 collected at different gate voltages V_G.

4.2.4. Simulation study via finite element method

Photo-current measurements, in the near field are performed combining scanning near-field THz nanoscopy with the electrical read-out at the S and D contacts of the FET, as sketched in figure 4.5a. The output of a THz-QCL emitting at 2.7 THz, operating in CW and linearly *p*-polarized, is focused on the 10 nm radius AFM PtIr coated tip of the s-SNOM. The AFM tip couples to the incident THz light which is funneled at its apex [211] and interacts with the approached sample. While performing a raster scan of the sample, we simultaneously monitor the topography with an infrared laser focused on the AFM probe cantilever, and the D-S electrical signal. Specifically, we detect the D-S photo-voltage ΔV when no V_{DS} is applied (V_{DS} = 0 V) using a high input impedance (R=100 MΩ), low-noise voltage amplifier, or, alternatively, the photo-current ΔI, for finite V_{DS}, by using a low input impedance (R=50 Ω), low-noise (50 fA) transimpedance amplifier. The near-field photo-excitation with the CW THz-QCL field funneled by the AFM tip produces a strongly localized heating in the NW, caused by THz photon absorption through intraband transitions. Conversely, interband absorption can be discarded considering that the ∼356 meV energy gap of InAs [212] largely exceeds the THz photon energy (11.2 meV). The absorbed heat results into finite thermal gradients of both electron T_e and phonon T_{ph} temperatures along the NW axis, dependent on the AFM tip position.

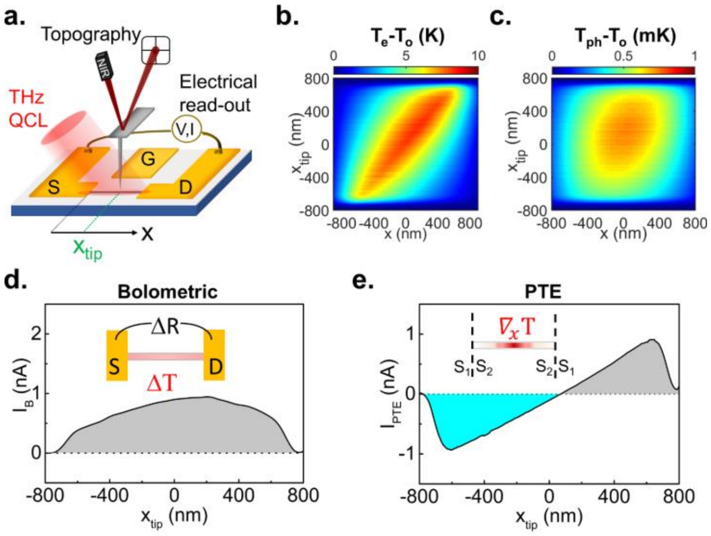

Figure 4.5: a) Sketch of the photo-current nanoscopy experiment. A THz-QCL coupled to the AFM tip of a s-SNOM photo-excites a single InAs NW integrated into a FET. Source (S), drain (D) and gate (G) contacts are marked on the graph. In the experiment, the S-D signal is monitored together with the sample topography. (b-c) Simulated local increase of the electron T_e (b) and lattice T_{ph} (c) temperatures with respect to room-temperature T_o = 296 K, induced by photo-excitation in a NW of length 1.4 µm, diameter of 80 nm and center in x = 0, as a function of the position x along the NW axis, and of the position x_{tip} of the tip scanning the sample. (d-e) Simulated photo-current profiles induced by the bolometric (d) and by the PTE (e) effects as a function of the tip position x_{tip}.

Therefore, in order to predict the temperature profiles during a sample scan, we first simulated the electromagnetic field distribution along the NW via FEM simulation as a function of the tip position x_{tip} (figure 4.6). Interestingly, the simulated THz field power is maximum below the tip apex and at the NW/electrodes interfaces. The electrons T_e and phonons T_{ph} temperatures corresponding to a given x_{tip}, *i.e.* to a given distribution of the THz field, are then estimated by solving the 1D heat-diffusion model along the NW, including the heat exchange with the substrate [81] (figure 4.5b,c). While the retrieved T_e profiles along the NW axis are peaked at x_{tip} (figure 4.5b), the T_{ph}, which describes the lattice temperature increase due to the coupling with the hot electron bath, presents a broader profile, less dependent on x_{tip} and peaked at the NW center. The photo-current signal at each x_{tip} is finally calculated from these temperature profiles, assuming thermally-driven effects: bolometric and PTE photo-currents. The bolometric (I_B) and thermoelectric (I_{PTE}) photo-currents as a function of x_{tip} are reported in figure 4.5d,e following the expressions:

$$\begin{aligned} I_B &= \int_{-l/2}^{+l/2} \frac{d\sigma}{dT}(T_{ph} - T_0)\frac{dV}{dx}dx \\ I_{PTE} &= \int_{-l/2}^{+l/2} \sigma S_e(T_e)\frac{dT_e}{dx}dx \end{aligned} \tag{4.1}$$

where σ is the electrical conductivity, S_e is the Seebeck coefficient and x spans the NW length l. The two effects exhibit consistently different photocurrent profiles. The expected near-field photo-current profile of I_B (figure 4.5d) resembles the bell-shaped trend of T_{ph}, with a maximum at the NW center and constant polarity. On the contrary, the PTE voltage V_{PTE} and the current $I_{PTE} = \sigma V_{PTE}$ exhibits a sign change along the NW, with zero signal at the NW center. The bolometric current I_B results from the variation of σ with T_{ph}, quantified by the bolometric coefficient $\frac{d\sigma}{dT}$. Differently from PTE, I_B could arise also when the device is homogeneously heated ($\nabla \cdot T = 0$) and depends only on the temperature variation with respect to the dark condition (T_o= 296 K). The polarity depends on the sign of the bolometric coefficient, which is negative (positive) for a degenerate (non-degenerate) semiconductor.

The PTE response instead emerges thanks to the combination of a finite T_e gradient induced by the local photo-excitation, and to a spatially varying Seebeck coefficient S. For the InAs NWs, a Seebeck coefficient $S_e^{NW}\ -150\mu VK^{-1}$is extrapolated from the transfer characteristics in good agreement with a recent study of the temperature dependence of the transport properties of InAs NWs [213]. On the other hand, the Au electrodes have $S_e^{Au}\sim\ 0\mu VK^{-1}$, such that the interface electrodes/NW acts as a thermocouple, able to translate temperature gradients into an electrical signal. When the tip is at the center of the NW, the two opposite PTE-currents originating at the S and D electrodes cancel out, resulting in a clearly zero signal (figure 4.5e). The maximum PTE signal appears at finite distance from the metal/NW interface since the difference (T_e-T_o) reaches its minimum on the metallic electrodes. The photo-voltaic mechanism is not considered for InAs NW because the THz incident photon-energy is not compatible with interband transitions photo-exciting electron-hole pairs. As expected, simulations confirm that the different photo-detection mechanisms that can come into play in InAs NW correspond to clearly distinguishable near-field photo-current profiles.

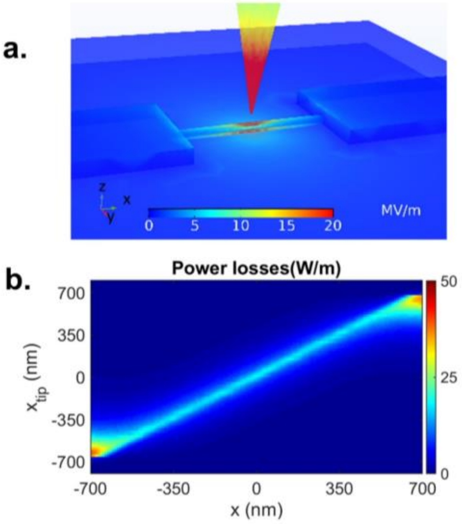

Figure 4.6: Electric field *E* distributions computed with COMSOL Multiphysics for incident p-polarized field of 100 mW at 2.7 THz. a) zoom of the *E* maps around the NW showing the cylindrical NW, the tip at x_{tip}= 0 nm, the drain and source electrodes and the SiO_2 substrate. b) Power losses linear density as function of *x* position along the NW axis and of the tip position x_{tip} obtained integrating the power losses density *F*(x,y,z) in the circular cross section of the NW in the plane zy.

4.2.5. Spatial resolution and far field background

In our nanoscopy experiments, the tip is operated in tapping mode with oscillation frequency Ω. The near-field signal depends non-linearly on the tip-sample distance, as it is shown in figure 4.7. Increasing the demodulation order, the signal decreases and we observe the virtual tip sharpening effect [214]. To find a good compromise between signal intensity and suppression of the background due to non-local scatterers, we chose the 2nd order to analyze the photocurrent maps, being *n*=2 the lowest order Fourier component at which the signal reaches the noise level once approaching the tip from the sample. The decay distance $h_{1/2}$ at which the amplitude signal has decayed by a factor of 2, is also shown.

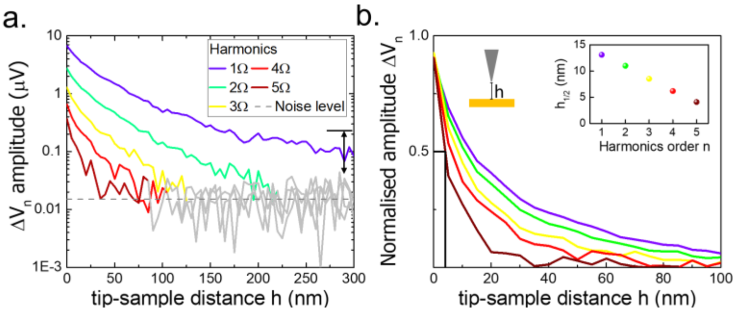

Figure 4.7: Approach curves at the different harmonics recorded on the InAs nanowire NW1 reported in semi-logarithm scale (a); and in linear scale to calculate the distance h1/2 (inset) at which the normalized signal drops to half of its maximum (b).

We characterize the signal amplitude s_n and lateral resolution Δ*x* by analyzing the line profiles across the interface between the electrodes and the nanowire in the case of the photo-current signal.

We define the spatial resolution in analogy to other microscopy techniques as the full width at half maximum (FWHM) of the line spread function (LSF). The LSF can be calculated by taking the derivative of the line profile measured across an interface. The black dots in figure 4.8 show the line profile across the source and nanowire interface, from which we extract the first derivative (in the inset), fit with Lorentzian functions with FWHM of 35 ± 2nm, which indicate a spatial confinement of the THz field of the order of $\lambda/3000$.

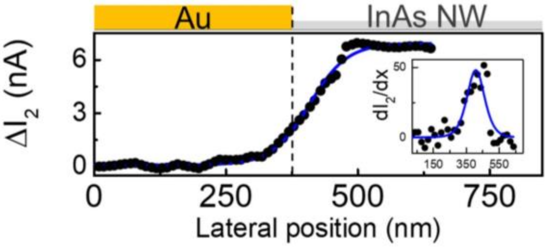

Figure 4.8: Spatial resolution of s-SNOM measurements. b) THz near-field photocurrent ΔI_2 (black dots) across source-electrode/NW interface together with the best fit using Boltzmann edge function (solid blue line); the first-derivative of ΔI_2 is reported in the inset together with the Lorentzian fit function (blue line) to estimate lateral spatial resolution.

4.2.6. Photo-current characterization

To perform photo-current nanoscopy experiments, we operate our s-SNOM tip in tapping mode, with an oscillating frequency Ω. In order to isolate the component of the electrical signals due to the near-field photo-excitation, *i.e.* induced solely by the light scattered by the tip, the signals are demodulated at high harmonics of the tapping frequency $\Omega_n = n\Omega$, *i.e.* at an order n in the range $n = 2–5$. First, we collected near-field maps while setting $V_{DS} = 0$ V on sample NW1, with S grounded and collecting ΔV

at the D electrode, as sketched in figure 4.9a. ΔV is the superposition of signals oscillating at the tapping frequency Ω and at its harmonics ΔV_n: $\Delta V = \sum_{n=0}^{5} \Delta V_n = \Delta V_0 + \Delta V_1 + \Delta V_2 + \ldots$; the second order ($n = 2$) component ΔV_2 is shown in figure 4.9c for different values of V_G. A finite value is reported only when the tip scans the portion of the NW which is not covered by the metallic electrodes. Indeed, the THz near-field is screened by the metal contacts, failing to photo-excite the portion of NW buried beneath. The horizontal cut of each individual photo-voltage map, taken by averaging over 50 nm (5 pixels) around the NW center (as identified by the topographic image in figure 4.9a), is shown in figure 4.9e.

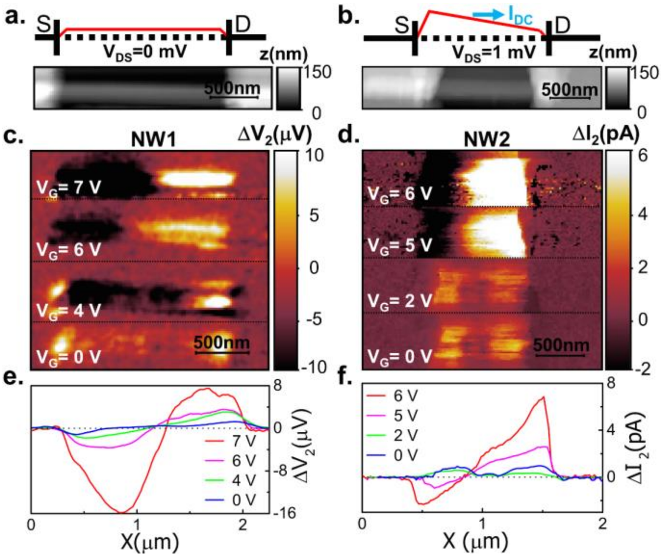

Figure 4.9: THz near-field photocurrent maps. (a-b) Sketches of the applied fields on the FET channel of NW1 with an applied $V_{DS} = 0$ V (a) and of NW2 with $V_{DS} = 1$mV (b) together with the topographic maps (in grey scale) of the two FETs. c) Near-field second-order photo-voltage ΔV_2 maps of NW1 with $V_{DS}= 0$ V and at different gate voltages in the range V_G = 0V-7V. d) Near-field second-order photo-current maps ΔI_2 of NW2 with $V_{DS}= 1$ mV and V_G in the range 0V-6V. e) ΔV_2 profiles of NW1 at different V_G obtained by averaging the horizontal cuts of the maps in panel (c), over a 50 nm range around the NW1 center. f) ΔI_2 profiles of NW2 at different V_G obtained by averaging horizontal cuts of the maps in panel (d), over a 50 nm range around the NW2 center.

In the near field maps and line profiles, the photo-voltage exhibits a phase-change along the NW, it increases in amplitude approaching the contacts and becomes negligible at the NW center, as expected when photo-detection is governed by the PTE. Moreover, the signal progressively increases with V_G, while the position of zero-signal along the NW axis remains practically unperturbed. Since V_{DS} = 0 V, we can here only probe the photo-voltage signal that is directly generated by photo-excitation, as in the case of PTE or PW, but we are not sensitive to any photo-induced variation of the conductivity, *i.e.* to any bolometric effect.

Accordingly, we repeat the same measurements on the NW2, as sketched in figure 4.9b while applying V_{DS} = 1mV at the S contact, corresponding to a *DC* dark current of ∼ 5 nA. The near-field maps and line profiles, corresponding to the second order (n = 2) component of the photo-current ΔI_2 are shown in figure 4.9d,f respectively. Since the signal is acquired from D, positive photo-current corresponds to a current flowing from S to D. At V_G = 0 V, as we illuminate the NW2 with THz-light, we observe a ΔI_2 signal with constant polarity along the whole NW, with only small intensity modulations, that resembles the expected response for bolometric effect, plotted in figure 4.5d. Since the number of carriers contributing to the conduction is not affected by THz-light absorption, the conductance change associated with the observed bolometric photo-current can be ascribed to a temperature induced mobility variation. Interestingly, by increasing V_G above the *pinch-off* ($V_G >$ 2.5V), the photo-current maps drastically change and the phase jump, distinctive of the PTE, reappears. The enhancement of the PTE, that eventually dominates at high carrier densities, overwhelming the bolometric response, is encoded in the dependence of S_e on the carrier density n_e, which determines the increase with V_G. To elucidate the interplay between the bolometric effect and the PTE, we explore the dependence of the photo-current signal in the NW2 in two opposite regimes: when the photo-response is dominated by the PTE (V_G= 6 V) and when the bolometric effect is dominant (V_G= 0 V). Figure 4.10 shows the ΔI_2 maps and the related horizontal cuts as a function of the incident THz-field power P and as a function of V_{DS}. The incident power is progressively increased by varying the bias applied to the THz-QCL heterostructure, and it is measured with a calibrated power meter (Thomas Keating THz Absolute Power & Energy Meter System) placed at the entrance of the s-SNOM. To better quantify how the incident power affects the retrieved near-field signals, we integrated the horizontal line profiles, extrapolating the area underneath. In the PTE regime (figure 4.10a-f), the signal increases with the incident power (figure 4.10e) and remains almost constant while varying V_{DS} up to V_{DS} = 10 mV (figure 4.10f). Conversely, in the bolometric regime, figure 4.10g-l, the near-field photo-current increases super-linearly with the incident THz power (figure 4.10k) and linearly with V_{DS} (figure 4.10l).

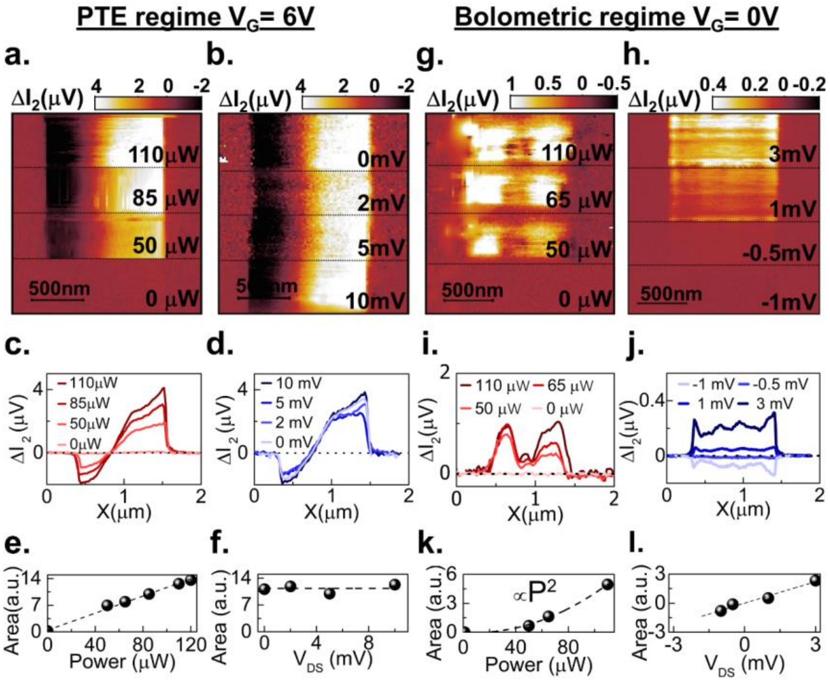

Figure 4.10: Evolution of the retrieved photo-current signals. (a-b) Second-order photo-current ΔI_2 maps of NW2 in the PTE regime (gate voltage V_G = 6V) as a function of the incident THz power P at fixed source-drain bias V_{DS} = 5mV (a), and, as a function of V_{DS} at a fixed P = 100 μW (b). (c-d) ΔI_2 linear profiles, in the PTE regime, extracted by averaging horizontal cuts of panels (a-b) in a 50 nm range around the NW center**.** (e-h) Integrated areas, in the PTE regime, underneath the ΔI_2 profiles shown in panels (c), (d). (g-h) ΔI_2 maps of NW2 in the bolometric regime (gate voltage V_G= 0V) as a function of P at fixed V_{DS} = 10mV (g), and as a function of V_{DS} at a fixed P =100 μW (h). (i-j) ΔI_2 linear profiles in the bolometric regime, extracted by averaging horizontal cuts of panels (g-h) in a 50 nm range around the NW center**.** (k-l) Integrated areas, in the bolometric regime, underneath the ΔI_2 profiles shown in panels (i), (j).

4.2.7. Conclusions

In this chapter section, I have presented photo-current nanoscopy experiments at THz frequency, conceived to identify the main photo-detection mechanisms in InAs NW FETs. Once impinging the radiation of a THz QCL source on the s-SNOM AFM tip we capture snapshots of the photo-current flowing in the strongly subwavelength NW section and we retrieve clear signatures of two thermally-driven processes: the PTE and the bolometric effects. The interplay between these two mechanisms is discussed as a function of the carrier density, V_{DS} and incident THz-power. Interestingly, PTE dominates at high carrier density, owing to the positive correlation between the temperature gradient and the Seebeck coefficient. Detection supported by PTE allows operation without any applied voltage, but the response to the incident power remains linear, as opposed to the super-linear scaling visible under a bolometric response. The achieved results provide a route for engineering THz photodetectors with large quantum efficiencies and inherently high speeds, which could be attained by favoring the formation of light-induced thermal gradients along the NW axis to exploit the highly efficient photo-thermoelectric response of InAs NWs, and by the inherently small attofarad capacitance.

The photo-current distributions and polarities corresponding to the two effects are consistently different, making photo-current nanoscopy a very valuable tool to investigate photo-conduction in low-dimensional materials.

In the next section of this chapter I will demonstrate how the achieved results can pave the way to design sensitive THz detectors based on InAs NWs FETs through the different architecture of an on-chip resonant antenna, or dynamically by varying the NW carrier density through electrostatic gating.

4.3. On-chip antenna-coupled InAs FETs as sensitive THz detectors

In this work, taking advantage of the physical understanding of the core detection dynamics in semiconductor nanowires FETs, retrieved via near-field THz nanoscopy [167,215], we design InAs NW-based THz detectors where the activation of the BE and PTE can be selected by the antenna design and even dynamically tuned across a transition between the two mechanisms by simply changing the NW carrier density through electrostatic gating.

4.3.1. Device design and fabrication

Homogeneous Se-doped InAs NWs are integrated within lateral dual gated FETs, as shown in figure 4.11b. NWs are first transferred through a mechanical dry-transfer approach from the growth substrate over a 300nm/350μm SiO2/intrinsic silicon host wafer. Subsequently, source (S), drain (D) and gate (G) electrodes are defined by means of an aligned electron-beam lithography (EBL) procedure, Cr/Au (10/100 nm) thermal evaporation and lift-off. The detectors are then mounted and wire-bonded on dual inline packages.

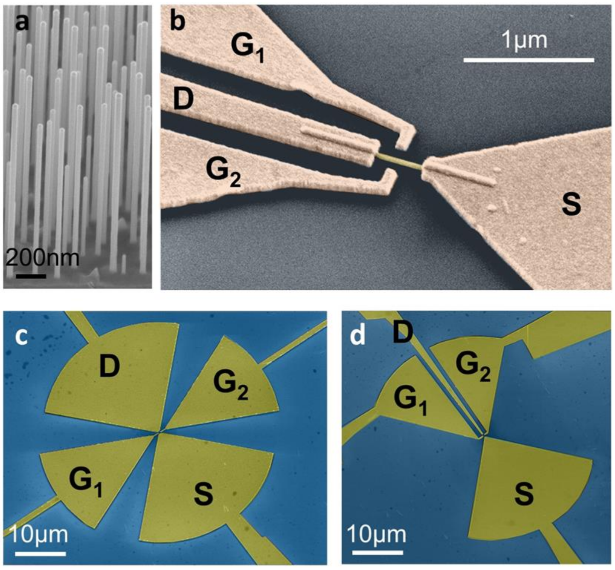

Figure 4.11: a) 45° tilted scanning electron micrograph (SEM) image of the as-grown InAs NW forest. The scale bar corresponds to 200 nm. b) False colour SEM image of the fabricated lateral-gate NW-FET (asymmetric configuration). (c,d) False colour SEM pictures of two NW-FETs in the s-FET (c) and a-FET (d) configurations.

In order to activate different detection mechanisms, we design two distinct device geometries: a symmetric FET configuration (s-FET, figure 4.11c), where the S and D electrodes are connected to the two arms of a planar bow-tie antenna, and an asymmetric configuration (a-FET, figure 4.11b,d), where the S and G electrodes are connected to the antenna arms, with the D electrode defined as a thin wire between the dual lateral gates. The total length of the bow-tie antennas (L = 44μm) is selected through electromagnetic simulations performed with a finite element method (FEM) in a commercial software (COMSOL Multiphysics) [78].

In s-FETs, the THz energy is symmetrically driven to the NW, whose temperature is expected to rise homogeneously as a consequence of free-carrier absorption [88]. Instead, in a-FETs, the bow-tie produces a THz-induced field enhancement at the S-side of the NW, generating a thermal gradient along it. Therefore, the two configurations should in principle favour the onset of different physical mechanisms [167], the BE in the s-FET and the PTE in the a-FET.

4.3.2. Electrical characterization

The transport characteristics of the designed NW-FETs are measured with two *DC* voltage generators (Keithley2400) to drive the V_{SD} and V_G, (kept identical for G_1 and G_2), while monitoring the current (I_{SD}) through the NW channel. In the employed electrical setup, the heat sink temperature (T_0) can be set and monitored by the combination of a heater and a temperature sensor, allowing the control of the device temperature during operation. Figures 4.12a,b show the I_{SD} *vs* V_G curve collected for the two samples in the two different antenna configurations, recorded at two different temperatures, 298 K and 330 K. We then estimate the transconductance (g) curve as the first derivative of the I_{SD} *vs* V_G characteristic, from which we can retrieve the field effect mobility (μ_{FE}) and the pristine carrier density (n_0) of the individual NWs. Indeed, μ_{FE} can be estimated from the maximum transconductance (g_m) using the formula [172] $\mu_{FE} = g_m w_G^2/(C_{wG}V_{SD})$, where w_G is the gate width and C_{wG} is the gate-to-channel capacitance; n_0 can be calculated as [172] $n_0 = C_{wG}V_{th}/(e\pi r^2 w_G)$, where V_{th} is the NW-FET threshold voltage, e is the elementary charge and πr^2 is the cross-sectional area of the NW, approximated as a cylinder. Importantly, the estimation of both parameters requires the knowledge of C_{wG}. For the two different architectures, C_{wG} is simulated using a commercial software (COMSOL Multiphysics). We obtained $C_{wG} = 12.3$ aF for the *s*-FET and $C_{wG} = 18.1$ aF for the *a*-FET.

Figures 4.12a,b also show that, for samples with $n_0 \gtrsim 5\times10^{17}$ cm^{-3}, μ_{FE} decreases when increasing T_0 and at large and positive V_G the conductivity (σ) decreases when increasing T_0, i.e. beyond a specific V_G the NW behaves as a degenerate semiconductor. For samples with $n_0 \lesssim 5\times10^{17}$ cm^{-3}, μ_{FE} is instead slowly varying with T_0. In both cases, n_0 increases with T_0 as a consequence of the thermal activation of surface donors [216].

Figure 4.12c presents a scatter plot of the as-obtained values of μ_{FE} and n_0 for the devised NW-FETs, at 298 K. μ_{FE} ranges from 80 to 650 cm^{2}V^{-1}s^{-1} while n_0 ranges from 0.8 to 20×10^{17} cm^{-3}. This latter spread in the carrier density is a combined effect of ambient pressure exposure, processing-related factors and different nanowire morphologies (e.g. diameter) [168].

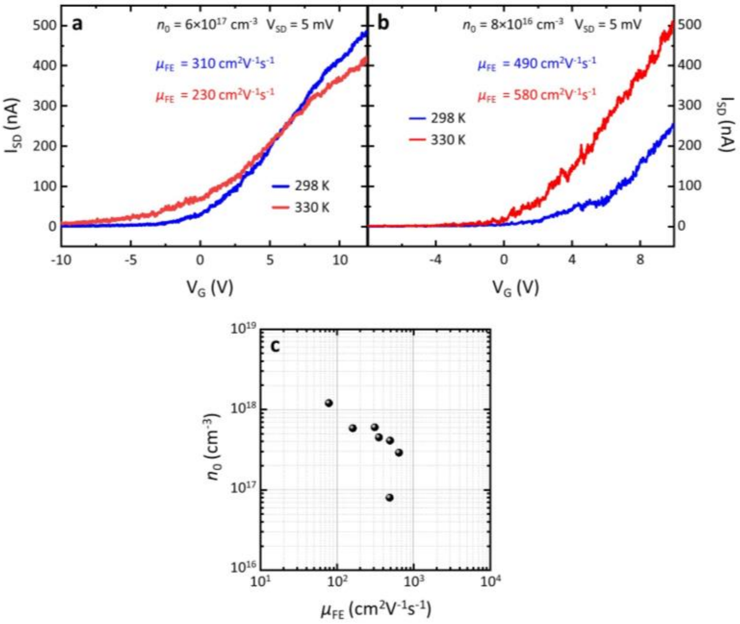

Figure 4.12: (a,b) I_{SD} *vs* V_G curve collected at $V_{SD} = 5$ mV at two distinctive temperatures, 298K and 330K, measured in the *s*-FET (a) and in the *a*-FET (b) with $n_0 = 6\times10^{17}$ cm^{-3} (a) and $n_0 = 8\times10^{16}$ cm^{-3} (b). c) Chart of n_0 *vs* μ_{FE}: every point corresponds to a different device.

4.3.3. Antenna characterization

The optical characterization of the investigated NW-FETs is performed by employing the experimental setup shown in figure 4.13a. A linearly polarized 2.8 THz wave is generated by a quantum cascade laser (QCL), refrigerated at an heat sink temperature of 30K by a Stirling cryocooler (Ricor K535) and operated in pulsed mode (40 kHz repetition rate, duty cycle 4%), capable of delivering to the detector an average optical power P_o ~1.1mW, calibrated with a power meter (Ophir 3A-P-THz). The divergent QCL beam is first collimated by a TPX (polymethylpentene polymer) lens with 1’ focal length and then focused by a TPX lens with 2’ focal length in a circular focal spot of radius ~200 µm (evaluated as full width at half maximum), as retrieved by the measured beam profile in the focal point (figure 4.13b). The QCL power in the focal point is set to P_o =400 µW, which corresponds to a THz intensity I_o= 0.32 Wcm^{-2}. The detectors are mounted on a x-y-z motorized stage and a rotational stage employed to manually adjust the polarization (α), azimuthal (φ) and elevation (θ) angles.

The measured photovoltage (Δu), recorded at the D electrode while keeping S grounded, is then pre-amplified with a voltage preamplifier (DL Instruments M1201, gain G=1000) and sent to a lock-in (SR5210). We use as lock-in reference a modulation frequency of 1.333 kHz, which is also used as square-wave-envelope for the QCL pulses. Δu can be inferred from the lock-in reading (V_{LI}) via the relation [58] $\Delta u = 2.2 \times V_{LI}/G$. Figure 4.13c shows the dependence of the photocurrent recorded with one of the NW-FET detectors as a function of P_o, demonstrating the NW-FET linearity.

We then characterize the response of the two antenna configurations with respect to the polarization angle by measuring Δu while the sample is rotated on the antenna plane, around the beam propagation direction. The polarization responses for the *s*-FET and *a*-FET are reported in figure 4.13d: in both cases, the signal is maximum when the antenna axis is parallel to the THz electric field (α=0°).

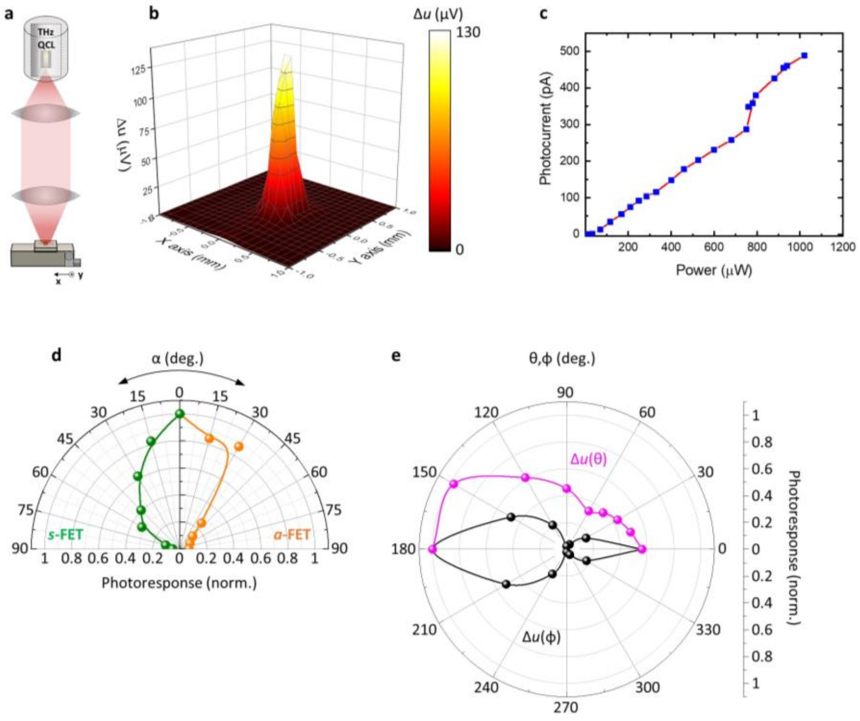

Figure 4.13: a) Schematic of the experimental setup for optical characterization. b) Intensity profile measured with an *s*-FET in the focal point. c) Dependence of the detector's photocurrent from the input optical power. d) Polar plot of the normalized photoresponse, recorded as a function of the angle (α) between the light polarization and antenna axis for symmetric (green) and asymmetric (orange) antennas. e) Antenna radiation pattern measured as a function of azimuth angle (φ, black dots) and elevation angle (θ, magenta dots). The direction (θ=0°, φ=0°) is pointing out of the substrate, perpendicularly to the antenna plane.

We evaluate the antenna directivity D_0, by recording Δu as a function of the angles φ (H-plane) and θ (E-plane). Figure 4.13e shows the results retrieved with an *a*-FET. The antenna directivity in a given direction (θ,φ) is defined as the ratio between the antenna radiation intensity in that direction and the radiation intensity averaged over all directions. The directivity is therefore evaluated in the direction orthogonal to the antenna surface and pointing out of the silicon substrate $(\theta,\varphi) = (0,0)$ as $D_0 = \Delta u(0,0)/\langle \Delta u(\theta,\varphi)\rangle = 3.75$, where $\langle ... \rangle$ represents the average of the photovoltage over an angle of 4π, which is calculated as a series approximation, assuming that the variations over θ and φ are separable [217].

4.3.4. Optical characterization

As mentioned in chapter 1, in order to be able to evaluate R_v, we first need to measure the optical power impinging onto the detector (P_a) which is related to the intensity in the focal point through the detector effective area (A_{eff}), as $P_a = I_o \times A_{eff}$. We calculate A_{eff} as the diffraction limited area [58] A_{eff} =

$\lambda^2/4 = 2800$ μm^2, where λ is the free-space wavelength. We note that, from the knowledge of D_0, it is possible to evaluate the effective area using a different formalism [218]: $A_{eff} = D_0\lambda^2/4\pi = 3300$ μm^2. Thus, in the present geometry, there is a <20% difference in the estimation of A_{eff} between the diffraction limited method and the antenna directivity method.

The plot of R_v as a function of V_G for the investigated *a*-FETs (figure 4.14a), displays a signal-to-noise ratio SNR > 600. The R_v curve shows a non-monotonic trend, which we ascribe to the non-trivial interplay of the BE and PTE mechanisms. The bolometric photovoltage Δu_B is expected to be proportional to the quantity β/σ, where σ is the static conductivity and $\beta=\mathrm{d}\sigma/\mathrm{d}T_0$ is the bolometric coefficient, which quantifies the sensitivity of the electrical conductivity with respect to a temperature change [219]. Thus, from the measurement of $\sigma(V_G)$ at different temperatures it is possible to extrapolate $\beta(V_G)$. The expected trend of $\Delta u_\mathrm{B}(V_G)$ is reported in figure 4.14a as a grey curve overlaid to $R_v(V_G)$. Interestingly, the bolometric effect can explain the photoresponse only for $V_G< 3$V, whereas at higher V_G another physical mechanism seems to dominate. To verify this conclusion, we extrapolate the detector photocurrent by quantifying the change of the I_{SD} *vs* V_{SD} characteristic between the illuminated state (THz-on) and the dark state (THz-off), while keeping S grounded and while sweeping V_{SD}. At V_G=-2V (figure 4.14b), the THz-on and THz-off traces are almost overlapped and the effect of THz radiation is visible only as a positive change of the NW conductivity $\Delta\sigma/\sigma = 4\%$, i.e. an increase of σ when the system is heated by the THz beam. At V_G=11.3V, instead, there is a rigid shift of the I_{SD} *vs* V_{SD} characteristics towards positive currents, as a consequence of an additional electromotive force along the channel, which pushes electrons from S to D. We ascribe this contribution to the PTE-driven photocurrent: $I_{PTE} =-\sigma S_b\nabla T_0$, where S_b is the NW Seebeck coefficient and ∇T_0 is the THz-induced (positive) thermal gradient between the D (cold) and S (hot) electrodes, resulting in $I_{SD} = \sigma(V_{SD} - S_b\nabla T)$ [220] (here a positive V_{SD} corresponds to a negative electrostatic voltage gradient from D to S). Importantly, for $V_G> 3$V, the BE is still observable in a negative $\Delta\sigma/\sigma = -5\%$, in agreement with the expected trend of $\Delta u_\mathrm{B}(V_G)$.

A different behaviour is observed in *s*-FETs (figure 4.14d). In this case, R_v decreases as a function of V_G, qualitatively following the trend of $\Delta u_\mathrm{B}(V_G)$ over the whole gate voltage sweep. This indicates that, in symmetric architectures, the photoresponse is mainly driven by the BE. Figure 4.14e shows the variation of the I_{SD} *vs* V_{SD} characteristics between the illuminated and dark states, testifying a huge change in the NW conductivity upon illumination, $\Delta\sigma/\sigma = 25\%$.

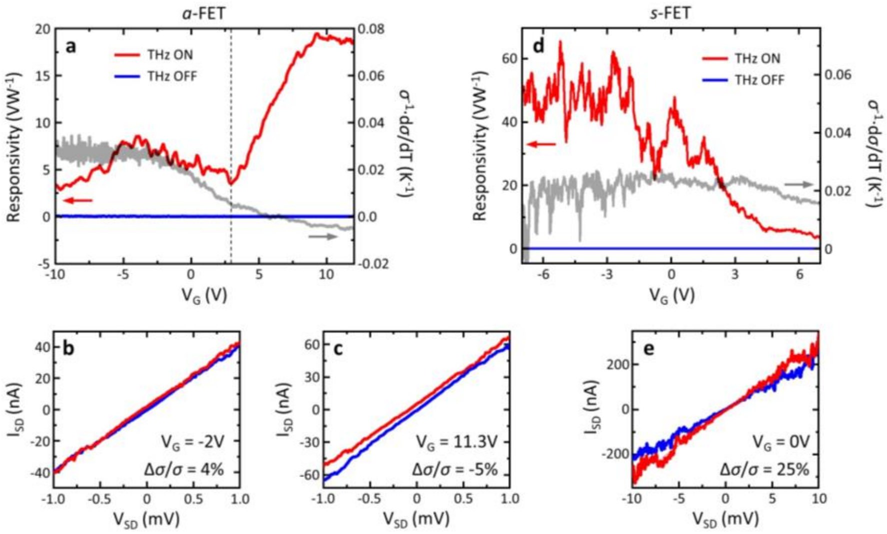

Figure 4.14: a) Left vertical axis: R_v measured as a function of V_G, in a prototypical *a*-FET; the blue line shows the noise level when the THz beam is blanked. Right vertical axis: expected trend of $\Delta u_B(V_G)$, calculated from the transconductance characteristics measured at different heat-sink temperatures. The dashed vertical line indicates the value of $V_G > 3$V where the PTE contribution starts to dominate the photoresponse. (b,c) I_{SD} *vs* V_{SD} traces recorded for the *a*-FET in the illuminated (red) and dark (blue) states at different V_G. d) Left vertical axis: $R_v(V_G)$ measured for a *s*-FET. Right vertical axis: expected trend of $\Delta u_B(V_G)$. e) I_{SD} plotted as a function of V_{SD} measured at V_G= 0V. All the measurements have been collected at room temperature.

4.3.5. Detector performance

To assess the detector sensitivity, we evaluate *NEP* as the ratio between the noise spectral density (NSD) and R_v. We measure the root mean square of NSD by connecting the detectors to a lock-in amplifier and employing an internal oscillator frequency (f) sweep technique [168]. The amplitude of the as-measured NSD is reported in figure 4.15a for the *a*-FET (sample corresponding to figures 4.12a and 4.14a). The noise figure is dominated by the flicker noise for $f < 4$kHz, whereas it flattens close to the thermal noise floor (Johnson-Nyquist noise N_J) at higher frequencies. At the modulation frequency employed in our experiments f=1.333kHz, the NSD is $\sim 2N_J = 2\times(4k_B R T_0)^{1/2}$, where k_B is the Boltzmann constant and R is the NW resistance. From the knowledge of NSD we found a minimum *NEP* = 2nWHz$^{-½}$ among the tested *a*-FETs and a minimum *NEP* = 670pWHz$^{-½}$ among the tested *s*-FETs.

Finally, we characterize the THz detection speed of the NW-FETs by recording the time trace of the photovoltage with a fast oscilloscope. For this measurement, we use a THz pulse duration of 1.6μs and we connect the detector output (D electrode) to a high-bandwidth (200 MHz) voltage preamplifier (Femto, HVA-200M-40-F) before the oscilloscope. The recorded waveform is depicted in figure 4.15b. The waveform discharge ramp is then fitted with the equation [78]

$V_{out}=P_1+V_{peak}\times\exp(-(t-P_2)/\tau)$, where V_{out} is the voltage read by the oscilloscope, t is the time independent variable, P_1, V_{peak} and P_2 are fitting parameters and τ is the detector response time. In the whole batch of samples we extract $\tau \sim 1\mu s$.

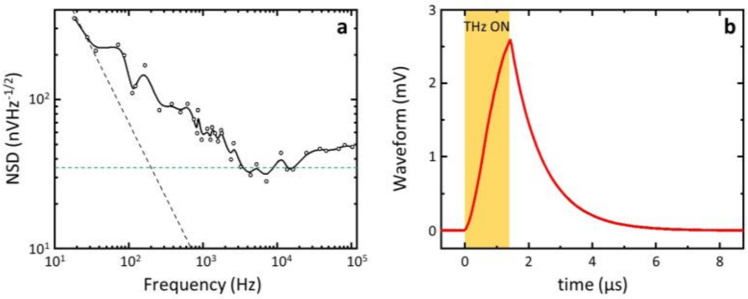

Figure 4.15: a) NSD measured with a lock-in oscillator frequency sweep technique. The dashed black line represents the 1/*f* (or flicker noise) term, and the dashed green line represents the thermal noise floor. b) Detection signal recorder with an *a*-FET at V_G = 12V, with a 5.0 GS/s oscilloscope, showing a response time of $\tau \sim 1\mu s$. The QCL pulse duration is set to 1.6μs, corresponding to the yellow-shaded area.

4.4. Discussion

Semiconductor NW FETs represent a promising platform for the development of RT THz frequency light detectors, thanks to the strong nonlinearity of the transfer characteristics and the remarkable combination of low *NEP* (< 1nW/Hz$^{1/2}$) and high responsivities (> 100V/W). However, conventional electrical and optical measurement techniques cannot unambiguously unveil the dominant detection mechanisms in InAs NW FETs, due to the inherent device asymmetry that allows different processes to be simultaneously activated.

Here, we investigate the photo-response of individual InAs nanowires via high spatial resolution (35 nm) THz photocurrent nanoscopy. Coupling a THz QCL to a s-SNOM and monitoring both electrical and optical readouts, provide us the information upon transport and scattering properties. As observed, the spatially resolved electric response shows the signatures of PTE or BE currents whose interplay is discussed as a function of photon density and material doping.

Having experienced by aforementioned technique, we then engineer our InAs NWs FETs operating as sensitive BE or PTE detector at 2.8 THz, at RT. We select and control the dominant detection dynamics via the symmetry of a lithographically patterned on-chip resonant antenna and through electrostatic gating, respectively. The devised detectors show state-of-the-art RT *NEP*s (0.67-2nWHz$^{-½}$) and response times of (1μs) suitable for real time sensing, security and imaging applications in the far-infrared, opening realistic perspectives for the development of nano-arrays potential for multi-pixel image reconstruction at high (> 2 THz) THz frequencies.

Chapter 5: Quantum dot based single electron transistors as cryogenic THz detectors

5.1. Quantum dot device versatile for quantum technologies

Applications in quantum information technology usually require a tight control of the orbitals states of a single electron, needed to encode and transfer information with high fidelity [221]. This has recently stimulated a wide interest in efficient, low-noise receivers that can detect a controlled photons number (photon counters), or even single-photons [222] - the ultimate limit of detection sensitivity - in quantum nanostructures. This has long been inaccessible for THz or gigahertz waves (wavelengths in the range 60 μm-1mm) because of the small energy quanta, as small as a part per one thousand of the photon energies in the visible or near-infrared regions. However, the far-infrared region of the electromagnetic spectrum discloses a peculiar potential in this respect: it is a rich domain of spectroscopy and metrological research, and a frontier region for a variety of applications in biomedical diagnostics [223], quality and process controls [224], security [225], high data rate wireless communication [226] as well as for applications in optical quantum cryptography [227], and for quantum key distribution [228].

Quantum detectors, conventionally employed in the visible, near-infrared or mid-infrared regimes - including photodiodes [229], photoconductors [230], phototransistors [231], charge-coupled detectors (CCDs) [232], photomultiplier tubes [233] or semiconductor quantum-well infrared photodetectors (QWIPs) [234] are devices that convert incoming photons directly into an electrical signal, as opposed to thermal detectors that rely on the conversion of incoming radiation to heat [235]. QWIPs represent the benchmark technology for quantum applications in the mid-infrared frequency range [236], owing to the high sensitivity and ultrafast response times, and the short lifetime of the intersubband transitions (τ_{IST} ~ ps) [235]. Pushing the operation of QWIPs in the far-infrared is however extremely challenging due to the low energy of far-infrared photons. Only few reports at high THz frequencies (4.5-7 THz) are presently available either in a standard mesa configuration, normally substrate-coupled through a polished facet [236], or in a double metal patch-antenna array architecture [237], or in a metamaterial configuration with dimensions below the diffraction limit [238], at 3 THz, and with a maximum speed of 3 GHz in an array configuration [239].

Quantum dots infrared photodetectors (QDIPs) represent a promising route to overcome some of the major limitations of THz QWIPs [240]. In particular, the energy level configuration and the orbital occupation can be controlled via the QD diameter-height and the gate bias, respectively. QDs are also inherently sensitive to normal incidence photoexcitation, therefore do not require 45° polished facets, metal-gratings [241], engineered band mixing [241,242] or reflectors, as it is conventionally needed for QWIPs [242]. Owing to the discrete density of states, they are well suited for tunable narrow band detection. Most importantly, the three-dimensional confinement leads to phonon bottleneck effect [243], inhibiting phonon scattering in QDs as compared to QWs [242,244] and increasing the lifetime of photoexcited carriers (~ 5-10 ps) [242], whose phonon-mediated relaxation to the ground state is eventually hindered in favor of an enhanced probability of tunneling out of the dot. This effect is then expected to give rise to a more efficient detection, as a consequence of a larger quantum efficiency and to enable operation at higher temperatures (up to 50-60 K) [240,242]. The reduced dependence of the density of states on temperature and the longer carrier lifetime (one to two order of magnitude) in QD have the additional advantage of reducing the dark current with respect to QWIPs [245] (figure 5.1).

QDIPs are promising candidates for applications in THz communication [235,246,247]. Once implemented in a single electron transistor (SET) geometry, a low noise equivalent power (*NEP*) $\sim 10^{-19}$WHz$^{-1/2}$ [235,247] can be indeed engineered under a precise control of bias [235]. When illuminated with a radiation energy that is not in resonance with the QD intersubband transition, QD-based devices still exhibit good detection performances (e.g. responsivity up to 100 A/W [248]), owing to the inherently strong non-linearity of the current-voltage characteristics.

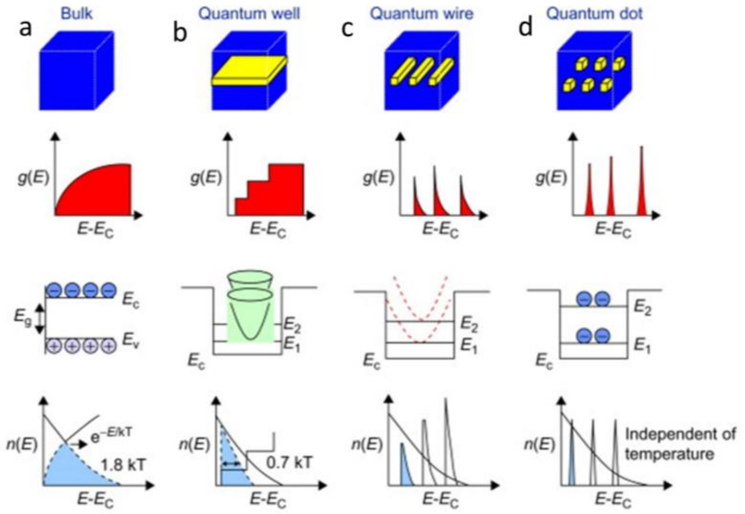

Figure 5.1: Schematics, density of states, and the carrier distribution for (a) bulk, (b) quantum wells, (c) quantum wires, and (d) quantum dots. Note that the quantum dot density of states is independent of temperature. Because the carrier distribution in quantum dots is discrete in energy, thermal transitions between the states require absorption of one or multiple phonons of the energy equal to the energy spacing, unlike the continuous distribution in the case of quantum well. This leads to lower dark current in QDIPs [241].

In this chapter, I report on the development of quantum-dot millimeter-wave nanodetectors employing InAs/InAsP QD nanowires (NWs) that, thanks to the small effective mass and favorable Fermi level pinning [167,249], give rise to localized QDs characterized by large charging energy [249,250]. Employing the confinement defined by the double-barrier heterostructure, we engineer a QD SET that, once irradiated with light, exhibits an extra electromotive force driven by the photothermoelectric (PTE) effect, which can be exploited to efficiently sense the incoming radiation with *NEP* levels down to 8 pWHz$^{-1/2}$. Importantly, the demonstrated PTE quantum detectors operate under zero-bias, therefore the dark current is largely reduced with respect to standard configurations employing biased systems [236–238]. The results and the physical analysis will be further discussed in the following sections of the present chapter.

In the last years, heterostructured semiconductor NWs proved to be a promising technological platform [1] for devising sensitive, high-speed, low-noise detectors across the THz [172]. Even though the stoichiometric and geometric control in the growth of axially heterostructured NWs can allow tailoring tunnel barrier properties on purpose, it does not allow a widely tunable tunnel coupling, as compared to electrostatically defined structures [251]. This provide an important benefit for efficient thermoelectric conversion [249,252], or for single-photon QD detectors which may require a broad different range of tunneling rates [253]. An alternative, more efficient strategy to simultaneously optimize charge stability and tunneling relies on engineering and tuning electrostatically the orbital configuration within the QD [254].

Therefore, in the following I will describe the transport characteristics and subsequently the orbital configuration as well as energy level spacing in InAsP/ InAs/ InAsP quantum dot component to pave the way of a proper understanding and eventually analysis for optically driven phenomena in our experiment.

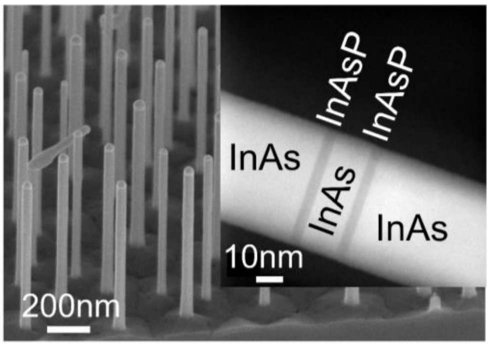

Figure 5.2: SEM image of a forest of epitaxially grown InAs nanowires, (inset). Transmission electron microscopy (TEM) image of a single InAs/InAsP QD-NW.

5.1.1. Coulomb blockade and transport in few electrons systems

The extremely reduced dimensions of nanometric systems determine a strong Coulomb interaction among the electrons in the nanostructrure. Therefore, the energy contribution due to the electrostatic charging of the quantum dot becomes relevant and can be experimentally investigated in the so-called "Coulomb blockade" phenomenon. In the typical electronic transport experiment in a quantum dot SET, two metallic contacts are employed as source and drain terminals, while one or more field effect electrodes are used as gates.

In order to explain the results of a typical low temperature transport measurement, both the energy quantization and the charging of the quantum dot, due to the interaction among the electrons, must be taken into account. In the following argument, I will neglect the former term and focus on the latter one. In the case of n gate electrodes, the charge induced of $\tilde{Q}_0$ on the system by the presence of the electrostatic voltages V_j applied to the j-th electrode is given by:

$$\tilde{Q}_0 = \sum_{j=0}^{n} C_{0j} V_j \tag{5.1}$$

where the $j = 0$ term refers to the quantum dot itself, so that $C_{00} = C_\Sigma$ is the autocapacitance of the system. The source and drain contacts are labelled by $j = 1$ and $j = 2$. The capacitive couplings between each electrode and the quantum dot are described by the parameters C_{0j}; in particular, $C_{0j}= C_j$. Therefore, C_j is the electrostatic capacitance between the quantum dot and the j-th electrode. The explicit relation between the charge induced in the system by the gate voltages and the total number N of the electrons in the quantum dot is:

$$\tilde{Q}_0 = Q_0 - q_0 = -eN - q_0 \tag{5.2}$$

where $Q_0 = -eN$ is the charge of the system due to the presence of N electrons and q_0 is the residual charge when all the gate voltages Vj are equal to 0. Regarding Eq. 5.1, Q_0 becomes:

$$Q_0 = q_0 + C_\Sigma V_0 + \sum_{j=1}^{n} C_{0j} V_j \tag{5.3}$$

Thus, the potential of the quantum dot with an electrostatic charge Q_0 is:

$$V_0(Q_0) = \frac{Q_0}{C_\Sigma} - \frac{q_0}{C_\Sigma} - \sum_{j=1}^{n} \frac{C_{0j}}{C_\Sigma} V_j \tag{5.4}$$

and hence, the electrostatic energy of the quantum dot with N electrons is given by:

$$U(N) = \int_0^{-eN} V_0(Q_0)\, dQ_0 = \frac{e^2 N^2}{2C_\Sigma} + eN\left(\frac{q_0}{C_\Sigma} + \sum_{j=1}^{n} \frac{C_{0j}}{C_\Sigma} V_j \right) \tag{5.5}$$

Now, it is possible to determine the electrostatic contribution Π_N to the addition energy (i.e. the energy required to add the N-th electron) as below:

$$\Pi_N = U(N) - U(N-1) = \frac{e^2}{C_\Sigma}(N - \frac{1}{2}) + e\left(\frac{q_0}{C_\Sigma} + \sum_{j=1}^{n} \frac{C_{0j}}{C_\Sigma} V_j\right) \tag{5.6}$$

Considering the quantization of orbital energy levels ε_i, in the approximation of “constant interaction” [255], and neglecting the spin degeneracy, the total energy of the quantum dot can be written as:

$$E(N) = \sum_{i=1}^{N} \varepsilon_i + U(N) \tag{5.7}$$

Consequently, the total addition energy for the N-th electron of a quantum containing N - 1 electrons is given by:

$$\mu_N = E(N) - E(N-1) = \varepsilon_N + \frac{e^2}{C_\Sigma}(N - \frac{1}{2}) + e\left(\frac{q_0}{C_\Sigma} + \sum_{j=1}^{n} \frac{C_{0j}}{C_\Sigma} V_j\right) \tag{5.8}$$

At low temperatures ($k_B T \ll e^2/C_\Sigma$) and adequately small source to drain voltage ($V_{sd} \ll e^2/C_\Sigma$, $V_s \sim V_d \sim 0$), the electrons can tunnel through the two barriers when the energy μ_N is equal to the chemical potentials μ_0 of the contacts ($\mu_s \sim \mu_d \sim \mu_0$), as shown in figure 5.3.

This configuration can be achieved by modulating the V_g on the gate electrode (labelled by j=3), hence, Eq. 5.8 will yield to:

$$\mu_s \square \mu_d = \mu_0 = \varepsilon_N + \frac{e^2}{C_\Sigma}(N - \frac{1}{2}) + e\left(\frac{q_0}{C_\Sigma} + \frac{C_{03}}{C_\Sigma} + \sum_{j=4}^{n} \frac{C_{0j}}{C_\Sigma} V_j\right) \tag{5.9}$$

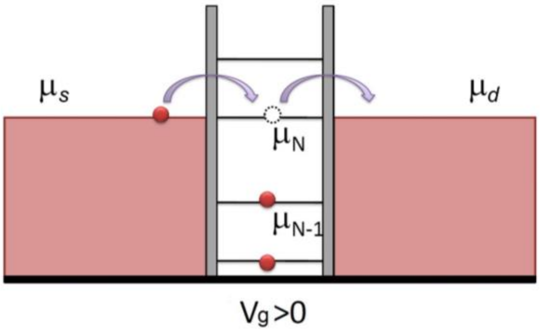

Figure 5.3: Electronic transport in a quantum dot through the tunnelling effect. The control of the gate voltage V_g allows to align the energy level μ_N of the quantum dot with the electrochemical potentials of the source (μ_s) and drain (μ_d) contacts [255].

Therefore, while varying the control voltage V_g, a set of conduction peaks is observed, owing to the progressive alignment of the quantum dot energy levels with the electrochemical potential of the source and drain contacts. The parameter $\alpha_j = -C_{0j} / C_\Sigma$, called "lever arm", is directly related to the capacitive coupling of the quantum dot with the j-th electrode. The N-th conductive peak is achieved when the value of V_g is:

$$V_g^N = \frac{1}{e\alpha_g}\left[\varepsilon_N + \frac{e^2}{C_\Sigma}(N - \frac{1}{2}) + e\left(\frac{q_0}{C_\Sigma} - \sum_{j=4}^{n} \alpha_j V_j\right) - \mu_0\right] \tag{5.10}$$

Thanks to the above-mentioned equation, the gate voltage difference between consecutive peaks can be defined as below:

$$V_g^N - V_g^{N-1} = \frac{1}{e\alpha_g}\left[\varepsilon_N - \varepsilon_{N-1} + \frac{e^2}{C_\Sigma}\right] \tag{5.11}$$

In case of finite values of source to drain bias ($V_{sd} \neq 0$), it is still possible to determine the conduction properties of the quantum dot, and the stability conditions for the electrons number. If the two barriers are supposed to be identical, the potential drop with respect to the quantum dot potential is equally distributed between the two contacts as follows:

$$\mu_s = \mu_0 + e\frac{V_{sd}}{2} \quad , \quad \mu_d = \mu_0 - e\frac{V_{sd}}{2} \tag{5.12}$$

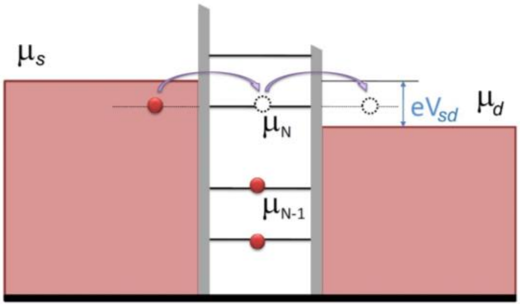

Figure 5.4: Electronic transport in a quantum dot, with finite source-to-drain bias. The tunnelling condition is possible only if there is an available energy level in the quantum dot between the electrochemical potentials of the two contacts [255].

Thus, at low temperature, tunnelling conduction is possible whenever there is an available electronic state in the quantum dot, having an addition energy value which lies between the electrochemical potentials of the two contacts, as shown in figure 5.4. When this condition is not satisfied, electron tunnelling is interdicted (“blocked”) and the system keeps a well-defined electron’s number *N*.

Moreover, the simultaneous variation of source to drain as well as gate voltage will give rise to the continuous changes in the conduction status of the system owing to the possibility of tunnelling /blockade of the electrons. In fact, the delimited diamond-shaped regions (figure 5.5) are called “Coulomb blockade diamonds” and are characterized by a fixed number of electrons in the quantum dot and a vanishing conductance. The low temperature transport measurement allows to determine the main physical parameter of the system, such as the auto-capacitance C_Σ of the quantum dot, lever arm α_g, the related charging energy (e^2 / C_Σ) and the energy deference between the consecutive single-particle orbital states ($\varepsilon_N - \varepsilon_{N\text{-}1}$).

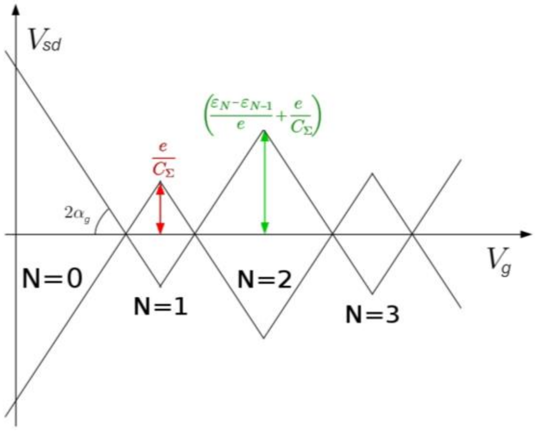

Figure 5.5: Coulomb blockade diamonds arise from the electrons number stability conditions in the $V_{sd} \times V_g$ plane. From the geometry of the scheme, it is possible to determine the main physical parameters of the quantum dot-based device [255].

5.1.2. Quantum devices and photodetection in THz regime

So far, several studies have been carried out to disclose the dominant physical dynamics for THz photodetection in quantum detectors (at low temperature). For instance, Riccardi. *et al.* have recently shown that the graphene quantum dot photodetector in THz regime relies on interfacial photogating effect [256]. Rinzan. *et al.* have reported on a photo-assisted single electron tunnelling (PASET) in carbon nanotube quantum dot in THz frequencies [257]. Moreover, a two-photon detection based on intersubband transitions in GaAs/AlGaAs QWs operating in the THz regime has been observed by H. Schneider. *et al.* [258]. However, here we propose a PTE model for THz detection in InAs/InAsP quantum dot SET [220,259], which can be operated in zero bias regime and thus bring the dark current to zero. The model and experiment will be defined in the following.

5.1.3. PTE model in a quantum dot SET

As discussed earlier, the SET is treated as a two terminals QD in contact with two particle reservoirs on its left (S) and right (D) sides, described by temperatures and chemical potentials T_s, μ_s and T_d, μ_d, respectively. Charge and heat transport through the system can be described with a transmission function governed by the general expressions provided by the non-equilibrium Keldysh formalism [260]. Many-body effects (such as electron-electron, electron-phonon and phonon-phonon interactions) are neglected, thus recovering the Landauer approach [261]. The general expressions for the thermoelectric transport through the dot - charge current (I_e), left and right heat (thermal) currents I_{Qs} and I_{Qd} - in stationary conditions are given by [261–264]:

$$I_e = I_{es} = I_{ed} = \frac{-e}{h}\int_{-\infty}^{+\infty} dE\, \theta(E)\, [f_s(E) - f_d(E)] \tag{5.13}$$

$$I_{Qs} = \frac{1}{h}\int_{-\infty}^{+\infty} dE\, (E - \mu_s)\, \theta(E)\, [f_s(E) - f_d(E)] \tag{5.14}$$

$$I_{Qd} = \frac{1}{h}\int_{-\infty}^{+\infty} dE\, (E - \mu_d)\, \theta(E)\, [f_s(E) - f_d(E)] \tag{5.15}$$

where the subscripts s and d denote the two reservoirs, f is the Fermi function, $e = |e|$ is the absolute value of the elementary charge, h is the Planck constant and $\theta(E)$ is the transmission function. Without loss of generality, we consider the left reservoir hotter than the right one ($T_s \geq T_d$), whereas no *a priori* assumption is done on the relative position of the two chemical potentials μ_s and μ_d. We assume valid the linear response approximation [263,264]. As given by Eq. 5.13, transport in a nanoscale system of non-interacting electrons is essentially controlled by the transmission function $\theta(E)$. For sufficiently spaced energy levels in a QD coupled to electrodes, a Breit-Wigner (Lorentzian)-like transmission function occurs whenever the electron energy E approaches one of the resonance energies (μ_N) of the QD [264–266]. $\theta(E)$ can then be written as:

$$\theta(E) = \sum_N \frac{\Gamma_N^2}{(E - \varepsilon_N)^2 + \Gamma_N^2} \tag{5.16}$$

The Lorentzian lineshapes are centered at each resonance ε_N, whose level is controlled in the experiment by V_g. In general, each resonance is characterized by a different finite broadening Γ_N. Once the transmission function $\theta(E)$ is known, we can access the kinetic transport coefficients (e.g. the Seebeck coefficient) that control, in the linear approximation, the thermoelectric properties of the

SET. The positions and broadenings of the resonances (ε_N, Γ_N) can be extracted from the transport map (Coulomb diamond map), assuming the temperature of the dot (T_{QD}) to be equal to the heat sink temperature T_0 = 4 K. By using Eqs. 5.13 and 5.14, we can then calculate the map of $|I_{sd}|$ in the dark state numerically.

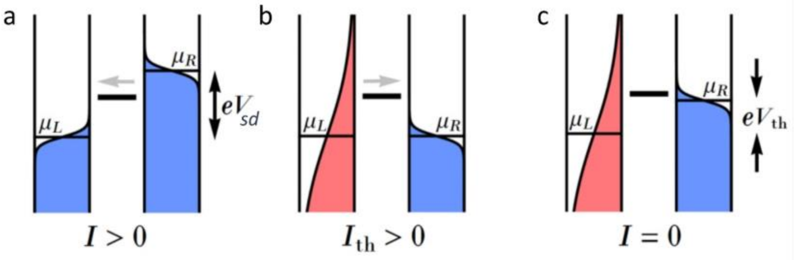

Figure 5.6: Illustrations of a resonance energy of a QD (black line) with respect to electrochemical potentials μ_L (μ_s) and μ_R (μ_d) of the reservoirs. Vertical axes represent electron energy. Colored areas represent Femi-Dirac distributions of electrons in reservoirs: blue indicates the temperature T, red indicates the higher temperature $T + \Delta T$. Gray arrows on top of resonances indicate electron current direction. Three cases: a) electrical bias giving rise to current $I = I_e$, b) thermal bias giving rise to thermocurrent $I_{th} = I_{Qs}$ (here shown at short-circuit condition), and c) thermal bias giving rise to thermovoltage V_{th} [267].

The proposed charge and heat transport model through the QD relies on the linear response approximation as mentioned above, which assumes that the device operates in a small interval of $\Delta\mu = \mu_s\text{-}\mu_d = -eV_{sd}$ and $\Delta T = T_s\text{-}T_d$, thus we consider both $\Delta\mu$ and ΔT as infinitesimal quantities (figure 5.6). We note that, when the THz beam is illuminating the system, the estimated value of ΔT is such that $\Delta T \ll T_{QD}$. This, however, does not qualitatively affect our results as long as ΔT does not larger than T_{QD} [266]. In the linear response approximation, we can write [265]:

$$f_s(E) - f_d(E) = \left(\frac{\partial f_s}{\partial E}\right)\left[\Delta\mu + (E - \mu_s)\frac{\Delta T}{T_s}\right] \tag{5.17}$$

Thus, the transport Eqs. 5.13 and 5.14 for charge and heat currents become:

$$I_e = \frac{-e}{h}\int_{-\infty}^{+\infty} dE\; \theta(E)\left(\frac{\partial f_s}{\partial E}\right)\left[-eV_{sd} + (E - \mu_s)\frac{\Delta T}{T_s}\right] \tag{5.18}$$

$$I_{Qs} = \frac{1}{h}\int_{-\infty}^{+\infty} dE\; (E - \mu_s)\,\theta(E)\left(\frac{\partial f_L}{\partial E}\right)\left[-eV_{sd} + (E - \mu_s)\frac{\Delta T}{T_s}\right] \tag{5.19}$$

We note that, in the linear response regime, the electric current for a Lorentzian transmission function can be expressed through an analytical formula [265].

Eventually, using Eqs. 5.18 and 5.19 it is possible to extract the transport coefficient of interest from the measurements, such as the isothermal conductance σ_0 and the contribution to the current due to the temperature bias, *i.e.* the Seebeck coefficient S_b, which become more evident when the electric current is written in a more effective form as below:

$$I_e = \sigma_0 \left(V_{sd} + S_b \Delta T \right) \tag{5.20}$$

Later in the current chapter (the section of optical characterization), we will discuss the implementation of aforementioned model for the analysis of PTE dynamics in our QD SET photodetector.

5.2. Device fabrication

We exploit InAs/$InAs_{0.3}P_{0.7}$ QD-NWs grown via a gold assisted CBE. This material system allows combining semiconductors with different lattice parameters in axial heterostructures, thanks to the efficient strain relaxation along the NW sidewalls. Moreover, the InAs/InP system is particularly suitable for the realization of high-quality axial NW heterostructures like QDs and superlattices in Au-assisted growth. Indeed, the very low solubility of both As and P into Au allows to obtain atomically sharp interfaces in both growth directions [268]. However, in the case of NWs grown from a metal seed nanoparticle (NP) by the VLS mechanism, the chemical composition of the NP changes when the growth is switched from one material to the other and this strongly affects the NP stability, the growth mode (straight or kinked) and the growth rate [268,269]. In particular, the growth of alternating InAs/InP segments is prone to nucleation delay during the growth of the InP segment, that can lead to NP reconfiguration, which, in turn, affects the growth dynamics [269]. On the other hand, if $InAs_{(1-x)}P_x$ alloys instead of InP are grown on top of InAs NWs, the nucleation delay is not present. As a consequence, the growth of InAs/$InAs_{(1-x)}P_x$ (figure 5.2) heterostructures is uniform and very symmetric thicknesses are obtained for the same growth times. Finally, the height of the tunneling barriers can be tuned by changing the P/As ratio in the alloy segments [270].

A 18 nm long segment of InAs with band gap $E_g = 0.356$ eV and electron effective mass $m^* = 0.063m_e$ [271], where m_e is the free electron mass, is confined by thin (5 ± 2 nm) $InAs_{0.3}P_{0.7}$ barriers with relatively high $E_g = 1.03$ eV and $m^* = 0.067m_e$ [272], leading to quantum confinement along the NW axial direction. The resulting InAs/$InAs_{0.3}P_{0.7}$ QD-NWs are transferred from the growth substrate over a 300 nm/350 μm SiO_2/intrinsic silicon wafer, where the detectors are nano-fabricated. Individual NWs are integrated in planar laterally-gated FETs [273] (figure 5.7), employing a combination of electron beam lithography (EBL) and thermal evaporation.

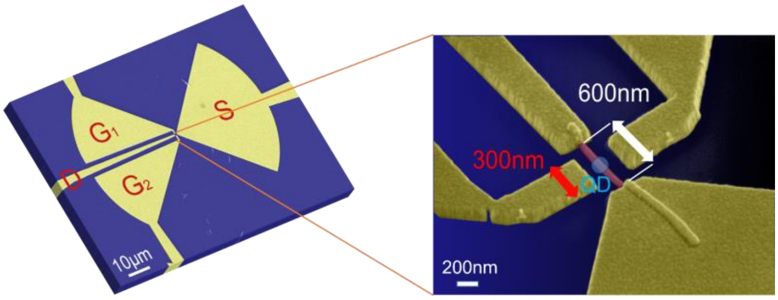

Figure 5.7: a) SEM image of a planar on-chip split bow-tie antenna. One side of the antenna is connected to the source electrode while the opposite side is connected to the arms of double lateral gate contacts. b) SEM image of a prototypical QD-NW SET.

5.3. Electromagnetic Simulation of the antenna

To couple the QD-NW based SET to the 0.6 THz field, the deeply sub-wavelength quantum dot element is asymmetrically integrated in a planar bow-tie antenna with radius 210 μm (figure 5.7). The asymmetry is ensured by the connection of the antenna arms to the S and lateral G electrodes. In order to evaluate the energy enhancement (η) owing to the presence of a planar bow-tie antenna, we perform 3D electromagnetic simulations of the detector's geometry utilizing commercial software (COMSOL Multiphysics). The simulated architecture comprises a metallic bow-tie antenna having radius of 210 μm and the device is illuminated with a 0.6 THz radiation, polarized parallel to the antenna major axis (figure 5.8). The energy is calculated as an integral in a small volume (600×400×350 nm) around the InAs nanowire. The enhancement is then computed as the ratio between the case of a gold antenna and the case of an antenna made of air, obtaining η>5000. The colormap in figure 5.8 represents the spatial distribution of the electromagnetic energy density on the plane of the antenna, normalized to the case where the antenna is not present.

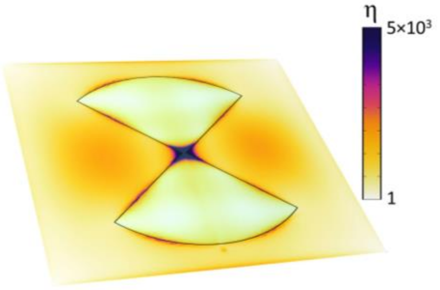

Figure 5.8: Electromagnetic simulation of the bow-tie antenna. The colormap shows the energy density on the detector plane, normalized to the energy density value obtained when the antenna is not present, i.e. the energy enhancement.

5.4. Geometrical dependence of orbital configuration and energy discretization in InAs/InAsP quantum dots

Thanks to the strong 3D confinement in QDs, by properly choosing the geometrical parameters of the dot, i.e. NW radius (R_{nw}) and width of the InAs segment between the two $InAs_{0.3}P_{0.7}$ barriers (W_{qd}), the distance between consecutive energy levels can be tailored to be resonant with a desired photon energy. We therefore compute the eigenstates $|\varphi_{nlg}>$ and eigenenergies φ_{nlg} of axially grown QD by iteratively solving the coupled Schrödinger-Poisson equations to investigate the energy spacing in our QDs component; here the quantum numbers n, l and g distinguish between levels confined along the radial, angular, and growth directions, respectively. The QD model is geometrically sketched in figure 5.9a and the simulation results are shown in figures 5.9b-5.9d. The computed energy spacing between the ground level and the first excited state, is ~ 9 meV for our specific QD geometry.

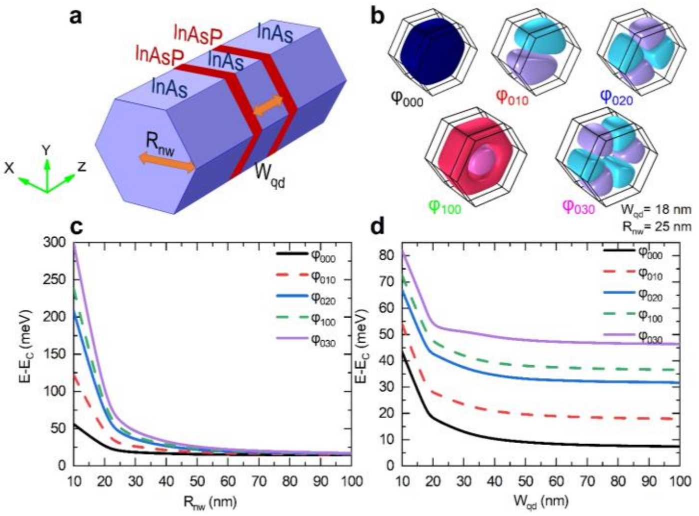

Figure 5.9: a) Three-dimensional hexagonal wurtzite structure of the axially grown QD-NW, employed in our numerical simulations. b) Distribution of the electron wave function (orbital configuration) for the first five energy states of a QD, having the following dimensions: NW radius (R_{nw}= 25 nm) and QD width along the growth direction (W_{qd}= 18 nm). c),d) Energy of the electronic states localized in the quantum dot, plotted as a function of R_{nw} and W_{qd} of the QD, respectively. Color lines (marked with letters, corresponding to panel b) present the evolution of the orbital energies. The ground state (black line) energy is E_{000} > 55 meV when R_{nw} approaches 10 nm, and it decreases noticeably while increasing the radius up to 50 nm (E_{000} < 20meV). As expected, the confinement also depends on W_{qd}. The energies of the radially confined states (quantum number g=0, (b)) as a function of W_{qd}. Interestingly, while the energy spacing between g=0 levels steadily decreases with R_{nw} (c), it remains almost unaltered when W_{qd} increases from 40 nm to 100 nm (d), demonstrating the strong correlation of quantum confinement to the geometrical characteristics.

Furthermore, we evaluate the lateral gates to QD capacitance (C_{gd}), as a function of QD size variation both radially and axially through the COMSOL Multiphysics simulation (figure 5.10). C_{Σ} and C_{gd} determine the gate lever arm, $\alpha_G = C_{gd}/C_{\Sigma}$, which is explicitly related to the capacitive coupling with the gate electrodes. The extrapolated C_{gd} value is equal to 1.1aF.

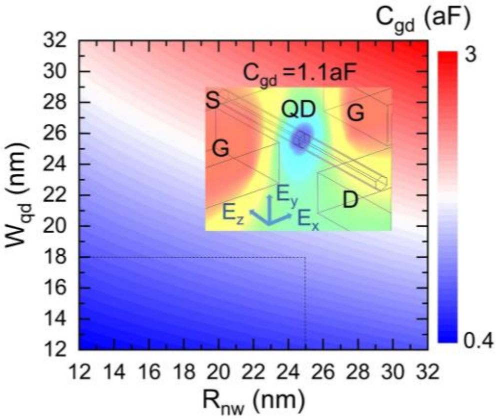

Figure 5.10: Color map of the gate-QD capacitance (C_{gd}) as a function of QD axial dimension (distance between the barriers, W_{qd}) and NW radius (R_{nw}), calculated numerically using an electrostatic simulation of the QD-NWFET performed with a commercial software (COMSOL Multiphysics). Inset: three-dimensional image of the SET channel overlaid to the simulated distribution of electrostatic potential around the InAs QD. The simulated C_{gd} value is 1.1aF for our specific device geometry (W_{qd} = 18nm, R_{nw} = 25nm).

5.5. Electrical characterization

We investigate the electron transport through the SET by measuring the charge stability diagram at a heat sink temperature T_0 = 4.2 K. The detector in mounted in a pulse-tube optical cryostat with helium exchange gas (Janis Research) and the I_{SD} is recorded as a function of both the V_{SD} and the V_G. The Coulomb blockade diagram (figure 5.11a) shows diamonds corresponding to regions where the conductance is suppressed, since single-electron tunneling processes are not allowed and the electron occupation (N) in the quantum dot is fixed. By spanning V_G beyond the pinch-off voltage (V_G = 4.5V), if both the thermal energy (k_BT) and the source-drain biasing energy (eV_{SD}) are smaller than the charging energy of the QD ($k_BT \leq eV_{SD} \leq e^2 / C_{\Sigma}$), a set of conduction peaks are visible, due to the progressive alignment of electrochemical potential on the *S* and *D* sides with the QD energy levels. Between two consecutive peaks, resonant tunneling through the barriers is inhibited and the charge stability condition is satisfied. Importantly, the transport characteristics of the SET in the Coulomb blockade regime, being related to the single particle energy states and to their mutual interactions, allows describing the electronic features of the device as explained in section 5.1.1. In particular, employing the constant interaction model [274], we evaluate the capacitive coupling between the QD and the gate electrode (C_{gd}), the charging energy, and the energy levels spectrum. Following these arguments, we extract from figure 5.11a: $e^2/C_\Sigma = 6.9$ meV, an energy level spacing $\Delta E = 7.0$ meV (in reasonable agreement with the value obtained by our Schrödinger-Poisson model), $C_\Sigma = 55$ aF, $C_{gd} = 1.1$ aF and $\alpha_G = C_{gd} / C_\Sigma = 18.8$ mV/V.

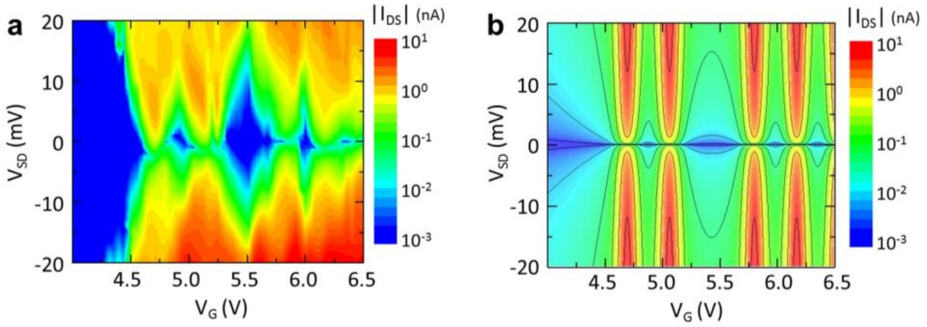

Figure 5.11: Low temperature electrical transport through the single electron transistor in the dark. The absolute drain-source current $|I_{DS}|$ is plotted as a function of V_{SD} (vertical axis) and V_G (horizontal axis) in logarithmic scale. a) Experimental dark state showing a typical Coulomb charge stability diagram, where the characteristic diamonds corresponding to a fixed electron population N=1,2,3 are resolved. b) Calculated THz-off map with the thermoelectric model, assuming the dot temperature T_{QD} equal to the heat-sink temperature $T_{QD}=T_0 = 4$ K.

5.6. Optical characterization

We shine the THz frequency light on the SET, by using a continuous-wave electronic source operating at 0.6 THz with an average power of 1mW (Virginia diodes) modulated via a mechanical chopper at 518 Hz. The THz beam is focused on the detector by a parabolic mirror placed in front of the cryostat window, reaching a spot size of radius ~1 mm. The *S* electrode of the QD-NW based FET is connected to a supplier (Keithley 2400), the *D* electrode to a transimpedance preamplifier, while the double lateral gates are identically biased. The retrieved photocurrent is monitored through a splitted channel via an Agilent multimeter and a lock-in-amplifier (Signal Recovery 7265 DSP). The former measures the direct current (*DC*) whereas the latter monitors the alternating current (*AC*) component given by the incoming electromagnetic wave.

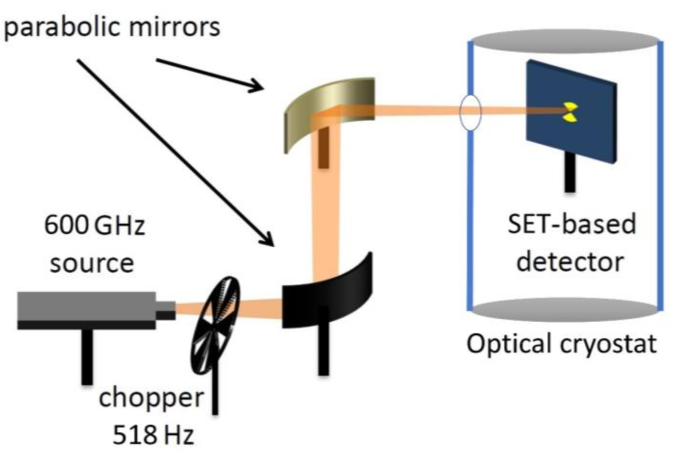

Figure 5.12: Optical setup scheme. The 600 GHz radiation from the source is mechanically chopped at 518 Hz, collimated and focused by means of parabolic mirrors onto the detector mounted in a pulse-tube optical cryostat (heat sink temperature T_0= 4.2K).

Once funneling the THz beam onto the detection element, the retrieved *dc* current map appears visibly altered (figure 5.13a). The clearest features are the distorted Coulomb diamonds and the shift of the current peaks towards larger V_G as compared to the corresponding peaks measured without THz radiation (figure 5.11a). In particular, the current vanishes to zero at different V_{SD} and for different V_G, very differently from what happens in the dark (figure 5.11a), where, for any given V_G, it approaches zero at V_{SD}= 0V.

We ascribe this behavior to the photothermoelectric effect, generated by the thermal gradient (ΔT) between the left and right side of the QD-NW: the bow-tie antenna funnels the radiation asymmetrically, producing a field enhancement, that is mainly confined between the *S* and *G* electrodes, leaving the drain-side colder with respect to the source-side of the QD.

Figure 5.13c schematically displays the detection mechanism, overlaid to the numerically simulated (finite element method, Comsol Multiphysics) electromagnetic energy enhancement (η) induced by the THz beam at the source-side of the NW. In this picture, the total current flowing along the SET channel $I_{\mathrm{DS}} = \sigma_0 \ (V_{SD} + S_b \Delta T)$ where $\sigma_0 = \mathrm{d}I_{\mathrm{SD}}/\mathrm{d}V_{\mathrm{SD}}$ is the electronic conductance, S_b represents the QD Seebeck coefficient (or thermopower). Under illumination, the distortion of the Coulomb diamonds is given by the additional electromotive force $V_{\mathrm{PTE}} = S_b \Delta T$, which is identified in the current map (figure 5.13a) by the V_{SD} values at which the current vanishes along the gate voltage sweep (it takes a finite V_{SD} to counterbalance V_{PTE}). Therefore, the amplitude and sign of V_{PTE} are ultimately determined by the QD thermopower S_b. It is worth noticing that, by taking advantage of the PTE mechanism, our scheme allows for zero-bias, zero-dark current operation, limiting the detector noise to intrinsic charge or temperature fluctuations.

Such a qualitative interpretation of the PTE detection is then supported by the quantitative comparison of the experimental data with the outcome of a numerical model of charge and heat transport through the QD, based on the Landauer approach [263,264], to evaluate its thermoelectric properties, starting from electrical parameters that mimic our experimental configuration. The results, shown in figure 5.13b, exhibit a good agreement with the experimental data (figure 5.13a). When the THz beam is illuminating the detector, we expect that a thermal gradient ΔT between the left (S) and right (D) leads of the QD is established, as a consequence of the asymmetric coupling provided by the bow-tie antenna (figure 5.13c). In addition to ΔT, the evaluation of the theoretical map for the illuminated case (figure 5.13b) also considers a global heating of the dot ($T_{QD} > T_0$, where T_{QD} is the dot temperature). This accounts for the fact that the QD, being approximately located at the center of the SET, will reach, at steady state, an intermediate temperature between those of the S and D extremes. By comparing the model with the experimental results, we estimate an overall increase of T_{QD} from 4 K (T_0) in the dark state to 7 K in the illuminated case, with a THz-induced temperature difference ΔT = 5 K between the leads. The increase of T_{QD} has the effect of increasing the coulomb peaks broadenings, whereas ΔT gives rise to a clear Seebeck effect, which corresponds to the additional electromotive force ($-S_\mathrm{b}\Delta T$) acting on the dot. Such a picture is nicely captured by the superposition of the $|I_{DS}|$ map in the illuminated case (THz on) with the theoretical contour lines corresponding to $I_{DS} = 0$ ($V_{SD} = -S_\mathrm{b}\Delta T$), calculated for different values of ΔT (figure 5.13d).

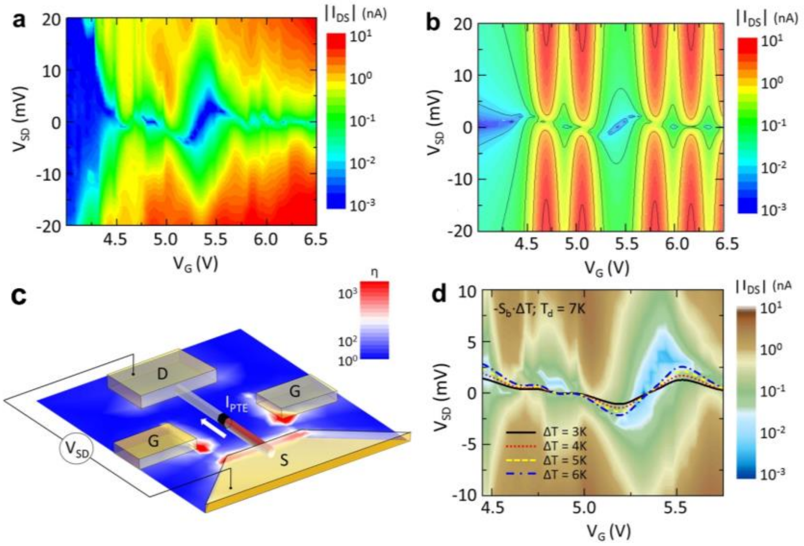

Figure 5.13: Low temperature electrical transport through the single electron transistor in the illuminated (a,b) states. a) $|I_{DS}|$ map measured when the 0.6 THz radiation is illuminating the device, showing smeared and tilted Coulomb diamonds. b) Calculated evolution of the Coulomb blockade diagram under illumination: a longitudinal source-drain thermal gradient ΔT = 5 K and a global heating of the dot T_{QD} = 7 K are assumed. c) Schematic diagram of the detection mechanism: the sign of the photothermoelectric (PTE) contribution to the current is determined by the direction of the thermal gradient and by the sign of the Seebeck coefficient of the QD. The background color map is a numerical simulation of the electromagnetic energy density enhancement (η) under THz illumination. d) Overlay between the experimental $|I_{DS}|$ color map and the PTE electromotive force $V_\mathrm{PTE} = -S_\mathrm{b}\Delta T$, calculated assuming different THz-induced ΔT= 3 K, 4 K, 5 K, 6 K and for T_{QD}=7 K.

5.7. Detector performance

We also extrapolate the gate bias dependent detector responsivity (R_a) in order to evaluate the main figures of merit of the devised QD NW photodetector. As shown in figure 5.14b, the observed dependence of R_a from V_G is correlated with the sharp transport peaks retrieved via transport experiments (figure 5.13a). In particular, the multiple sign changes of the photoresponse reflect the sign changes of the thermopower S_b around each Coulomb peak and R_a reaches a maximum value of 55 μA/W. The corresponding *NEP* [275] is determined by the ratio between the noise spectral density (NSD) and R_a. The NSD is measured by connecting *D* to a Dacron dynamic spectrum analyzer (model Photon) (figure 5.14a), while keeping *S* grounded and V_G=5V. At low frequency (f < 200 Hz) the noise spectrum is mostly following $1/f^b$ trend (0<b<2 pink noise), whereas at higher frequencies (f > 200 Hz) it is dominated by instrumental noise, slightly increasing as a function of frequency. Significantly, a local minimum in the noise figure occurs at 518 Hz, *i.e.* the frequency of the employed mechanical chopper. The contribution of the thermal (Johnson-Nyquist) noise in our system is $\sim 0.5 \times 10^{-15}$A/Hz$^{1/2}$ for V_G = 5V and V_{SD} = 0V. The bias dependent *NEP* (figure 5.14d) shows a sequence of minima corresponding to the peaks observed in the responsivity curve. A minimum *NEP* of 8 pWHz$^{-1/2}$ is reached (figure 5.14d). Although it appears still distant from the *NEP*s of commercially available cooled detectors as hot electron bolometers (*NEP*s~10^{-19}-10^{-20} WHz$^{-½}$) [235], the envisioned optimization guidelines combined with its zero-dark-current and inherent quantum nature make the proposed technology extremely appealing for quantum technology oriented applications.

We then estimate the temporal response of the proposed QD-NW PTE device through the analysis of its transport characteristics. As demonstrated experimentally, the timescales governing the heating/cooling dynamics of the carrier density in InAs NWs falls in the 40 fs - 4 ps range [276]. These timescales are much faster than the detector rise/fall times, which are limited by its electrical time constant $\tau_{RC} = R_t C_t$ ~ 1ns - 10 ns, where R_t (~1MΩ - 10MΩ) and C_t (~1 fF, includes the bow-tie shunt capacitance, simulated using COMSOL Multiphysics, electrostatic module) are the photodetector resistance and capacitance, respectively.

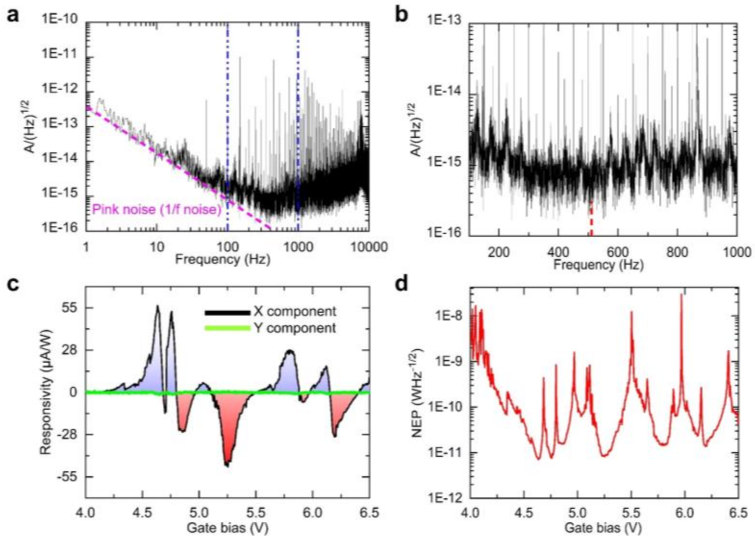

Figure 5.14: a) Noise Spectral Density (NSD) as a function of frequency measured by a spectrum analyzer. Pink dashed line is referring to the predicted 1/f noise contributor. The dotted blue lines mark the region of low noise. b) Zoom of the NSD of panel a) plotted in the 100 Hz-1 kHz range while the red dashed line refers to the frequency equal to 518 Hz; c) Responsivity measured under illumination at 0.6 THz, at low temperature (T_0 = 4.2 K), plotted as a function of V_G, while keeping V_{SD} fixed at zero and measuring the X and Y components of the lock in amplifier. d) Noise equivalent power (*NEP*) plotted as a function of V_G.

5.8. Quantum engineering roadmap

Starting from theoretical considerations based on the proposed photothermoelectric model, we can identify a qualitative and quantitative roadmap for device optimization. The PTE mechanism is described by the heat and charge transport through the dot, which, in turn, is governed by the energy-dependent transmission function $\theta(E)$. We can then engineer the system following the two strategies detailed below:

a. Optimization of the transmission through a single level.
b. Optimization through the selection of the QD energy levels spacing.

a. For sufficiently spaced energy levels in a QD coupled to electrodes, a Lorentzian-like transmission function occurs. For such transmission function, it is well known [263,264] that the Seebeck coefficient, i.e. the detector responsivity, can be improved by reducing the broadening parameter (Γ). At each resonance, Γ depends on the coupling between the QD and the electrodes (decreases for lower coupling [264], figure 5.16a), which is determined by various material and geometrical factors, e.g. barrier height and width, doping on the leads [264], and by the QD orbitals involved [249]. Interestingly, by using a multi-gate architecture, the barrier transparency can be tuned by the application of an electric field in the dot radial direction [249]. In principle, such a strategy could be adopted to maximize the photothermoelectric conversion in the device. However, the reduction in Γ comes at the cost of a reduced conductivity (reduced barrier transparency). Therefore, we expect to find a trade-off between a low-*NEP* and a low resistance, which ultimately sets the detector response time.

b. By considering the collective ensemble of the QD energy levels, the increase of the energy spacing improves the device sensitivity. In fact, a larger spacing between the individual resonances of θ(*E*) reduces the destructive interplay between adjacent single-level transmission functions, increasing the thermoelectric conversion (figure 5.16b). This is also reflected in the results depicted in figures 5.13d and 5.14c: the larger Coulomb diamond corresponds to the largest thermoelectric conversion, because of the increased energy spacing between the two resonances occurring at V_G = 5.2 V and V_G = 5.8 V. On the other hand, a smaller Seebeck coefficient is expected for the smaller diamonds. The latter arguments lead to the conclusion that a lower *NEP* is reached when the quantum confinement is increased, i.e. when the dot size is reduced. Therefore, in order to improve the detector sensitivity, the quantum design should go towards thinner NWs, or a reduced spacing between the barriers.

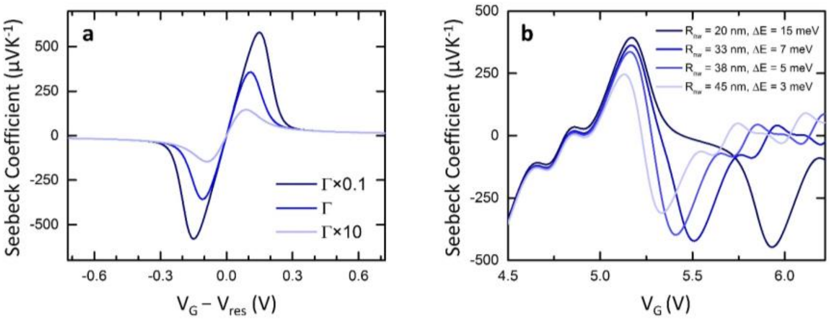

Figure 5.16: a) effect of the broadening parameter Γ on the Seebeck coefficient for an individual Lorentian resonance. Here, we assume Γ=0.24 me with the experimental parameter (lever are, QD temperature) reported earlier. b) Simulated Seebeck coefficient for different energy level spacing between the ground state and first excited state, assuming a charging energy, lever arm, temperature gradient and Γ= 0.24 meV, identical to those used for the calculations reported in figure 5.11. A large Δ*E* is beneficial to improve the maximum thermopower.

Therefore, the design of an ideal QD-based PTE device requires a critical understanding of the mechanism, together with an application-oriented optimization approach:

i) For high-sensitivity applications, thinner NWs (R_{nw} < 20 nm) with opaque barriers should be used, in view of maximizing the PTE conversion.

ii) For high-speed applications, the overall device resistance should be kept < 100 kΩ, thus involving thick NWs (R_{nw} > 35 nm) and transparent barriers.

5.9. Discussion

The achieved performances, combined with the extreme versatility of the QD-NW platform in terms of geometry and chemical composition, and with the intrinsically broadband and zero-bias nature of the PTE detection mechanism, unveiled through the choice of the impinging frequency - NW QD geometry combination, leave room for substantial improvements of the proposed quantum detection concept. For example, we envision that an optimization strategy for the PTE conversion shall proceed towards the reduction of the tunnel coupling between the dot and the leads [249], the engineering of the energy levels spacing and the exploitation of quantum phenomena, e.g. Kondo effect [277], in search of a balance between detector sensitivity and speed. Therefore, the reported results open a solid perspective for the combination of THz technology and few-electron physics to address some of the major challenges of quantum science, as quantum key distributions, quantum communications, and quantum sensing, where sub-shot noise *NEP*s combined with large quantum efficiencies are required. Furthermore, our work provides a clear understanding of the broadband PTE driven photoresponse in a QD-NW architecture, offering a framework for disentangling the different physical phenomena that would occur when the impinging photon energy matches the QD level spacing.

However, the flexibility offered by quantum engineering to optimize device transport and optical properties while simultaneously matching the photon energy with the QD energy level spacing, makes our QD InAs/InAsP heterostructured-nanowires an ideal building block in quantum-optics and nanophotonic applications, requiring a precise control of individual photon paths.

Chapter 6: Double photon detection scheme in quantum devices

Intersubband transitions in QWs have been exploited to engineer several key photonic and optoelectronic devices in the mid-IR, as QWIPs and QCL [258]. These innovations have formed the basis for emerging applications in thermal imaging, surveillance technology [278], chemical sensing [279], and infrared data transmission [258]. Moreover, intersubband transitions in QWs go along with pronounced optical nonlinearities, resulting in huge nonlinear coefficients for second harmonic generation, more than three orders of magnitude larger than for the host material GaAs [280]. Intersubband transitions have also been exploited for wavelength conversion of QCL radiation [281] and external near-infrared signals [282]. Quadratic photodetection involving resonant two-photon transitions between three energy levels, namely two bound states |1>, |2>, and one equidistant continuum resonance |3> is demonstrated in figure 6.1. In this configuration, two infrared photons are required to emit an electron into the continuum, such that the photocurrent scales quadratically with the incident power [283]. This behaviour, which contrasts the linear power dependence of standard QWIPs [258], provides the basis for device operation as a quadratic detector. Furthermore, the two-photon QWIP approach has proven useful for quadratic autocorrelation of pulsed mid-infrared sources including frequency converter radiation from tabletop laser systems [283], free-electron lasers [284], and QCLs. For the latter device, various modes of pulsed operation, including self-pulsations [285], coherent instabilities [286], and modelocking [287] have been demonstrated so far. Besides these applications in mid-infrared pulse diagnostics, the two-photon QWIPs also enabled several fundamental investigations of intersubband dynamics [283,288].

Extending device operation towards far-infrared wavelengths has led to the demonstration of THz-QCLs [15,289] and THz-QWIPs [236,290]. Nonlinear detection in this spectral regime in particular would be promising for applications in THz technology based on femtosecond near-infrared lasers [291] where short THz transients naturally emerge. Moreover, two-photon QWIPs operating in the THz regime have shown quadratic intensity dependence and been used in quadratic autocorrelation measurements of far-infrared picosecond pulses from a free-electron laser [258] with quadratic detection at THz pulse intensities as low as a few pJ due to a huge optical nonlinearity.

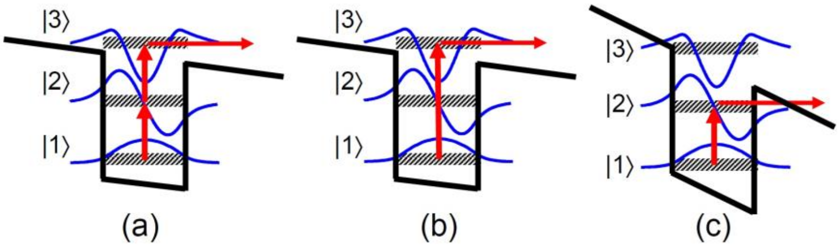

Figure 6.1: Band diagrams for (a) quadratic detection associated with transitions |1>→ |2> and |2> → |3>, (b) linear detection by transition |1> → |3>, and (c) linear detection involving |1> → |2> assisted by tunnelling [258].

Applications of QD structures for THz detection have been reported so far in different works [220,256,257]. Due to its unique structure and properties, a QD photodetector can absorb light incident from all directions without using grating couplers. The spectral response of a QD photodetector is usually very narrow due to the distribution of initial and final states [292]. If the transition energies of the QD levels are designed not to match the longitudinal optical (LO) phonon energies, the recombination process via LO phonons can be suppressed, which will result in a longer excited electron lifetime and a higher signal-to-noise ratio. These unique properties could overcome some of the shortcomings encountered in QWIPs [293].

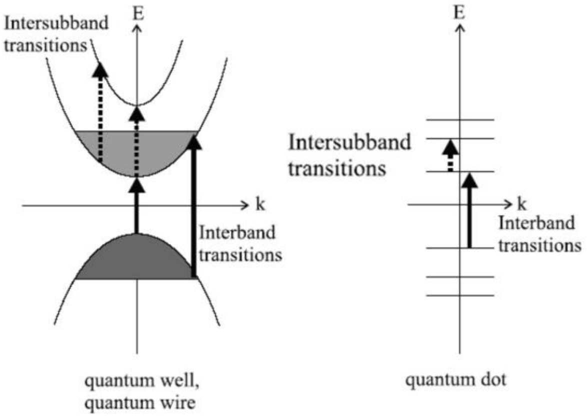

Figure 6.2: Interband and intersubband transitions for quantum wells, quantum wires (left) and quantum dots (right). The diagrams show a scheme of the band/level structure [294].

Thereby, we engineer a double photon THz detector exploiting a InAs nanowire QD SET. We employ a 2.8 THz frequency QCL, to unveil the dominant photodetection dynamics in such configuration which might be governed by intersubband transition in QD and hence, gives rise to the exploitation of double photon detection with a huge impact in non-linear optical applications. In order to do that, the same kind of QDs component as described in chapter 5 (section 5.1), embedded in a FET and characterized by a QCL, emitting at 2.8 THz frequency, are considered.

As QDs are deeply sub-wavelength objects in the THz region, in order to couple the free space-propagating wave (λ =107 μm) we employ an integrated symmetrical planner bow-tie antenna (figure 6.3). Moreover, we take into account that intersubband transitions are allowed only if the electric field of the electromagnetic wave is parallel to the direction of confinement.

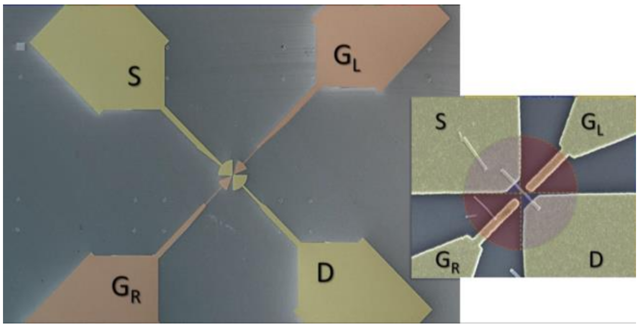

Figure 6.3: SEM image of a planar on-chip bow-tie antenna. One side of the antenna is connected to the source (S) electrode while the opposite side is connected to the drain (D) so that the direction of impinging electric filed can be parallel to the confinement axis. A couple of lateral gates consist of gate left (G_L) and gate right (G_R) are used for tuning of discrete energy levels in QD to be in resonance with the chemical potential of the leads (μ_S and μ_D). (Onset) SEM image of a prototypical QD-NW SET.

We then characterize our photodetector electrically as discussed in chapter 5 (section 5.4). From the transport measurement in the low temperature (4K) we extract the coulomb diamonds map and so the energy level spacing in the range of 5meV to 15meV is calculated (Eq. 5.11). Given the fact that the associated energy for 2.8THz frequency is around 10meV, we can expect that the impinging light can be in resonance with energy level spacing in QD, and thus, the transition in the intersubband of QD can be favorable.

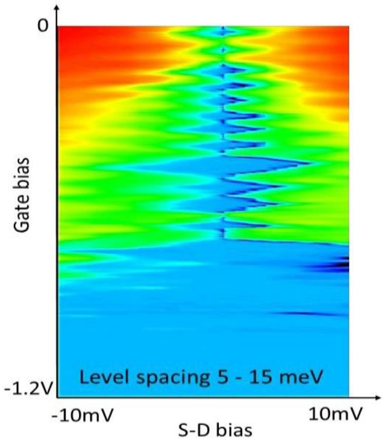

Figure 6.4: Low temperature electrical transport through the SET in the absence of light. The absolute source-drain current (I_{SD}) as a function of source-drain bias (S-D) and gate bias.

The optical measurement takes place when the QD SET is mounted in a helium flow Janis optical cryostat and illuminated by a 2.8 THz frequency QCL. The laser is operated in pulsed mode, and the beam is then focused into the detector through the several optical lenses as explained in chapter 3 (section 3.5.1). Under this condition, a maximum value of $R_v = 50$ V/W is obtained.

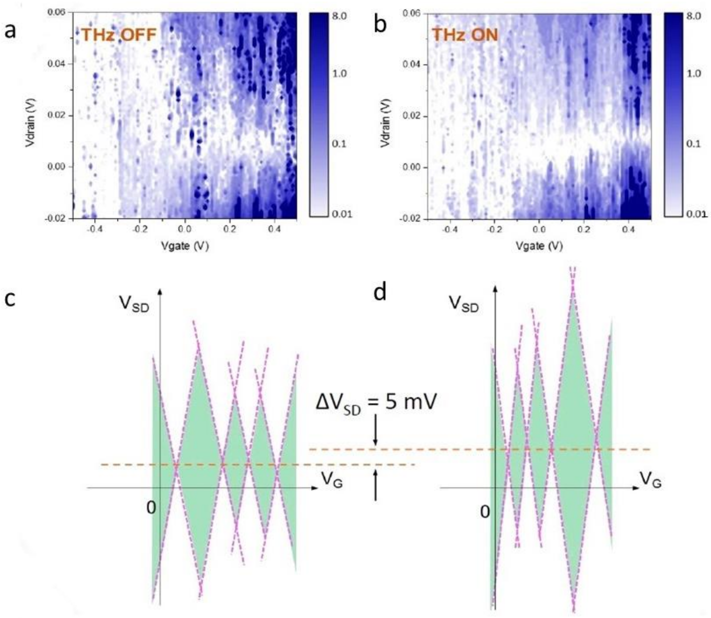

Figure 6.5: a,b) conductance maps collected experimentally through the transport measurements in the absence and presence of the THz light respectively and in 4K that show absolute source-drain current (I_{SD}) as a function of source-drain voltage (V_{drain}) and gate voltage (V_{gate}). c,d) Schematics of light off/ light on maps in correspondence with experimental maps which represent the consecutive diamonds by means of purple dashed lines. Horizontal red dashed lines pass from centre of diamonds demonstrating a vertical shift of around 5mV in the presence of the THz light due to the PTE. Moreover, a horizontal shift is observed that can be attributed to a possible intersubband transition.

Looking at the conductance maps both in presence and absence of the THz light (figure 6.5), and so by comparing light on/off maps with each other, we conclude that THz radiation has two major impacts on the conductance, which occurs through the QD in coulomb blockade regime:

- Firstly, a rigid and evident shift along vertical axis (V_{SD}) which is ascribed to the onset of an electromotive force owing to the PTE effect.
- Secondly, a difference in level energies (a shift along V_G) which is possibly due to the intersubband transitions.

There are still lots of rooms for the improvement as this is a broad topic and therefore the results discussed in this chapter are preliminary steps toward an appropriate understanding of know-how for the better optimization of parameters such as thermal isolation, noise reduction, etc. that can help to selectively activate double photon detection dynamics in the QD SET THz photodetectors which is of interest for non-linear optics and achieving higher harmonics. This is the perspective of this latter part of my experimental activity.

Conclusion and perspective

The THz region of the electromagnetic spectrum (1–10 THz frequencies, 300–30 μm) has historically suffered from the lack of photonic and optoelectronic devices, in large part because of inadequate optical materials with suitable reflectivity, absorption, or transmission in this spectral range. However, emerging applications such as quantum sensing, high data-rate communications, security, metrology, atmospheric sensing, biomedical imaging, processing and quality control, food inspection, and cultural heritage are increasing the demand for reliable, miniaturized, and cost-effective THz technologies, easy to be integrated with existing photonic or electronic platforms.

A widespread technological development, in this spectral range, entails the development of performing sources, modulators, and detectors. However, it is well known that, while the THz spectral region lies at the boundary between the mature and well-developed domains of infrared photonics and high-speed electronics, device concepts taken from the neighbouring fields cannot be adapted to THz frequencies. On one side, conventional electronic devices are too slow to allow switching, modulation, or actuation at THz frequencies. On the other side, traditional semiconductor materials ,a cornerstone of photonic devices, have a bandgap that far exceeds the THz photon energy, making them unsuitable for devising active optoelectronic components such as detectors, sources, and modulators.

Artificial semiconductor heterostructures played a major role in developing THz electronic and photonic technologies, providing a highly effective platform for the manipulation and control of carriers and photons, and overcoming the fundamental limitation represented by the valence to conduction bandgap. However, these solid-state architectures require challenging epitaxial growth procedures and, commonly, low operation temperature.

Layered 2D materials, such as graphene, black phosphorus, transition metal dichalcogenides (TMDs), and their related vdW heterostructures, as well as epitaxially grown 1D semiconductor NW have garnered increasing attention in the last few years owing to their unusual optical and electrical properties that can enable manipulation, propagation, and detection of THz waves with an unprecedented level of control.

Along with above mentioned considerations, the development of a breakthrough solid-state technology for fast, room-temperature, THz detectors integrated in high-speed multipixel arrays is highly desired. Therefore, the context of this thesis was fully dedicated to the investigation of physical dynamics of detection within the THz photodetector building blocks with different choices of material for optimizing their state-of-the-art and figures of merits to be eventually compatible with the technological platform.

In this regard, we first fabricated and characterized numerous THz SLG photodetectors, being proven to be versatile for up-scaling, with pulsed QCLs operating in the frequency range 2.8 THz. PTE-dominated detection was demonstrated in all the realized devices by measuring the device responsivity as a function of applied gate voltage. By characterizing more than 50 photodetectors, we obtained a minimum NEP ~1 $nWHz^{-1/2}$ and response times ~5 ns. According to the PTE model, the n_0 in SLG is the main electrical property that determines the amplitude of the Seebeck coefficient. In good agreement with this prediction, our statistical analysis indicated that detectors NEP decreases for lower n_0, confirming a PTE-driven detection.

Moreover, our analysis indicated that Al_2O_3/SLG/hBN heterostructures present a two times lower performance variability in the NEP figure of merit with respect to the other material platforms. This feature is one of the main requirements towards the realization of multi-pixel THz.

Later, we also captured snapshots of the photoresponse of individual InAs NWs via THz photocurrent nanoscopy, using a s- SNOM coupled to a THz QCL. By monitoring the electrical read-outs of the FET while scanning the sample, we mapped the photocurrent distribution induced by local THz photoexcitation with sub-diffraction spatial resolution (18nm). Lock-in detection at the n-th harmonics of the AFM tip tapping frequency, allowed isolating the near-field photocurrent I_n from the background due to farfield illumination. The spatially resolved electric response of InAs NWFET exhibited the fingerprints of PTE and bolometric currents, clearly distinguishable by their spatial profiles. While PTE response was characterized by a phase change along the NW, the bolometric currents was signaled constant polarity. By tuning the carrier density with the lateral gate, we revealed that the PTE effect dominates at high doping as expected due to the positive correlation of carrier density, temperature gradient and Seebeck coefficient. To elucidate the interplay of the two thermal effects we further investigated the dependence on photon density and on applied source-drain bias. Specifically, the lack of bias dependence indicated negligible contribution from plasma wave rectification, while the photovoltaic effect was discarded due to the sizable electronic gap of InAs NW (365meV) preventing electron-hole pair excitation by THz absorption. Taking advantage of aforementioned knowledge and study, we were then able to engineer InAs NW based FET integrated with different antenna's geometry for efficiently detecting THz light, by selectively tuning the dominant thermal photodetection dynamics (interplay of PTE effect and bolometric effect).

We finally employed QD NWs grown CBE, which provides a precise control over the NW stoichiometry and geometry so that a small segment of InAs (18nm) is confined by thin (7nm) $InAs_{0.3}P_{0.7}$ barriers, resulting in an axially confined QD. The QD NWs were then transferred over a 300 nm/350 μm SiO_2/intrinsic silicon wafer, and then embedded in SET, defining weakly coupled S and D electrodes, and capacitively coupled to a set of two lateral gate electrodes.

We then illuminated the QD device with a continuous-wave electronic source operating at 0.6 THz with an average power of 1mW. Under this condition, Coulomb diamonds were distorted, and the peaks were shifted as compared to where they take place in the absence of THz. These shifts stem from an additional THz-induced electromotive force whose amplitude changes with V_G. This feature can be well-described considering the SET as a thermoelectric device where the current transport is modified by a thermal gradient. We also calculated the figures of merit for such detector, and the observed THz responsivity was correlated with the sharp transport peaks retrieved via transport experiments. As expected, the responsivity trend revealed a visible PTE effect, following the QD related Seebeck coefficient fluctuations as a function of V_G. A maximum responsivity R_v = 55 μA/W was measured. Additionally, a minimum NEP = 5pWHz$^{-1/2}$ was obtained. Importantly, the PTE mechanism allowed for zero-bias, zero-dark-current operation of the QD NW device, promising for the development of a highly sensitive THz cryogenic detector platform based on axially heterostructured NW.

Future challenges regard the improvement of the architecture reliability and the possibility to exploit NW QD as double photon THz photodetectors to be exploited for second order non-linear autocorrelation experiments in the far infrared, where a reliable technological platform does not exist.

Heterostructured NWs in a hard-wall double-barrier configuration, in the channel of a double-later gate FET can induce quadratic photodetection via resonant two-photon transitions between three orbital energy levels (two confined states in the QD and one equidistant quasi-resonant state after the adjacent InP barrier) The role of the intermediate confined state is to induce a resonantly enhanced optical nonlinearity. The energy level configuration and the orbital occupation will be set through the growth calibration of the QD diameter/height and the gate bias, respectively. The source-drain conductance is expected to show sharp peaks as a function of the gate voltage, corresponding to the resonant elastic tunneling of electrons through the dot; Coulomb blockade occurs between the peaks and their gate voltage spacing is related to the energy level difference and to the charging energy of the dot, as we preliminary demonstrated in a proof of principle QD-NW FET.

The THz radiation, coupled in the system, will then provide to the electrons the required energy to fulfill the tunneling conditions, leading to additional satellite peaks in the regions previously characterized by Coulomb blockade. The excited charge (via the two-photon process) out of the QD will be detected via a conductance change of the nearby charge-sensitive semiconductor element. The inherent three-dimensional carrier confinement and the reduced electron-phonon scattering will ensure a long lifetime to the intermediate confined state and very low dark currents, as well as very fast response times.

In summary, the obtained performances prove that the conceived architectures are ideal for the development of a new class of zero-dark-current thermoelectric photodetectors in NW QD architectures, and state of the art ultrafast, scalable and highly sensitive graphene detectors across the whole 0.3-4 THz range. Moreover, we investigated our QD NW SETs utilizing THz QCL emitting at 2.8THz as a potential technological platform for double photon detection mediated by intersubband transitions in the QD. However, this still requires a deep optimization of the device geometrical, thermal, electrical and optical parameters to clearly unveil a second order non-linear response.

References

1. Vitiello, M.S.; Coquillat, D.; Viti, L.; Ercolani, D.; Teppe, F.; Pitanti, A.; Beltram, F.; Sorba, L.; Knap, W.; Tredicucci, A. Room-Temperature Terahertz Detectors Based on Semiconductor Nanowire Field-Effect Transistors. *Nano Lett.* **2012**, *12*, 96–101, doi:10.1021/nl2030486.
2. Siegel, P.H. Terahertz Technology. *IEEE Trans. Microw. Theory Tech.* **2002**, *50*, 910–928, doi:10.1109/22.989974.
3. Hashim, A.M.; Kasai, S.; Hasegawa, H. Observation of First and Third Harmonic Responses in Two-Dimensional AlGaAs/GaAs HEMT Devices Due to Plasma Wave Interaction. *Superlattices Microstruct.* **2008**, *44*, 754–760, doi:10.1016/j.spmi.2008.08.003.
4. Tauk, R.; Teppe, F.; Boubanga, S.; Coquillat, D.; Knap, W.; Meziani, Y.M.; Gallon, C.; Boeuf, F.; Skotnicki, T.; Fenouillet-Beranger, C.; et al. Plasma Wave Detection of Terahertz Radiation by Silicon Field Effects Transistors: Responsivity and Noise Equivalent Power. *Appl. Phys. Lett.* **2006**, *89*, 1–4, doi:10.1063/1.2410215.
5. Zhang, X.; Ji, X.; Liao, Y.; Peng, J.; Zhu, C.; Yan, F. Performance Enhancement of CMOS Terahertz Detector by Drain Current∗. *Chinese Phys. B* **2017**, *26*, doi:10.1088/1674-1056/26/9/098401.
6. Schuster, F.; Coquillat, D.; Videlier, H.; Sakowicz, M.; Teppe, F.; Dussopt, L.; Giffard, B.; Skotnicki, T.; Knap, W. Broadband Terahertz Imaging with Highly Sensitive Silicon CMOS Detectors. *Opt. Express* **2011**, *19*, 7827, doi:10.1364/oe.19.007827.
7. Lewis, R.A. A Review of Terahertz Sources. *J. Phys. D. Appl. Phys.* **2014**, *47*, doi:10.1088/0022-3727/47/37/374001.
8. Dyakonov, M.; Shur, M.S. Plasma Wave Electronics for Terahertz Applications. *Terahertz Sources Syst.* **2001**, 187–207, doi:10.1007/978-94-010-0824-2_12.
9. Harris, B.J. What ’ s Up With Digital Downconverters — Part 1. *Analog dialogue* **2016**, 1–7.
10. Boyd, R.W. The Nonlinear Optical Susceptibility. *Nonlinear Opt.* **2008**, 1–67, doi:10.1016/b978-0-12-369470-6.00001-0.
11. Wang, K.; Mittleman, D.M. Metal Wires for Terahertz Wave Guiding. *Nature* **2004**, *432*, 376–379, doi:10.1038/nature03040.
12. Fitch, M.J.; Osiander, R. Terahertz Waves for Communications and Sensing. *Johns Hopkins APL Tech. Dig. (Applied Phys. Lab.* **2004**, *25*, 348–355.
13. Pawar, A.Y.; Sonawane, D.D.; Erande, K.B.; Derle, D. V. Terahertz Technology and Its Applications. *Drug Invent. Today* **2013**, *5*, 157–163, doi:10.1016/j.dit.2013.03.009.
14. Feiginov, M. Frequency Limitations of Resonant-Tunnelling Diodes in Sub-THz and THz Oscillators and Detectors. *J. Infrared, Millimeter, Terahertz Waves* **2019**, 365–394, doi:10.1007/s10762-019-00573-5.
15. R. Kohler, et al. Terahertz Semiconductor- Heterostructure Laser. *Lett. to Nat.* **2002**, *417*.
16. Khalatpour, A.; Paulsen, A.K.; Deimert, C.; Wasilewski, Z.R.; Hu, Q. High-Power Portable

Terahertz Laser Systems. *Nat. Photonics* **2021**, *15*, 16–20, doi:10.1038/s41566-020-00707-5.

17. Lin, T.T.; Hirayama, H. Improvement of Operation Temperature in GaAs/AlGaAs THz-QCLs by Utilizing High Al Composition Barrier. *Phys. Status Solidi Curr. Top. Solid State Phys.* **2013**, *10*, 1430–1433, doi:10.1002/pssc.201300216.
18. Brandstetter, M.; Deutsch, C.; Krall, M.; Detz, H.; Macfarland, D.C.; Zederbauer, T.; Andrews, A.M.; Schrenk, W.; Strasser, G.; Unterrainer, K. High Power Terahertz Quantum Cascade Lasers with Symmetric Wafer Bonded Active Regions. *Appl. Phys. Lett.* **2013**, *103*, 0–5, doi:10.1063/1.4826943.
19. Vitiello, M.S.; Consolino, L.; Bartalini, S.; Taschin, A.; Tredicucci, A.; Inguscio, M.; De Natale, P. Quantum-Limited Frequency Fluctuations in a Terahertz Laser. *Nat. Photonics* **2012**, *6*, 525–528, doi:10.1038/nphoton.2012.145.
20. Curwen, C.A.; Reno, J.L.; Williams, B.S. Broadband Continuous Single-Mode Tuning of a Short-Cavity Quantum-Cascade VECSEL. *Nat. Photonics* **2019**, *13*, 855–859, doi:10.1038/s41566-019-0518-z.
21. Rösch, M.; Beck, M.; Süess, M.J.; Bachmann, D.; Unterrainer, K.; Faist, J.; Scalari, G. Heterogeneous Terahertz Quantum Cascade Lasers Exceeding 1.9 THz Spectral Bandwidth and Featuring Dual Comb Operation. *Nanophotonics* **2018**, *7*, 237–242, doi:10.1515/nanoph-2017-0024.
22. Jiang, Y.; Vijayraghavan, K.; Jung, S.; Demmerle, F.; Boehm, G.; Amann, M.C.; Belkin, M.A. External Cavity Terahertz Quantum Cascade Laser Sources Based on Intra-Cavity Frequency Mixing with 1.2-5.9 THz Tuning Range. *J. Opt. (United Kingdom)* **2014**, *16*, doi:10.1088/2040-8978/16/9/094002.
23. Lee, A.W.M.; Qin, Q.; Kumar, S.; Williams, B.S.; Hu, Q.; Reno, J.L. Real-Time Terahertz Imaging over a Standoff Distance (>25 Meters). *Appl. Phys. Lett.* **2006**, *89*, 2–5, doi:10.1063/1.2360210.
24. Fathololoumi, S.; Dupont, E.; Chan, C.W.I.; Wasilewski, Z.R.; Laframboise, S.R.; Ban, D.; Mátyás, A.; Jirauschek, C.; Hu, Q.; Liu, H.C. Terahertz Quantum Cascade Lasers Operating up to ∼ 200 K with Optimized Oscillator Strength and Improved Injection Tunneling. *Opt. Express* **2012**, *20*, 3866, doi:10.1364/oe.20.003866.
25. Fukunaga, K.; Picollo, M. Terahertz Spectroscopy Applied to the Analysis of Artists' Materials. *Appl. Phys. A Mater. Sci. Process.* **2010**, *100*, 591–597, doi:10.1007/s00339-010-5643-y.
26. Jha, K.R.; Sharma, S.K. Waveguide Integrated Microstrip Patch Antenna at THz Frequency. *IEEE Antennas Propag. Soc. AP-S Int. Symp.* **2014**, 1851–1852, doi:10.1109/APS.2014.6905252.
27. Anastasi, R.F.; Madaras, E.I.; Seebo, J.P.; Smith, S.W.; Lomness, J.K.; Hintze, P.E.; Kammerer, C.C.; Winfree, W.P.; Russell, R.W. Terahertz NDE Application for Corrosion

Detection and Evaluation under Shuttle Tiles. *Nondestruct. Charact. Compos. Mater. Aerosp. Eng. Civ. Infrastructure, Homel. Secur. 2007* **2007**, *6531*, 65310W, doi:10.1117/12.715128.

28. Danciu, M.; Alexa-Stratulat, T.; Stefanescu, C.; Dodi, G.; Tamba, B.I.; Mihai, C.T.; Stanciu, G.D.; Luca, A.; Spiridon, I.A.; Ungureanu, L.B.; et al. Terahertz Spectroscopy and Imaging: A Cutting-Edge Method for Diagnosing Digestive Cancers. *Materials (Basel).* **2019**, *12*, 1–16, doi:10.3390/ma12091519.
29. Rogalski, A.; Sizov, F. Terahertz Detectors and Focal Plane Arrays. *Opto-Electronics Rev.* **2011**, *19*, 346–404, doi:10.2478/s11772-011-0033-3.
30. Jia-Ming Liu *Principles of Photonics*; Cambridge University Press, 2016; ISBN 9781316687109.
31. Chen, X.; Shieh, W. *High-Capacity Direct-Detection Systems*; Optical Fiber Telecommunications VII, 2020;
32. Richards, P.L. Bolometers for Infrared and Millimeter Waves. *J. Appl. Phys.* **1994**, *76*, 1–24, doi:10.1063/1.357128.
33. Dereniak, E.L.;Crowe, D.. *Optical Radiation Detectors*; Wiley, 1984; ISBN 0471897973, 9780471897972.
34. Henry W. Ott *Noise Reduction Techniques in Electronic Systems*; Second, Ed.; John Wiley & Sons, 1988;
35. Eppeldauer, G.P.; Martin, R.J. Photocurrent Measurement of PC and PV HgCdTe Detectors. *J. Res. Natl. Inst. Stand. Technol.* **2001**, *106*, 577–587, doi:10.6028/jres.106.024.
36. Atalla, M.R.M.; Assali, S.; Koelling, S.; Attiaoui, A.; Moutanabbir, O. High-Bandwidth Extended-SWIR GeSn Photodetectors on Silicon Achieving Ultrafast Broadband Spectroscopic Response. *ACS Photonics* **2022**, *9*, 1425–1433, doi:10.1021/acsphotonics.2c00260.
37. Sizov, F. Terahertz Radiation Detectors: The State-of the-Art. *Semicond. Sci. Technol.* **2018**, *33*.
38. Hyseni, G.; Caka, N.; Hyseni, K. Infrared Thermal Detectors Parameters: Semiconductor Bolometers versus Pyroelectrics. *WSEAS Trans. Circuits Syst.* **2010**, *9*, 238–247.
39. Https://Www.Pyrosensor.de/High-Sensitive-924646.Html. *Accessed on 26/10/22*.
40. A. Rogalski *Infrared Detectors*; 2nd Editio.; CRC Press: Boca Raton, 2010; ISBN 9780429192982.
41. Oda, N.; Lee, A.W.M.; Ishi, T.; Hosako, I.; Hu, Q. Proposal for Real-Time Terahertz Imaging System with Palm-Size Terahertz Camera and Compact Quantum Cascade Laser. *Terahertz Physics, Devices, Syst. VI Adv. Appl. Ind. Def.* **2012**, *8363*, 83630A-83630A – 13, doi:10.1117/12.917682.
42. D. C. Alsop, C. Inman, A. E. Lange, and T.W. Design and Construction of High-Sensitivity, Infrared Bolometers for Operation at 300 MK. *Appl. Opt.* **1992**, *31*, 6610–6615.

43. Shugurov, K.Y.; Mozharov, A.M.; Mukhin, I.S. Numerical Study of Schottky Diode Based on Single GaN NW on Si. *J. Phys. Conf. Ser.* **2020**, *1695*, doi:10.1088/1742-6596/1695/1/012172.

44. Lewis, R.A. A Review of Terahertz Detectors. *J. Phys. D. Appl. Phys.* **2019**, *52*, doi:10.1088/1361-6463/ab31d5.

45. Yang, L.; Yao, W.; Liu, Y.; Wang, L.; Dai, Y.; Liu, H.; Wang, F.; Ren, Y.; Wu, Z.; Liu, Y.; et al. Low Capacitance AlGaN/GaN Based Air-Bridge Structure Planar Schottky Diode with a Half through-Hole. *AIP Adv.* **2020**, *10*, doi:10.1063/5.0004470.

46. Friederich, F.; Von Spiegel, W.; Bauer, M.; Meng, F.; Thomson, M.D.; Boppel, S.; Lisauskas, A.; Hils, B.; Krozer, V.; Keil, A.; et al. THz Active Imaging Systems with Real-Time Capabilities. *IEEE Trans. Terahertz Sci. Technol.* **2011**, *1*, 183–200, doi:10.1109/TTHZ.2011.2159559.

47. Han, R.; Zhang, Y.; Coquillat, D.; Videlier, H.; Knap, W.; Brown, E.; Kenneth, K.O. A 280-GHz Schottky Diode Detector in 130-Nm Digital CMOS. *IEEE J. Solid-State Circuits* **2011**, *46*, 2602–2612, doi:10.1109/JSSC.2011.2165234.

48. Yachmenev, A.E.; Khabibullin, R.A.; Ponomarev, D.S. Recent Advances in THz Detectors Based on Semiconductor Structures with Quantum Confinement: A Review. *J. Phys. D. Appl. Phys.* **2022**, *55*, doi:10.1088/1361-6463/ac43dd.

49. Liu, H.C.; Dudek, E.; Shen, A.; Dupont, E.; Song, C.Y.; Wasilewski, Z.R.; Buchanan, M. QWIPs Designed for High Absorption and High Operating Temperature. *Int. J. High Speed Electron. Syst.* **2002**, *12*, 803–819, doi:10.1142/S0129156402001708.

50. But, D. Silicon Based Terahertz Radiation Detectors Dmytro But To Cite This Version : HAL Id : Tel-01811025 Spécialité : Physique Détecteurs de Radiation THz à Base de Silicium. **2018**.

51. Knap, W.; Deng, Y.; Rumyantsev, S.; Shur, M.S. Resonant Detection of Subterahertz and Terahertz Radiation by Plasma Waves in Submicron Field-Effect Transistors. *Appl. Phys. Lett.* **2012**, *4637*, 1–4, doi:10.1063/1.1525851.

52. Teppe, F.; Coquillat, D.; Nadar, S. Current Driven Resonant Plasma Wave Detection of Terahertz Radiation: Toward the Dyakonov–Shur Instability. *Appl. Phys. Lett.* **2008**, *212101*, 1–4, doi:10.1063/1.2936077.

53. Dyakonov, M.I. Comptes Rendus Physique Generation and Detection of Terahertz Radiation by Field Effect Transistors Génération et Détection de Rayonnement Térahertz Avec Des Transistors à Effet de Champ. *Comptes Rendus Phys.* **2010**, *11*, 413–420, doi:10.1016/j.crhy.2010.05.003.

54. Lisauskas, A.; Pfeiffer, U.; Öjefors, E.; Bolìvar, P.H.; Glaab, D.; Lisauskas, A.; Pfeiffer, U.; Öjefors, E.; Bolìvar, P.H. Rational Design of High-Responsivity Detectors of Terahertz Radiation Based on Distributed Self-Mixing in Silicon Field-Effect Transistors Rational Design of High-Responsivity Detectors of Terahertz Radiation Based on Distributed Self-

Mixing in Silicon Fi. *J. Appl. Phys.* **2013**, *114511*, doi:10.1063/1.3140611.

55. Öjefors, E.; Pfeiffer, U.R.; Member, S.; Lisauskas, A.; Roskos, H.G. A 0 . 65 THz Focal-Plane Array in a Quarter-Micron. *IEEE J. Solid-State Circuits* **2009**, *44*, 1968–1976.
56. Drexler, C.; Dyakonova, N.; Olbrich, P.; Karch, J.; Schafberger, M.; Drexler, C.; Dyakonova, N.; Olbrich, P.; Karch, J.; Schafberger, M.; et al. Helicity Sensitive Terahertz Radiation Detection by Field Effect Transistors. *J. Appl. Phys.* **2012**, *124504*, doi:10.1063/1.4729043.
57. Schuster, F.; Coquillat, D.; Videlier, H.; Sakowicz, M.; Teppe, F.; Dussopt, L.; Giffard, B.; Skotnicki, T.; Knap, W. Broadband Terahertz Imaging with Highly Sensitive Silicon CMOS Detectors. *Opt. Express* **2011**, *19*, 7827–7832.
58. Vitiello, M.S.; Coquillat, D.; Viti, L.; Ercolani, D.; Teppe, F.; Pitanti, A.; Beltram, F.; Sorba, L.; Knap, W.; Tredicucci, A. Room-Temperature Terahertz Detectors Based on Semiconductor Nanowire Field-Effect Transistors. *Nano Lett.* **2012**.
59. Koppens, F.H.L.; Mueller, T.; Avouris, P.; Ferrari, A.C.; Vitiello, M.S.; Polini, M. Photodetectors Based on Graphene, Other Two-Dimensional Materials and Hybrid Systems. *Nat. Publ. Gr.* **2014**, *9*, doi:10.1038/nnano.2014.215.
60. Dyakonov, M.; Shur, M. Shallow Water Analogy for a Ballistic Field Effect Transistor: New Mechanism of Plasma Wave Generation by Dc Current. *Phys. Rev. Lett.* **1993**, *71*, 2465–2468, doi:10.1103/PhysRevLett.71.2465.
61. Knap, W.; Dyakonov, M.; Coquillat, D.; Teppe, F.; Dyakonova, N.; Łusakowski, J.; Karpierz, K.; Sakowicz, M.; Valusis, G.; Seliuta, D.; et al. Field Effect Transistors for Terahertz Detection: Physics and First Imaging Applications. *J. Infrared, Millimeter, Terahertz Waves* **2009**, *30*, 1319–1337, doi:10.1007/s10762-009-9564-9.
62. Knap, W.; Lusakowski, J.; Parenty, T.; Bollaert, S.; Cappy, A.; Popov, V. V.; Shur, M.S. Terahertz Emission by Plasma Waves in 60 Nm Gate High Electron Mobility Transistors. *Appl. Phys. Lett.* **2004**, *84*, 2331–2333, doi:10.1063/1.1689401.
63. Maas, S.A. A Gaas Mesfet Mixer with Very Low Intermodulation. *IEEE Trans. Microw. Theory Tech.* **1987**, *35*, 425–429, doi:10.1109/TMTT.1987.1133665.
64. Dyakonov, M.; Shur, M. Detection, Mixing, and Frequency Multiplication of Terahertz Radiation by Two-Dimensional Electronic Fluid. *IEEE Trans. Electron Devices* **1996**, *43*, 380–387, doi:10.1109/16.485650.
65. Dyakonov, M.I. Generation and Detection of Terahertz Radiation by Field Effect Transistors. *Prog. Electromagn. Res. Symp.* **2011**, *11*, 1261–1265, doi:10.1016/j.crhy.2010.05.003.
66. Massicotte, M.; Soavi, G.; Principi, A.; Tielrooij, K.J. Hot Carriers in Graphene-Fundamentals and Applications. *Nanoscale* **2021**, *13*, 8376–8411, doi:10.1039/d0nr09166a.
67. Pogna, E.A.A.; Jia, X.; Principi, A.; Block, A.; Banszerus, L.; Zhang, J.; Liu, X.; Sohier, T.; Forti, S.; Soundarapandian, K.; et al. Hot-Carrier Cooling in High-Quality Graphene Is Intrinsically Limited by Optical Phonons. *ACS Nano* **2021**, *15*, 11285–11295,

doi:10.1021/acsnano.0c10864.

68. Goupil, C.; Seifert, W.; Zabrocki, K.; Müller, E.; Snyder, G.J. Thermodynamics of Thermoelectric Phenomena and Applications. *Entropy* **2011**, *13*, 1481–1517, doi:10.3390/e13081481.
69. Xu, X.; Gabor, N.M.; Alden, J.S.; Van Der Zande, A.M.; McEuen, P.L. Photo-Thermoelectric Effect at a Graphene Interface Junction. *Nano Lett.* **2010**, *10*, 562–566, doi:10.1021/nl903451y.
70. Sun, D.; Aivazian, G.; Jones, A.M.; Ross, J.S.; Yao, W.; Cobden, D.; Xu, X. Ultrafast Hot-Carrier-Dominated Photocurrent in Graphene. *Nat. Nanotechnol.* **2012**, *7*, 114–118, doi:10.1038/nnano.2011.243.
71. Asgari, M.; Riccardi, E.; Balci, O.; De Fazio, D.; Shinde, S.M.; Zhang, J.; Mignuzzi, S.; Koppens, F.H.L.; Ferrari, A.C.; Viti, L.; et al. Chip-Scalable, Room-Temperature, Zero-Bias, Graphene-Based Terahertz Detectors with Nanosecond Response Time. *ACS Nano* **2021**, *15*, 17966–17976, doi:10.1021/acsnano.1c06432.
72. Freitag, M.; Low, T.; Avouris, P. Increased Responsivity of Suspended Graphene Photodetectors. *Nano Lett.* **2013**, *13*, 1644–1648, doi:10.1021/nl4001037.
73. Wu, Q.; Voorhis, T. Van; Nocera, D.G.; Nocera, D.G.; Bansal, A.; Turner, J.A.; Kapur, M.; Kainthla, R.C.; Bockris, J.O.M.; Turner, J.A.; et al. References and Notes 1. *Science (80-.).* **2011**, *334*, 648–653.
74. Schuler, S.; Schall, D.; Neumaier, D.; Dobusch, L.; Bethge, O.; Schwarz, B.; Krall, M.; Mueller, T. Controlled Generation of a P-n Junction in a Waveguide Integrated Graphene Photodetector. *Nano Lett.* **2016**, *16*, 7107–7112, doi:10.1021/acs.nanolett.6b03374.
75. Gan, X.; Shiue, R.J.; Gao, Y.; Meric, I.; Heinz, T.F.; Shepard, K.; Hone, J.; Assefa, S.; Englund, D. Chip-Integrated Ultrafast Graphene Photodetector with High Responsivity. *Nat. Photonics* **2013**, *7*, 883–887, doi:10.1038/nphoton.2013.253.
76. Mueller, T.; Xia, F.; Avouris, P. Graphene Photodetectors for High-Speed Optical Communications. *Nat. Photonics* **2010**, *4*, 297–301, doi:10.1038/nphoton.2010.40.
77. M. Asgari et al. Terahertz Photodetection in Scalable Single-Layer-Graphene and Hexagonal Boron Nitride Heterostructures. *Appl. Phys. Lett.* **2022**, doi:https://doi.org/10.1063/5.0097726.
78. Viti, L.; Purdie, D.G.; Lombardo, A.; Ferrari, A.C.; Vitiello, M.S. HBN-Encapsulated, Graphene-Based, Room-Temperature Terahertz Receivers, with High Speed and Low Noise. *Nano Lett.* **2020**, doi:10.1021/acs.nanolett.9b05207.
79. Viti, L.; Cadore, A.R.; Yang, X.; Vorobiev, A.; Muench, J.E.; Watanabe, K.; Taniguchi, T.; Stake, J.; Ferrari, A.C.; Vitiello, M.S. Thermoelectric Graphene Photodetectors with Sub-Nanosecond Response Times at Terahertz Frequencies. *Front. Opt. Photonics* **2021**, *10*, 89–98, doi:10.1515/9783110710687-007.
80. Groenendijk, D.J.; Buscema, M.; Steele, G.A.; Bratschitsch, R.; Zant, H.S.J. Van Der;

Castellanos-gomez, A. Photovoltaic and Photothermoelectric E Ff Ect in a Double-Gated WSe 2 Device. *Nano Lett.* **2014**.

81. Low, T.; Engel, M.; Steiner, M.; Avouris, P. Origin of Photoresponse in Black Phosphorus Phototransistors. *Phys. Rev. B - Condens. Matter Mater. Phys.* **2014**, *90*, 1–5, doi:10.1103/PhysRevB.90.081408.
82. Song, J.C.W.; Rudner, M.S.; Marcus, C.M.; Levitov, L.S. Hot Carrier Transport and Photocurrent Response in Graphene. *Nano Lett.* **2011**, *11*, 4688–4692, doi:10.1021/nl202318u.
83. Brida, D.; Tomadin, A.; Manzoni, C.; Kim, Y.J.; Lombardo, A.; Milana, S.; Nair, R.R.; Novoselov, K.S.; Ferrari, A.C.; Cerullo, G.; et al. Ultrafast Collinear Scattering and Carrier Multiplication in Graphene. *Nat. Commun.* **2013**, *4*, 1–9, doi:10.1038/ncomms2987.
84. Zuev, Y.M.; Chang, W.; Kim, P. Thermoelectric and Magnetothermoelectric Transport Measurements of Graphene. *Phys. Rev. Lett.* **2009**, *102*, 1–4, doi:10.1103/PhysRevLett.102.096807.
85. Hwang, E.H.; Rossi, E.; Das Sarma, S. Theory of Thermopower in Two-Dimensional Graphene. *Phys. Rev. B - Condens. Matter Mater. Phys.* **2009**, *80*, 1–5, doi:10.1103/PhysRevB.80.235415.
86. Gabor, N.M. et al. Hot Carrier-Assisted Intrinsic Photoresponse in Graphene. *Science (80-.).* **2011**, *334*, 648–653.
87. Lui, C.H.; Mak, K.F.; Shan, J.; Heinz, T.F. Ultrafast Photoluminescence from Graphene. *Phys. Rev. Lett.* **2010**, *105*, 1–4, doi:10.1103/PhysRevLett.105.127404.
88. Mihnev, M.T.; Kadi, F.; Divin, C.J.; Winzer, T.; Lee, S.; Liu, C.H.; Zhong, Z.; Berger, C.; De Heer, W.A.; Malic, E.; et al. Microscopic Origins of the Terahertz Carrier Relaxation and Cooling Dynamics in Graphene. *Nat. Commun.* **2016**, *7*, doi:10.1038/ncomms11617.
89. Han, Q.; Gao, T.; Zhang, R.; Chen, Y.; Chen, J.; Liu, G.; Zhang, Y.; Liu, Z.; Wu, X.; Yu, D. Highly Sensitive Hot Electron Bolometer Based on Disordered Graphene. *Sci. Rep.* **2013**, *3*, 1–6, doi:10.1038/srep03533.
90. Yang, W.; Berthou, S.; Lu, X.; Wilmart, Q.; Denis, A.; Rosticher, M.; Taniguchi, T.; Watanabe, K.; Fève, G.; Berroir, J.M.; et al. A Graphene Zener-Klein Transistor Cooled by a Hyperbolic Substrate. *Nat. Nanotechnol.* **2018**, *13*, 47–52, doi:10.1038/s41565-017-0007-9.
91. Xia, F.; Mueller, T.; Lin, Y.M.; Valdes-Garcia, A.; Avouris, P. Ultrafast Graphene Photodetector. *Nat. Nanotechnol.* **2009**, *4*, 839–843, doi:10.1038/nnano.2009.292.
92. Shiue, R.J.; Gao, Y.; Wang, Y.; Peng, C.; Robertson, A.D.; Efetov, D.K.; Assefa, S.; Koppens, F.H.L.; Hone, J.; Englund, D. High-Responsivity Graphene-Boron Nitride Photodetector and Autocorrelator in a Silicon Photonic Integrated Circuit. *Nano Lett.* **2015**, *15*, 7288–7293, doi:10.1021/acs.nanolett.5b02368.
93. Buchal, C.; Loken, M.; Siegert, M. Silicon-Based Optoelectronics. *Mater. Res. Soc. Symp. - Proc.* **1998**, *486*, 3–19, doi:10.1557/s0883769400030219.

94. Freitag, M.; Low, T.; Xia, F.; Avouris, P. Photoconductivity of Biased Graphene. *Nat. Photonics* **2013**, *7*, 53–59, doi:10.1038/nphoton.2012.314.

95. Yan, J.; Kim, M.H.; Elle, J.A.; Sushkov, A.B.; Jenkins, G.S.; Milchberg, H.M.; Fuhrer, M.S.; Drew, H.D. Dual-Gated Bilayer Graphene Hot-Electron Bolometer. *Nat. Nanotechnol.* **2012**, *7*, 472–478, doi:10.1038/nnano.2012.88.

96. Engel, M.; Steiner, M.; Avouris, P. Black Phosphorus Photodetector for Multispectral, High-Resolution Imaging. *Nano Lett.* **2014**, *14*, 6414–6417, doi:10.1021/nl502928y.

97. Vitiello, M.S.; Consolino, L.; Inguscio, M.; De Natale, P. Toward New Frontiers for Terahertz Quantum Cascade Laser Frequency Combs. *Front. Opt. Photonics* **2021**, *10*, 189–196, doi:10.1515/9783110710687-017.

98. Simoens, F.; Meilhan, J. Terahertz Real-Time Imaging Uncooled Array Based on Antenna- and Cavity-Coupled Bolometers. *Philos. Trans. R. Soc. A Math. Phys. Eng. Sci.* **2014**, *372*, doi:10.1098/rsta.2013.0111.

99. Ikamas, K.; Lisauskas, A.; Boppel, S.; Hu, Q.; Roskos, H.G. Efficient Detection of 3 THz Radiation from Quantum Cascade Laser Using Silicon CMOS Detectors. *J. Infrared, Millimeter, Terahertz Waves* **2017**, *38*, 1183–1188, doi:10.1007/s10762-017-0407-9.

100. Lisauskas, A.; Bauer, M.; Boppel, S.; Mundt, M.; Khamaisi, B.; Socher, E.; Venckevičius, R.; Minkevičius, L.; Kašalynas, I.; Seliuta, D.; et al. Exploration of Terahertz Imaging with Silicon MOSFETs. *J. Infrared, Millimeter, Terahertz Waves* **2014**, *35*, 63–80, doi:10.1007/s10762-013-0047-7.

101. Romagnoli, M.; Sorianello, V.; Midrio, M.; Koppens, F.H.L.; Huyghebaert, C.; Neumaier, D.; Galli, P.; Templ, W.; D'Errico, A.; Ferrari, A.C. Graphene-Based Integrated Photonics for next-Generation Datacom and Telecom. *Nat. Rev. Mater.* **2018**, *3*, 392–414, doi:10.1038/s41578-018-0040-9.

102. Goossens, S.; Navickaite, G.; Monasterio, C.; Gupta, S.; Piqueras, J.J.; Pérez, R.; Burwell, G.; Nikitskiy, I.; Lasanta, T.; Galán, T.; et al. Broadband Image Sensor Array Based on Graphene-CMOS Integration. *Nat. Photonics* **2017**, *11*, 366–371, doi:10.1038/nphoton.2017.75.

103. Castro Neto, A.H.; Guinea, F.; Peres, N.M.R.; Novoselov, K.S.; Geim, A.K. The Electronic Properties of Graphene. *Rev. Mod. Phys.* **2009**, *81*, 109–162, doi:10.1103/RevModPhys.81.109.

104. Falkovsky, L.A. Optical Properties of Graphene. *J. Phys. Conf. Ser.* **2008**, *129*, doi:10.1088/1742-6596/129/1/012004.

105. Pop, E.; Varshney, V.; Roy, A.K. Thermal Properties of Graphene: Fundamentals and Applications. *MRS Bull.* **2012**, *37*, 1273–1281, doi:10.1557/mrs.2012.203.

106. Brida, D.; Tomadin, A.; Manzoni, C.; Kim, Y.J.; Lombardo, A.; Milana, S.; Nair, R.R.; Novoselov, K.S.; Ferrari, A.C.; Cerullo, G.; et al. Ultrafast Collinear Scattering and Carrier Multiplication in Graphene. *Nat. Commun.* **2013**, *4*, doi:10.1038/ncomms2987.

107. Viti, L.; Vitiello, M.S. Tailored Nano-Electronics and Photonics with Two-Dimensional Materials at Terahertz Frequencies. *J. Appl. Phys.* **2021**, *130*, doi:10.1063/5.0065595.

108. Bolotin, K.I.; Sikes, K.J.; Jiang, Z.; Klima, M.; Fudenberg, G.; Hone, J.; Kim, P.; Stormer, H.L. Ultrahigh Electron Mobility in Suspended Graphene. *Solid State Commun.* **2008**, *146*, 351–355, doi:10.1016/j.ssc.2008.02.024.

109. Chen, Z.; Jang, W.; Bao, W.; Lau, C.N.; Dames, C. Thermal Contact Resistance between Graphene and Silicon Dioxide. *Appl. Phys. Lett.* **2009**, *95*, 3–6, doi:10.1063/1.3245315.

110. De Fazio, D.; Purdie, D.G.; Ott, A.K.; Braeuninger-Weimer, P.; Khodkov, T.; Goossens, S.; Taniguchi, T.; Watanabe, K.; Livreri, P.; Koppens, F.H.L.; et al. High-Mobility, Wet-Transferred Graphene Grown by Chemical Vapor Deposition. *ACS Nano* **2019**, *13*, 8926–8935, doi:10.1021/acsnano.9b02621.

111. Sassi, U.; Parret, R.; Nanot, S.; Bruna, M.; Borini, S.; De Fazio, D.; Zhao, Z.; Lidorikis, E.; Koppens, F.H.L.; Ferrari, A.C.; et al. Graphene-Based Mid-Infrared Room-Temperature Pyroelectric Bolometers with Ultrahigh Temperature Coefficient of Resistance. *Nat. Commun.* **2017**, *8*, doi:10.1038/ncomms14311.

112. Mišeikis, V.; Marconi, S.; Giambra, M.A.; Montanaro, A.; Martini, L.; Fabbri, F.; Pezzini, S.; Piccinini, G.; Forti, S.; Terrés, B.; et al. Ultrafast, Zero-Bias, Graphene Photodetectors with Polymeric Gate Dielectric on Passive Photonic Waveguides. *ACS Nano* **2020**, *14*, 11190–11204, doi:10.1021/acsnano.0c02738.

113. Giambra, M.A. e al. Wafer-Scale Integration of Graphene-Based Photonic Devices. *ACS Nano* **2021**, *15*, 3171–3187, doi:10.1021/acsnano.0c09758.

114. Cai, X.; Sushkov, A.B.; Suess, R.J.; Jadidi, M.M.; Jenkins, G.S.; Nyakiti, L.O.; Myers-Ward, R.L.; Li, S.; Yan, J.; Gaskill, D.K.; et al. Sensitive Room-Temperature Terahertz Detection via the Photothermoelectric Effect in Graphene. *Nat. Nanotechnol.* **2014**, *9*, 814–819, doi:10.1038/nnano.2014.182.

115. Viti, L.; Purdie, D.G.; Lombardo, A.; Ferrari, A.C.; Vitiello, M.S. HBN-Encapsulated, Graphene-Based, Room-Temperature Terahertz Receivers, with High Speed and Low Noise. *Nano Lett.* **2020**, *20*, 3169–3177, doi:10.1021/acs.nanolett.9b05207.

116. Castilla, S.; Terrés, B.; Autore, M.; Viti, L.; Li, J.; Nikitin, A.Y.; Vangelidis, I.; Watanabe, K.; Taniguchi, T.; Lidorikis, E.; et al. Fast and Sensitive Terahertz Detection Using an Antenna-Integrated Graphene Pn Junction. *Nano Lett.* **2019**, *19*, 2765–2773, doi:10.1021/acs.nanolett.8b04171.

117. Piscanec, S.; Lazzeri, M.; Mauri, F.; Ferrari, A.C.; Robertson, J. Kohn Anomalies and Electron-Phonon Interactions in Graphite. *Phys. Rev. Lett.* **2004**, *93*, 1–4, doi:10.1103/PhysRevLett.93.185503.

118. Soavi, G.; Wang, G.; Rostami, H.; Purdie, D.G.; De Fazio, D.; Ma, T.; Luo, B.; Wang, J.; Ott, A.K.; Yoon, D.; et al. Broadband, Electrically Tunable Third-Harmonic Generation in

Graphene. *Nat. Nanotechnol.* **2018**, *13*, 583–588, doi:10.1038/s41565-018-0145-8.

119. Espinosa-Ortega, T.; Luk'Yanchuk, I.A.; Rubo, Y.G. Magnetic Properties of Graphene Quantum Dots. *Phys. Rev. B - Condens. Matter Mater. Phys.* **2013**, *87*, 1–6, doi:10.1103/PhysRevB.87.205434.
120. Tielrooij, K.J.; Piatkowski, L.; Massicotte, M.; Woessner, A.; Ma, Q.; Lee, Y.; Myhro, K.S.; Lau, C.N.; Jarillo-Herrero, P.; Van Hulst, N.F.; et al. Generation of Photovoltage in Graphene on a Femtosecond Timescale through Efficient Carrier Heating. *Nat. Nanotechnol.* **2015**, *10*, 437–443, doi:10.1038/nnano.2015.54.
121. Tielrooij, K.J.; Hesp, N.C.H.; Principi, A.; Lundeberg, M.B.; Pogna, E.A.A.; Banszerus, L.; Mics, Z.; Massicotte, M.; Schmidt, P.; Davydovskaya, D.; et al. Out-of-Plane Heat Transfer in van Der Waals Stacks through Electron-Hyperbolic Phonon Coupling. *Nat. Nanotechnol.* **2018**, *13*, 41–46, doi:10.1038/s41565-017-0008-8.
122. Balandin, A.A. Low-Frequency 1/f Noise in Graphene Devices. *Nat. Nanotechnol.* **2013**, *8*, 549–555, doi:10.1038/nnano.2013.144.
123. Castilla, S.; Vangelidis, I.; Pusapati, V.V.; Goldstein, J.; Autore, M.; Slipchenko, T.; Rajendran, K.; Kim, S.; Watanabe, K.; Taniguchi, T.; et al. Plasmonic Antenna Coupling to Hyperbolic Phonon-Polaritons for Sensitive and Fast Mid-Infrared Photodetection with Graphene. *Nat. Commun.* **2020**, *11*, 1–7, doi:10.1038/s41467-020-18544-z.
124. Zak, A.; Andersson, M.A.; Bauer, M.; Matukas, J.; Lisauskas, A.; Roskos, H.G.; Stake, J. Antenna-Integrated 0.6 THz FET Direct Detectors Based on CVD Graphene. *Nano Lett.* **2014**, *14*, 5834–5838, doi:10.1021/nl5027309.
125. Yang, H.; Qin, S.; Zheng, X.; Wang, G.; Tan, Y.; Peng, G.; Zhang, X. An Al2O3 Gating Substrate for the Greater Performance of Field Effect Transistors Based on Two-Dimensional Materials. *Nanomaterials* **2017**, *7*, doi:10.3390/nano7100286.
126. Shautsova, V.; Gilbertson, A.M.; Black, N.C.G.; Maier, S.A.; Cohen, L.F. Hexagonal Boron Nitride Assisted Transfer and Encapsulation of Large Area CVD Graphene. *Sci. Rep.* **2016**, *6*, 1–8, doi:10.1038/srep30210.
127. Piper, J.R.; Fan, S. Total Absorption in a Graphene Monolayer in the Optical Regime by Critical Coupling with a Photonic Crystal Guided Resonance. *ACS Photonics* **2014**, *1*, 347–353, doi:10.1021/ph400090p.
128. Nair, R.R.; Blake, P.; Grigorenko, A.N.; Novoselov, K.S.; Booth, T.J.; Stauber, T.; Peres, N.M.R.; Geim, A.K. Fine Structure Constant Defines Visual Transparency of Graphene. *Science (80-.).* **2008**, *320*, 1308, doi:10.1126/science.1156965.
129. Cao, Y.; Fatemi, V.; Fang, S.; Watanabe, K.; Taniguchi, T.; Kaxiras, E.; Jarillo-Herrero, P. Unconventional Superconductivity in Magic-Angle Graphene Superlattices. *Nature* **2018**, *556*, 43–50, doi:10.1038/nature26160.
130. Adam, S.; Hwang, E.H.; Galitski, V.M.; Das Sarma, S. A Self-Consistent Theory for Graphene

Transport. *Proc. Natl. Acad. Sci. U. S. A.* **2007**, *104*, 18392–18397, doi:10.1073/pnas.0704772104.

131. Hafez, H.A.; Kovalev, S.; Tielrooij, K.J.; Bonn, M.; Gensch, M.; Turchinovich, D. Terahertz Nonlinear Optics of Graphene: From Saturable Absorption to High-Harmonics Generation. *Adv. Opt. Mater.* **2020**, *8*, doi:10.1002/adom.201900771.
132. Higuchi, T.; Heide, C.; Ullmann, K.; Weber, H.B.; Hommelhoff, P. Light-Field-Driven Currents in Graphene. *Nature* **2017**, *550*, 224–228, doi:10.1038/nature23900.
133. Yoshikawa, N.; Tamaya, T.; Tanaka, K. Optics: High-Harmonic Generation in Graphene Enhanced by Elliptically Polarized Light Excitation. *Science (80-.).* **2017**, *356*, 736–738, doi:10.1126/science.aam8861.
134. Hafez, H.A.; Kovalev, S.; Deinert, J.C.; Mics, Z.; Green, B.; Awari, N.; Chen, M.; Germanskiy, S.; Lehnert, U.; Teichert, J.; et al. Extremely Efficient Terahertz High-Harmonic Generation in Graphene by Hot Dirac Fermions. *Nature* **2018**, *561*, 507–511, doi:10.1038/s41586-018-0508-1.
135. Das Sarma, S.; Adam, S.; Hwang, E.H.; Rossi, E. Electronic Transport in Two-Dimensional Graphene. *Rev. Mod. Phys.* **2011**, *83*, 407–470, doi:10.1103/RevModPhys.83.407.
136. Mics, Z.; Tielrooij, K.J.; Parvez, K.; Jensen, S.A.; Ivanov, I.; Feng, X.; Müllen, K.; Bonn, M.; Turchinovich, D. Thermodynamic Picture of Ultrafast Charge Transport in Graphene. *Nat. Commun.* **2015**, *6*, 1–7, doi:10.1038/ncomms8655.
137. Miseikis, V.; Convertino, D.; Mishra, N.; Gemmi, M.; Mashoff, T.; Heun, S.; Haghighian, N.; Bisio, F.; Canepa, M.; Piazza, V.; et al. Rapid CVD Growth of Millimetre-Sized Single Crystal Graphene Using a Cold-Wall Reactor. *2D Mater.* **2015**, *2*, 14006, doi:10.1088/2053-1583/2/1/014006.
138. Braeuninger-Weimer, P.; Brennan, B.; Pollard, A.J.; Hofmann, S. Understanding and Controlling Cu-Catalyzed Graphene Nucleation: The Role of Impurities, Roughness, and Oxygen Scavenging. *Chem. Mater.* **2016**, *28*, 8905–8915, doi:10.1021/acs.chemmater.6b03241.
139. Ferrari, A.C.; Meyer, J.C.; Scardaci, V.; Casiraghi, C.; Lazzeri, M.; Mauri, F.; Piscanec, S.; Jiang, D.; Novoselov, K.S.; Roth, S.; et al. Raman Spectrum of Graphene and Graphene Layers. *Phys. Rev. Lett.* **2006**, *97*, 1–4, doi:10.1103/PhysRevLett.97.187401.
140. Ferrari, A.C.; Basko, D.M. Raman Spectroscopy as a Versatile Tool for Studying the Properties of Graphene. *Nat. Nanotechnol.* **2013**, *8*, 235–246, doi:10.1038/nnano.2013.46.
141. Lagatsky, A.A.; Sun, Z.; Kulmala, T.S.; Sundaram, R.S.; Milana, S.; Torrisi, F.; Antipov, O.L.; Lee, Y.; Ahn, J.H.; Brown, C.T.A.; et al. 2 Mm Solid-State Laser Mode-Locked By Single-Layer Graphene. *Appl. Phys. Lett.* **2013**, *102*, 1–5, doi:10.1063/1.4773990.
142. Das, A.; Pisana, S.; Chakraborty, B.; Piscanec, S.; Saha, S.K.; Waghmare, U. V.; Novoselov, K.S.; Krishnamurthy, H.R.; Geim, A.K.; Ferrari, A.C.; et al. Monitoring Dopants by Raman

Scattering in an Electrochemically Top-Gated Graphene Transistor. *Nat. Nanotechnol.* **2008**, *3*, 210–215, doi:10.1038/nnano.2008.67.

143. Bruna, M.; Ott, A.K.; Ijäs, M.; Yoon, D.; Sassi, U.; Ferrari, A.C. Doping Dependence of the Raman Spectrum of Defected Graphene. *ACS Nano* **2014**, *8*, 7432–7441, doi:10.1021/nn502676g.
144. A. C. Ferrari and J. Robertson Interpretation of Raman Spectra of Disordered and Amorphous Carbon. *Phys. Rev. B* **2000**, *61*, 632–645, doi:10.1007/BF02543692.
145. Basko, D.M.; Piscanec, S.; Ferrari, A.C. Electron-Electron Interactions and Doping Dependence of the Two-Phonon Raman Intensity in Graphene. *Phys. Rev. B* **2009**, *80*, 1–10, doi:10.1103/physrevb.80.165413.
146. Lim, G.; Kihm, K.D.; Kim, H.G.; Lee, W.; Lee, W.; Pyun, K.R.; Cheon, S.; Lee, P.; Min, J.Y.; Ko, S.H. Enhanced Thermoelectric Conversion Efficiency of CVD Graphene with Reduced Grain Sizes. *Nanomaterials* **2018**, *8*, 1–9, doi:10.3390/nano8070557.
147. Bianco, F.; Miseikis, V.; Perenzoni, D.; Coletti, C.; Perenzoni, M.; Tredicucci, A. Antenna-Coupled Graphene Field-Effect Transistors as a Terahertz Imaging Array. *IEEE Trans. Terahertz Sci. Technol.* **2021**, *11*, 70–78, doi:10.1109/TTHZ.2020.3021353.
148. Pierre-Noël Favennec *Electromagnetic Waves 2: Antennas*; Wiley, 2021; ISBN 9781119818397.
149. Balanis, C.A. *Antenna Theory: Analysis and Design, 3rd Edition*; 2005; ISBN 047166782X.
150. Kim, S.; Nah, J.; Jo, I.; Shahrjerdi, D.; Colombo, L.; Yao, Z.; Tutuc, E.; Banerjee, S.K. Realization of a High Mobility Dual-Gated Graphene Field-Effect Transistor with Al2O3 Dielectric. *Appl. Phys. Lett.* **2009**, *94*, 2007–2010, doi:10.1063/1.3077021.
151. Chen, J.H.; Jang, C.; Adam, S.; Fuhrer, M.S.; Williams, E.D.; Ishigami, M. Charged-Impurity Scattering in Graphene. *Nat. Phys.* **2008**, *4*, 377–381, doi:10.1038/nphys935.
152. Bandurin, D.A.; Gayduchenko, I.; Cao, Y.; Moskotin, M.; Principi, A.; Grigorieva, I. V.; Goltsman, G.; Fedorov, G.; Svintsov, D. Dual Origin of Room Temperature Sub-Terahertz Photoresponse in Graphene Field Effect Transistors. *Appl. Phys. Lett.* **2018**, *112*, doi:10.1063/1.5018151.
153. Jiang, Z.; Wang, Y.; Chen, L.; Yu, Y.; Yuan, S.; Deng, W.; Wang, R.; Wang, Z.; Yan, Q.; Wu, X.; et al. Antenna-Integrated Silicon-Plasmonic Graphene Sub-Terahertz Emitter. *APL Photonics* **2021**, *6*, doi:10.1063/5.0047070.
154. Balandin, A.A. Low-Frequency 1/f Noise in Graphene Devices. *Nat. Nanotechnol.* **2013**, *8*, 549–555, doi:10.1038/nnano.2013.144.
155. Langford, E. Quartiles in Elementary Statistics. *J. Stat. Educ.* **2006**, *14*, doi:10.1080/10691898.2006.11910589.
156. Kharche, N.; Nayak, S.K. Quasiparticle Band Gap Engineering of Graphene and Graphone on Hexagonal Boron Nitride Substrate. *Nano Lett.* **2011**, *11*, 5274–5278, doi:10.1021/nl202725w.

157. Cassabois, G.; Valvin, P.; Gil, B. Hexagonal Boron Nitride Is an Indirect Bandgap Semiconductor. *Nat. Photonics* **2016**, *10*, 262–266, doi:10.1038/nphoton.2015.277.

158. Massicotte, M. Ultrafast Optoelectronics in 2D Materials and Their Heterostructures, Universitat Politècnica de Catalunya, **2017**.

159. Xia, F.; Wang, H.; Xiao, D.; Dubey, M.; Ramasubramaniam, A. Two-Dimensional Material Nanophotonics. *Nat. Photonics* **2014**, *8*, 899–907, doi:10.1038/nphoton.2014.271.

160. Viti, L.; Asgari, M.; Riccardi, E.; Balci, O.; De Fazio, D.; Shinde, S.M.; Zhang, J.; Mignuzzi, S.; Koppens, F.H.L.; Ferrari, A.C.; et al. Chip-Scalable, Graphene-Based Terahertz Thermoelectric Photodetectors. In Proceedings of the 2022 47th International Conference on Infrared, Millimeter and Terahertz Waves (IRMMW-THz); 2022; pp. 1–2.

161. Tomadin, A.; Brida, D.; Cerullo, G.; Ferrari, A.C.; Polini, M. Nonequilibrium Dynamics of Photoexcited Electrons in Graphene: Collinear Scattering, Auger Processes, and the Impact of Screening. *Phys. Rev. B - Condens. Matter Mater. Phys.* **2013**, *88*, 1–18, doi:10.1103/PhysRevB.88.035430.

162. Tomadin, A.; Polini, M. Theory of the Effective Seebeck Coefficient for Photoexcited Two-Dimensional Materials: Graphene. *Phys. Rev. B* **2021**, *104*, 1–8, doi:10.1103/PhysRevB.104.125443.

163. Ravaro, M.; Locatelli, M.; Viti, L.; Ercolani, D.; Consolino, L.; Bartalini, S.; Sorba, L.; Vitiello, M.S.; De Natale, P. Detection of a 2.8 THz Quantum Cascade Laser with a Semiconductor Nanowire Field-Effect Transistor Coupled to a Bow-Tie Antenna. *Appl. Phys. Lett.* **2014**, *104*, 2–6, doi:10.1063/1.4867074.

164. Dayeh, S.A.; Aplin, D.P.R.; Zhou, X.; Yu, P.K.L.; Yu, E.T.; Wang, D. High Electron Mobility InAs Nanowire Field-Effect Transistors. *small* **2007**, *3*, 326–332.

165. Ford, A.C.; Johnny C., H.; Chueh, Y.L.; Tseng, Y.C.; Fan, Z.; Guo, J.; Bokor, J.; Javey, A. Diameter-Dependent Electron Mobility of Lnas Nanowires. *Nano Lett.* **2009**, *9*, 360–365, doi:10.1021/nl803154m.

166. Takahashi, T.; Takei, K.; Adabi, E.; Fan, Z.; Niknejad, A.M.; Javey, A. Parallel Array InAs Nanowire Transistors for Mechanically Bendable, Ultrahigh Frequency Electronics. *ACS Nano* **2010**, *4*, 5855–5860, doi:10.1021/nn1018329.

167. Pogna, E.A.A.; Asgari, M.; Zannier, V.; Sorba, L.; Viti, L.; Vitiello, M.S. Unveiling the Detection Dynamics of Semiconductor Nanowire Photodetectors by Terahertz Near-Field Nanoscopy. *Light Sci. Appl.* **2020**, *9*, 1–12, doi:10.1038/s41377-020-00425-1.

168. Asgari, M.; Viti, L.; Zannier, V.; Sorba, L.; Vitiello, M.S. Semiconductor Nanowire Field-Effect Transistors as Sensitive Detectors in the Far-Infrared. *Nanomaterials* **2021**, *11*, doi:10.3390/nano11123378.

169. Chen, X.; Liu, H.; Li, Q.; Chen, H.; Peng, R.; Chu, S.; Cheng, B. Terahertz Detectors Arrays Based on Orderly Aligned InN Nanowires. *Sci. Rep.* **2015**, *5*, doi:10.1038/srep13199.

170. Viti, L.; Vitiello, M.S.; Ercolani, D.; Sorba, L.; Tredicucci, A. Se-Doping Dependence of the Transport Properties in CBE-Grown InAs Nanowire Field Effect Transistors. *Nanoscale Res. Lett.* **2012**, *7*, 159, doi:10.1186/1556-276X-7-159.

171. Vitiello, M.S.; Viti, L.; Coquillat, D.; Knap, W.; Ercolani, D.; Sorba, L. One Dimensional Semiconductor Nanostructures: An Effective Active-Material for Terahertz Detection. *APL Mater.* **2015**, *3*, 26104.

172. Viti, L.; Coquillat, D.; Ercolani, D.; Sorba, L.; Knap, W.; Vitiello, M.S. Nanowire Terahertz Detectors with a Resonant Four-Leaf-Clover-Shaped Antenna. *Opt. Express* **2014**, *22*, 8996, doi:10.1364/oe.22.008996.

173. Erhard, N.; Seifert, P.; Prechtel, L.; Hertenberger, S.; Karl, H.; Abstreiter, G.; Koblmüller, G.; Holleitner, A.W. Ultrafast Photocurrents and THz Generation in Single InAs-Nanowires. *Ann. Phys.* **2013**, *525*, 180–188, doi:10.1002/andp.201200181.

174. Persson, A.I.; Fröberg, L.E.; Jeppesen, S.; Björk, M.T.; Samuelson, L. Surface Diffusion Effects on Growth of Nanowires by Chemical Beam Epitaxy. *J. Appl. Phys.* **2007**, *101*, doi:10.1063/1.2435800.

175. Ercolani, D.; Rossi, F.; Li, A.; Roddaro, S.; Grillo, V.; Salviati, G.; Beltram, F.; Sorba, L. InAs/InSb Nanowire Heterostructures Grown by Chemical Beam Epitaxy. *Nanotechnology* **2009**, *20*, doi:10.1088/0957-4484/20/50/505605.

176. Bazylewski, P.; Ezugwu, S.; Fanchini, G. A Review of Three-Dimensional Scanning near-Field Optical Microscopy (3D-SNOM) and Its Applications in Nanoscale Light Management. *Appl. Sci.* **2017**, *7*, doi:10.3390/app7100973.

177. M. M. Wiecha Terahertz Nano-Imaging with s-SNOM. In *Terahertz Technology*; intechopen: London, 2021.

178. Graham, R.; Miller, C.; Oh, E.; Yu, D. Electric Field Dependent Photocurrent Decay Length in Single Lead Sulfide Nanowire Field Effect Transistors. *Nano Lett.* **2010**, *11*, 717–722, doi:10.1021/nl1038456.

179. Arcangeli, A.; Rossella, F.; Tomadin, A.; Xu, J.; Ercolani, D.; Sorba, L.; Beltram, F.; Tredicucci, A.; Polini, M.; Roddaro, S. Gate-Tunable Spatial Modulation of Localized Plasmon Resonances. *Nano Lett.* **2016**, *16*, 5688–5693.

180. Allen, J.E.; Hemesath, E.R.; Lauhon, L.J. Scanning Photocurrent Microscopy Analysis of Si Nanowire Field-Effect Transistors Fabricated by Surface Etching of the Channel. *Nano Lett.* **2009**, *9*, 1903–1908.

181. Ahn, Y.; Dunning, J.; Park, J. Scanning Photocurrent Imaging and Electronic Band Studies in Silicon Nanowire Field Effect Transistors. *Nano Lett.* **2005**, *5*, 1367–1370.

182. Xia, F.; Mueller, T.; Golizadeh-Mojarad, R.; Freitag, M.; Lin, Y.; Tsang, J.; Perebeinos, V.; Avouris, P. Photocurrent Imaging and Efficient Photon Detection in a Graphene Transistor. *Nano Lett.* **2009**, *9*, 1039–1044.

183. Huber, A.J.; Keilmann, F.; Wittborn, J.; Aizpurua, J.; Hillenbrand, R. Terahertz Near-Field Nanoscopy of Mobile Carriers in Single Semiconductor Nanodevices. *Nano Lett.* **2008**, *8*, 3766–3770.

184. Stiegler, J.M.; Huber, A.J.; Diedenhofen, S.L.; Gomez Rivas, J.; Algra, R.E.; Bakkers, E.; Hillenbrand, R. Nanoscale Free-Carrier Profiling of Individual Semiconductor Nanowires by Infrared near-Field Nanoscopy. *Nano Lett.* **2010**, *10*, 1387–1392.

185. Berweger, S.; Blanchard, P.T.; Brubaker, M.D.; Coakley, K.J.; Sanford, N.A.; Wallis, T.M.; Bertness, K.A.; Kabos, P. Near-Field Control and Imaging of Free Charge Carrier Variations in GaN Nanowires. *Appl. Phys. Lett.* **2016**, *108*, 73101.

186. Liewald, C.; Mastel, S.; Hesler, J.; Huber, A.J.; Hillenbrand, R.; Keilmann, F. All-Electronic Terahertz Nanoscopy. *Optica* **2018**, *5*, 159–163.

187. Jung, L.; Pries, J.; Maß, T.W.W.; Lewin, M.; Boyuk, D.S.; Mohabir, A.T.; Filler, M.A.; Wuttig, M.; Taubner, T. Quantification of Carrier Density Gradients along Axially Doped Silicon Nanowires Using Infrared Nanoscopy. *ACS Photonics* **2019**, *6*, 1744–1754.

188. Kawata, S.; Ohtsu, M.; Irie, M. *Near-Field Optics and Surface Plasmon Polaritons*; Springer Science & Business Media, 2001; Vol. 81;.

189. Chen, J.; Badioli, M.; Alonso-González, P.; Thongrattanasiri, S.; Huth, F.; Osmond, J.; Spasenović, M.; Centeno, A.; Pesquera, A.; Godignon, P.; et al. Optical Nano-Imaging of Gate-Tunable Graphene Plasmons. *Nature* **2012**, *487*, 77–81, doi:10.1038/nature11254.

190. Fei, Z.; Andreev, O.G.O.; Bao, O.W.; Zhang, L.M.; Mcleod, A.S.; Wang, C.; Stewart, M.K.; Zhao, Z.; Dominguez, G.; Thiemens, M.; et al. Infrared Nanoscopy of Dirac Plasmons at the Graphene À SiO 2 Interface. **2011**, 4701–4705.

191. Fei, Z.; Rodin, A.S.; Andreev, G.O.; Bao, W.; McLeod, A.S.; Wagner, M.; Zhang, L.M.; Zhao, Z.; Thiemens, M.; Dominguez, G.; et al. Gate-Tuning of Graphene Plasmons Revealed by Infrared Nano-Imaging. *Nature* **2012**, *486*, 82–85, doi:10.1038/nature11253.

192. Li, P.; Lewin, M.; Kretinin, A. V; Caldwell, J.D.; Novoselov, K.S.; Taniguchi, T.; Watanabe, K.; Gaussmann, F.; Taubner, T. Hyperbolic Phonon-Polaritons in Boron Nitride for near-Field Optical Imaging and Focusing. *Nat. Commun.* **2015**, *6*, 7507.

193. Huber, A.; Ocelic, N.; Kazantsev, D.; Hillenbrand, R. Near-Field Imaging of Mid-Infrared Surface Phonon Polariton Propagation. *Appl. Phys. Lett.* **2005**, *87*, 081103, doi:10.1063/1.2032595.

194. Renger, J.; Grafström, S.; Eng, L.M.; Hillenbrand, R. Resonant Light Scattering by Near-Field-Induced Phonon Polaritons. *Phys. Rev. B - Condens. Matter Mater. Phys.* **2005**, *71*, 075410, doi:10.1103/PhysRevB.71.075410.

195. Low, T.; Chaves, A.; Caldwell, J.D.; Kumar, A.; Fang, N.X.; Avouris, P.; Heinz, T.F.; Guinea, F.; Martin-Moreno, L.; Koppens, F. Polaritons in Layered Two-Dimensional Materials. *Nat. Mater.* **2017**, *16*, 182.

196. Alonso-González, P.; Nikitin, A.Y.; Gao, Y.; Woessner, A.; Lundeberg, M.B.; Principi, A.; Forcellini, N.; Yan, W.; Vélez, S.; Huber, A.J.; et al. Acoustic Terahertz Graphene Plasmons Revealed by Photocurrent Nanoscopy. *Nat. Nanotechnol.* **2017**, *12*, 31–35, doi:10.1038/nnano.2016.185.
197. Schiefele, J.; Pedrós, J.; Sols, F.; Calle, F.; Guinea, F. Coupling Light into Graphene Plasmons through Surface Acoustic Waves. *Phys. Rev. Lett.* **2013**, *111*, 1–5, doi:10.1103/PhysRevLett.111.237405.
198. Hsu, J.W.P.; Fitzgerald, E.A.; Xie, Y.H.; Silverman, P.J. Near-Field Scanning Optical Microscopy Imaging of Individual Threading Dislocations on Relaxed Ge x Si1- x Films. *Appl. Phys. Lett.* **1994**, *65*, 344–346.
199. Buratto, S.K.; Hsu, J.W.P.; Trautman, J.K.; Betzig, E.; Bylsma, R.B.; Bahr, C.C.; Cardillo, M.J. Imaging InGaAsP Quantum-Well Lasers Using near-Field Scanning Optical Microscopy. *J. Appl. Phys.* **1994**, *76*, 7720–7725.
200. Grover, S.; Dubey, S.; Mathew, J.P.; Deshmukh, M.M. Limits on the Bolometric Response of Graphene Due to Flicker Noise. *Appl. Phys. Lett.* **2015**, *106*, 51113.
201. Woessner, A.; Alonso-González, P.; Lundeberg, M.B.; Gao, Y.; Barrios-Vargas, J.E.; Navickaite, G.; Ma, Q.; Janner, D.; Watanabe, K.; Cummings, A.W.; et al. Near-Field Photocurrent Nanoscopy on Bare and Encapsulated Graphene. *Nat. Commun.* **2016**, *7*, 10783.
202. Goldberg, B.B.; Unlu, M.S.; Herzog, W.D.; Ghaemi, H.F.; Towe, E. Near-Field Optical Studies of Semiconductor Heterostructures and Laser Diodes. *IEEE J. Sel. Top. Quantum Electron.* **1995**, *1*, 1073–1081.
203. Richter, A.; Tomm, J.W.; Lienau, C.; Luft, J. Optical Near-Field Photocurrent Spectroscopy: A New Technique for Analyzing Microscopic Aging Processes in Optoelectronic Devices. *Appl. Phys. Lett.* **1996**, *69*, 3981–3983.
204. McNeill, C.R.; Frohne, H.; Holdsworth, J.L.; Furst, J.E.; King, B. V; Dastoor, P.C. Direct Photocurrent Mapping of Organic Solar Cells Using a Near-Field Scanning Optical Microscope. *Nano Lett.* **2004**, *4*, 219–223.
205. Gu, Y.; Kwak, E.-S.; Lensch, J.L.; Allen, J.E.; Odom, T.W.; Lauhon, L.J. Near-Field Scanning Photocurrent Microscopy of a Nanowire Photodetector. *Appl. Phys. Lett.* **2005**, *87*, 43111.
206. Mueller, T.; Xia, F.; Freitag, M.; Tsang, J.; Avouris, P.; others Role of Contacts in Graphene Transistors: A Scanning Photocurrent Study. *Phys. Rev. B* **2009**, *79*, 245430.
207. Rauhut, N.; Engel, M.; Steiner, M.; Krupke, R.; Avouris, P.; Hartschuh, A. Antenna-Enhanced Photocurrent Microscopy on Single-Walled Carbon Nanotubes at 30 Nm Resolution. *ACS Nano* **2012**, *6*, 6416–6421.
208. Mauser, N.; Hartschuh, A. Tip-Enhanced near-Field Optical Microscopy. *Chem. Soc. Rev.* **2014**, *43*, 1248–1262.
209. Mauser, N.; Hartmann, N.; Hofmann, M.S.; Janik, J.; Hogele, A.; Hartschuh, A. Antenna-

Enhanced Optoelectronic Probing of Carbon Nanotubes. *Nano Lett.* **2014**, *14*, 3773–3778.

210. Wunnicke, O. Gate Capacitance of Back-Gated Nanowire Field-Effect Transistors. *Appl. Phys. Lett.* **2006**, *89*, 83102.
211. Keilmann, F.; Hillenbrand, R. Near-Field Microscopy by Elastic Light Scattering from a Tip. *Philos. Trans. R. Soc. London. Ser. A Math. Phys. Eng. Sci.* **2004**, *362*, 787–805.
212. Vurgaftman, I.; Meyer, J. áR; Ram-Mohan, L. áR Band Parameters for III--V Compound Semiconductors and Their Alloys. *J. Appl. Phys.* **2001**, *89*, 5815–5875.
213. Roddaro, S.; Ercolani, D.; Safeen, M.A.; Suomalainen, S.; Rossella, F.; Giazotto, F.; Sorba, L.; Beltram, F. Giant Thermovoltage in Single InAs Nanowire Field-Effect Transistors. *Nano Lett.* **2013**, *13*, 3638–3642.
214. Knoll, B.; Keilmann, F. Enhanced Dielectric Contrast in Scattering-Type Scanning near-Field Optical Microscopy. *Opt. Commun.* **2000**, *182*, 321–328, doi:10.1016/S0030-4018(00)00826-9.
215. Pogna, E.A.A.; Asgari, M.; Zannier, V.; Sorba, L.; Viti, L.; Vitiello, M.S. Tracing Photodetection of THz Frequency Light in InAs Nanowire Field Effect Transistors via Near-Field THz Nanoscopy. In Proceedings of the 2020 45th International Conference on Infrared, Millimeter, and Terahertz Waves (IRMMW-THz); 2020; p. 1.
216. Gupta, N.; Song, Y.; Holloway, G.W.; Sinha, U.; Haapamaki, C.M.; Lapierre, R.R.; Baugh, J. Temperature-Dependent Electron Mobility in InAs Nanowires. *Nanotechnology* **2013**, *24*, doi:10.1088/0957-4484/24/22/225202.
217. C. A. Balanis *Antenna Theory: Analysis and Design, 4th Ed*; Wiley: Hoboken, NJ, USA, 2016;
218. Javadi, E.; But, D.B.; Ikamas, K.; Zdanevičius, J.; Knap, W.; Lisauskas, A. Sensitivity of Field-Effect Transistor-Based Terahertz Detectors. *Sensors* **2021**, *21*, 1–20, doi:10.3390/s21092909.
219. Viti, L.; Hu, J.; Coquillat, D.; Politano, A.; Knap, W.; Vitiello, M.S. Efficient Terahertz Detection in Black-Phosphorus Nano-Transistors with Selective and Controllable Plasma-Wave, Bolometric and Thermoelectric Response. *Sci. Rep.* **2016**, *6*, 1–10, doi:10.1038/srep20474.
220. Asgari, M.; Coquillat, D.; Menichetti, G.; Zannier, V.; Diakonova, N.; Knap, W.; Sorba, L.; Viti, L.; Vitiello, M.S. Quantum-Dot Single-Electron Transistors as Thermoelectric Quantum Detectors at Terahertz Frequencies. *Nano Lett.* **2021**, *21*, 8587–8594, doi:10.1021/acs.nanolett.1c02022.
221. Chatterjee, A.; Stevenson, P.; De Franceschi, S.; Morello, A.; de Leon, N.P.; Kuemmeth, F. Semiconductor Qubits in Practice. *Nat. Rev. Phys.* **2021**, *3*, 157–177, doi:10.1038/s42254-021-00283-9.
222. Arakawa, Y.; Holmes, M.J. Progress in Quantum-Dot Single Photon Sources for Quantum Information Technologies: A Broad Spectrum Overview. *Appl. Phys. Rev.* **2020**, *7*, 021309,

doi:10.1063/5.0010193.

223. Sizov, F. Infrared and Terahertz in Application to Biomedicine. *Int. J. Biosens. Bioelectron.* **2018**, *4*, 134–136, doi:10.15406/ijbsbe.2018.04.00114.

224. Aboud, S.A.; Altemimi, A.B.; Al-hiiphy, A.R.S.; Yi-chen, L.; Cacciola, F. A Comprehensive Review on Infrared Heating. *Molecules* **2019**, *2*, 1–20.

225. Tonouchi, M. Cutting-Edge Terahertz Technology. *Nat. Photonics* **2007**, *1*, 97–105, doi:10.1038/nphoton.2007.3.

226. Tohmé, L.; Blin, S.; Ducournau, G.; Nouvel, P.; Coquillat, D.; Hisatake, S.; Nagatsuma, T.; Pénarier, A.; Varani, L.; Knap, W.; et al. Terahertz Wireless Communication Using GaAs Transistors as Detectors. *Electron. Lett.* **2014**, *50*, 323–325, doi:10.1049/el.2013.3702.

227. Mikio, A.R.A.; Makoto, A.; Masahide, S. Study for Far-Infrared and Faint Light. *J. Natl. Inst. Inf. Commun. Technol.* **2004**, *51*, 51–58.

228. B. S. Karasik, A.V.S. and D.E.P. Nanobolometers for THz Photon Detection. *IEEE Trans. Terahertz Sci. Technol.* **2011**, *1*, 97–111.

229. Livache, C.; Martinez, B.; Goubet, N.; Gréboval, C.; Qu, J.; Chu, A.; Royer, S.; Ithurria, S.; Silly, M.G.; Dubertret, B.; et al. A Colloidal Quantum Dot Infrared Photodetector and Its Use for Intraband Detection. *Nat. Commun.* **2019**, *10*, 1–10, doi:10.1038/s41467-019-10170-8.

230. Rogalski, A. Quantum Well Photoconductors in Infrared Detector Technology. *J. Appl. Phys.* **2003**, *93*, 4355–4391, doi:10.1063/1.1558224.

231. Ueda, T.; An, Z.; Hirakawa, K.; Komiyama, S. Charge-Sensitive Infrared Phototransistors: Characterization by an All-Cryogenic Spectrometer. *J. Appl. Phys.* **2008**, *103*, 093109, doi:10.1063/1.2919779.

232. Loch, M.; Widenhorn, R.; Bodegom, E. Infrared Response of Charge-Coupled Devices. *Sensors Camera Syst. Sci. Ind. Appl. VI* **2005**, *5677*, 201, doi:10.1117/12.610650.

233. Nadeev, A.I.; Razenkov, I.A.; Shelefontyuk, D.I.; Shevtsov, E.S. Comparison of an Avalanche Photodiode and a Photomultiplier Tube as Photodetectors of Near-Infrared Radiation in the Photon-Counting Mode. *Instruments Exp. Tech.* **2018**, *61*, 377–381, doi:10.1134/S0020441218020057.

234. Schneider, H.; Maier, T.; Liu, H.C.; Walther, M.; Koidl, P. Ultrasensitive Femtosecond Two-Photon Detector with Resonantly Enhanced Nonlinear Absorption. *Opt. Lett.* **2005**, *30*, 287, doi:10.1364/ol.30.000287.

235. Sizov, F. Terahertz Radiation Detectors: The State-of-the-Art. *Semicond. Sci. Technol.* **2018**, *33*, 123001, doi:10.1088/1361-6641/aae473.

236. Liu, H.C.; Song, C.Y.; SpringThorpe, A.J.; Cao, J.C. Terahertz Quantum-Well Photodetector. *Appl. Phys. Lett.* **2004**, *84*, 4068–4070, doi:10.1063/1.1751620.

237. Palaferri, D.; Todorov, Y.; Chen, Y.N.; Madeo, J.; Vasanelli, A.; Li, L.H.; Davies, A.G.; Linfield, E.H.; Sirtori, C. Patch Antenna Terahertz Photodetectors. *Appl. Phys. Lett.* **2015**, *106*,

1–6, doi:10.1063/1.4918983.

238. Mathieu Jeannin, Thomas Bonazzi, Djamal Gacemi, Angela Vasanelli, Stéphan Suffit, Lianhe Li, Alexander Giles Davies, Edmund Linfield, Carlo Sirtori, and Y.T. High Temperature Metamaterial Terahertz Quantum Detector. *Appl. Phys. Lett.* **2020**, *117*, 251102, doi:https://doi.org/10.1063/5.0033367.

239. Paulillo, B.; Pirotta, S.; Nong, H.; Crozat, P.; Guilet, S.; Xu, G.; Dhillon, S.; Li, L.H.; Davies, A.G.; Linfield, E.H.; et al. Ultrafast Terahertz Detectors Based on Three-Dimensional Meta-Atoms. *Optica* **2018**, *4*, 1451–1456, doi:10.1364/optica.4.001451.

240. Webster, J.G.; Perera, A.G.U.; Ariyawansa, G. Epitaxial Quantum Dot Infrared Photodetectors. *Wiley Encycl. Electr. Electron. Eng.* **2014**, 1–30, doi:10.1002/047134608x.w8218.

241. Gunapala, S.D.; Bandara, S. V.; Rafol, S.B.; Ting, D.Z. Quantum Well Infrared Photodetectors. *Semicond. Semimetals* **2011**, *84*, 59–151, doi:10.1016/B978-0-12-381337-4.00002-4.

242. Phillips, J.; Kamath, K.; Bhattacharya, P. Far-Infrared Photoconductivity in Self-Organized InAs Quantum Dots. *Appl. Phys. Lett.* **1998**, *72*, 2020–2022, doi:10.1063/1.121252.

243. Urayama, J.; Norris, T.B.; Singh, J.; Bhattacharya, P. Observation of Phonon Bottleneck in Quantum Dot Electronic Relaxation. *Phys. Rev. Lett.* **2001**, *86*, 4930–4933, doi:10.1103/PhysRevLett.86.4930.

244. Bimberg, D. Quantum Dots: Paradigm Changes in Semiconductor Physics. *Semiconductors* **1999**, *33*, 951–955, doi:10.1134/1.1187810.

245. Barve, A. V.; Krishna, S. *Quantum Dot Infrared Photodetectors*; Elsevier Inc., 2011; Vol. 84; ISBN 9780123813374.

246. Kadow, C.; Jackson, A.W.; Gossard, A.C.; Matsuura, S.; Blake, G.A. Self-Assembled ErAs Islands in GaAs for Optical-Heterodyne THz Generation. *Appl. Phys. Lett.* **2000**, *76*, 3510–3512, doi:10.1063/1.126690.

247. Kleinschmidt, P.; Giblin, S.P.; Antonov, V.; Hashiba, H.; Kulik, L.; Tzalenchuk, A.; Komiyama, S. A Highly Sensitive Detector for Radiation in the Terahertz Region. *IEEE Trans. Instrum. Meas.* **2007**, *56*, 463–467, doi:10.1109/TIM.2007.891146.

248. Riccardi, E.; Massabeau, S.; Valmorra, F.; Messelot, S.; Rosticher, M.; Tignon, J.; Watanabe, K.; Taniguchi, T.; Delbecq, M.; Dhillon, S.; et al. Ultrasensitive Photoresponse of Graphene Quantum Dots in the Coulomb Blockade Regime to THz Radiation. *Nano Lett.* **2020**, *20*, 5408–5414, doi:10.1021/acs.nanolett.0c01800.

249. Sadre Momtaz, Z.; Servino, S.; Demontis, V.; Zannier, V.; Ercolani, D.; Rossi, F.; Rossella, F.; Sorba, L.; Beltram, F.; Roddaro, S. Orbital Tuning of Tunnel Coupling in InAs/InP Nanowire Quantum Dots. *Nano Lett.* **2020**, *20*, 1693–1699, doi:10.1021/acs.nanolett.9b04850.

250. Romeo, L.; Roddaro, S.; Pitanti, A.; Ercolani, D.; Sorba, L.; Beltram, F. Electrostatic Spin

Control in InAs/InP Nanowire Quantum Dots. *Nano Lett.* **2012**, *12*, 4490–4494, doi:10.1021/nl301497j.

251. Pfund, A.; Shorubalko, I.; Leturcq, R.; Ensslin, K. Top-Gate Defined Double Quantum Dots in InAs Nanowires. *Appl. Phys. Lett.* **2006**, *89*, 252106, doi:10.1063/1.2409625.

252. Prete, D.; Erdman, P.A.; Demontis, V.; Zannier, V.; Ercolani, D.; Sorba, L.; Beltram, F.; Rossella, F.; Taddei, F.; Roddaro, S. Thermoelectric Conversion at 30 K in InAs/InP Nanowire Quantum Dots. *Nano Lett.* **2019**, *19*, 3033–3039, doi:10.1021/acs.nanolett.9b00276.

253. Kleinschmidt, P.; Giblin, S.; Tzalenchuk, A.; Hashiba, H.; Antonov, V.; Komiyama, S. Sensitive Detector for a Passive Terahertz Imager. *J. Appl. Phys.* **2006**, *99*, 114504, doi:10.1063/1.2199107.

254. Thomas, F.S.; Baumgartner, A.; Gubser, L.; Jünger, C.; Fülöp, G.; Nilsson, M.; Rossi, F.; Zannier, V.; Sorba, L.; Schönenberger, C. Highly Symmetric and Tunable Tunnel Couplings in InAs/InP Nanowire Heterostructure Quantum Dots. *Nanotechnology* **2020**, *31*, 135003, doi:10.1088/1361-6528/ab5ce6.

255. Romeo, L. Semiconductor Nanowires : The Building Block for next Generation Electronics and Photonics Candidate, Sciola Normale Superiore, 2014.

256. Riccardi, E.; Massabeau, S.; Valmorra, F.; Messelot, S.; Rosticher, M.; Tignon, J.; Watanabe, K.; Taniguchi, T.; Delbecq, M.; Dhillon, S.; et al. Ultrasensitive Photoresponse of Graphene Quantum Dots in the Coulomb Blockade Regime to THz Radiation. *Nano Lett.* **2020**, *20*, 5408–5414, doi:10.1021/acs.nanolett.0c01800.

257. Rinzan, M.; Jenkins, G.; Drew, H.D.; Shafranjuk, S.; Barbara, P. Carbon Nanotube Quantum Dots as Highly Sensitive Terahertz-Cooled Spectrometers. *Nano Lett.* **2012**, *12*, 3097–3100, doi:10.1021/nl300975h.

258. H. Schneider. et al. Terahertz Two-Photon Quantum Well Infrared Photodetector. *Opt. Express* **2009**, *17*, 12279–12284, doi:10.1364/OE.17.012929.

259. Asgari, M.; Coquillat, D.; Menichetti, G.; Zannier, V.; Dyakonova, N.; Knap, W.; Sorba, L.; Viti, L.; Serena Vitiello, M. Highly Sensitive Photodetectors at 0.6 THz Based on Quantum Dot Single Electron Transistors. In Proceedings of the 2021 46th International Conference on Infrared, Millimeter and Terahertz Waves (IRMMW-THz); 2021; pp. 1–2.

260. Datta, S.; van Houten, H. Electronic Transport in Mesoscopic Systems . *Phys. Today* **1996**, *49*, 70–70, doi:10.1063/1.2807624.

261. Butcher, P.N. Thermal and Electrical Transport Formalism for Electronic Microstructures with Many Terminals. *J. Phys. Condens. Matter* **1990**, *2*, 4869–4878, doi:10.1088/0953-8984/2/22/008.

262. Ferry, D.K.; Goodnick, S.M.; Bird, J. Transport in Nanostructures. *Transp. Nanostructures* **2009**, 1–659, doi:10.1017/CBO9780511840463.

263. Bevilacqua, G.; Grosso, G.; Menichetti, G.; Pastori Parravicini, G. Thermoelectric Efficiency

of Nanoscale Devices in the Linear Regime. *Phys. Rev. B* **2016**, *94*, 1–14, doi:10.1103/PhysRevB.94.245419.

264. Menichetti, G.; Grosso, G.; Parravicini, G.P. Analytic Treatment of the Thermoelectric Properties for Two Coupled Quantum Dots Threaded by Magnetic Fields. *J. Phys. Commun.* **2018**, *2*, 055026, doi:10.1088/2399-6528/aac423.
265. Mani, P.; Nakpathomkun, N.; Linke, H. Intrinsic Seebeck Coefficient of Quantum Dots. *J. Electron. Mater.* **2009**, *38*, 1163–1165, doi:10.1007/s11664-009-0691-9.
266. Talbo, V.; Saint-Martin, J.; Retailleau, S.; Dollfus, P. Non-Linear Effects and Thermoelectric Efficiency of Quantum Dot-Based Single-Electron Transistors. *Sci. Rep.* **2017**, *7*, 1–13, doi:10.1038/s41598-017-14009-4.
267. Svilans, A.; Leijnse, M.; Linke, H. Experiments on the Thermoelectric Properties of Quantum Dots. *Comptes Rendus Phys.* **2016**, *17*, 1096–1108, doi:10.1016/j.crhy.2016.08.002.
268. Zannier, V.; Rossi, F.; Dubrovskii, V.G.; Ercolani, D.; Battiato, S.; Sorba, L. Nanoparticle Stability in Axial InAs-InP Nanowire Heterostructures with Atomically Sharp Interfaces. *Nano Lett.* **2018**, *18*, 167–174, doi:10.1021/acs.nanolett.7b03742.
269. Zannier, V.; Rossi, F.; Ercolani, D.; Sorba, L. Growth Dynamics of InAs/InP Nanowire Heterostructures by Au-Assisted Chemical Beam Epitaxy. *Nanotechnology* **2019**, *30*, 094003, doi:10.1088/1361-6528/aaf7ab.
270. Persson, A.I.; Björk, M.T.; Jeppesen, S.; Wagner, J.B.; Wallenberg, L.R.; Samuelson, L. InAs1-XPx Nanowires for Device Engineering. *Nano Lett.* **2006**, *6*, 403–407, doi:10.1021/nl052181e.
271. Hjort, M.; Lehmann, S.; Knutsson, J.; Zakharov, A.A.; Du, Y.A.; Sakong, S.; Timm, R.; Nylund, G.; Lundgren, E.; Kratzer, P.; et al. Electronic and Structural Differences between Wurtzite and Zinc Blende Inas Nanowire Surfaces: Experiment and Theory. *ACS Nano* **2014**, *8*, 12346–12355, doi:10.1021/nn504795v.
272. Liu, D. (Ohio S.U.;) Design, Fabrication and Chracterization of InAlAs/InGaAs/InAsP Composite Channel HEMTS, 2008.
273. Kouwenhoven, L.P.; Jauhar, S.; Orenstein, J.; McEuen, P.L.; Nagamune, Y.; Motohisa, J.; Sakaki, H. Observation of Photon-Assisted Tunneling through a Quantum Dot. *Phys. Rev. Lett.* **1994**, *73*, 3443–3446, doi:10.1103/PhysRevLett.73.3443.
274. Hanson, R.; Kouwenhoven, L.P.; Petta, J.R.; Tarucha, S.; Vandersypen, L.M.K. Spins in Few-Electron Quantum Dots. *Rev. Mod. Phys.* **2007**, *79*, 1217–1265, doi:10.1103/RevModPhys.79.1217.
275. El Fatimy, A.; Myers-Ward, R.L.; Boyd, A.K.; Daniels, K.M.; Gaskill, D.K.; Barbara, P. Epitaxial Graphene Quantum Dots for High-Performance Terahertz Bolometers. *Nat. Nanotechnol.* **2016**, *11*, 335–338, doi:10.1038/nnano.2015.303.
276. Eisele, M.; Cocker, T.L.; Huber, M.A.; Plankl, M.; Viti, L.; Ercolani, D.; Sorba, L.; Vitiello,

M.S.; Huber, R. Ultrafast Multi-Terahertz Nano-Spectroscopy with Sub-Cycle Temporal Resolution. *Nat. Photonics* **2014**, *8*, 841–845, doi:10.1038/nphoton.2014.225.

277. Dutta, B.; Majidi, D.; García Corral, A.; Erdman, P.A.; Florens, S.; Costi, T.A.; Courtois, H.; Winkelmann, C.B. Direct Probe of the Seebeck Coefficient in a Kondo-Correlated Single-Quantum-Dot Transistor. *Nano Lett.* **2019**, *19*, 506–511, doi:10.1021/acs.nanolett.8b04398.
278. E. L. Dereniak, G.D.B. *Infrared Detectors and Systems*; Wiley: New York, 1996; ISBN 978-0-471-12209-8.
279. Weidmann, D.; Tittel, F.K.; Aellen, T.; Beck, M.; Hofstetter, D.; Faist, J.; Blaser, S. Mid-Infrared Trace-Gas Sensing with a Quasi-Continuous-Wave Peltier-Cooled Distributed Feedback Quantum Cascade Laser. *Appl. Phys. B Lasers Opt.* **2004**, *79*, 907–913, doi:10.1007/s00340-004-1634-z.
280. Rosencher, A.E.; Fiore, A.; Vinter, B.; Berger, V.; Bois, P.; Nagle, J. Quantum Engineering of Optical Nonlinearities Published by : American Association for the Advancement of Science Quantum Engineering of Optical Nonlinearities. **1996**, *271*, 168–173.
281. Gmachl, C.; Malis, O.; Belyanin, A. Optical Nonlinearities in Intersubband Transitions and Quantum Cascade Lasers. In *Intersubband Transitions In Quantum Structures*; Paiella, R., Ed.; McGraw-Hill Education: New York, 2006 ISBN 9780071457927.
282. Dhillon, S.S.; Sirtori, C.; Alton, J.; Barbieri, S.; de Rossi, A.; Beere, H.E.; Ritchie, D.A. Terahertz Transfer onto a Telecom Optical Carrier. *Nat. Photonics* **2007**, *1*, 411–415, doi:10.1038/nphoton.2007.94.
283. Schneider, H.; Maier, T.; Liu, H.C.; Walther, M. Two-Photon Photocurrent Autocorrelation Using Intersubband Transitions at Nearly-Resonant Excitation. *Opt. Express* **2008**, *16*, 1523, doi:10.1364/oe.16.001523.
284. Schneider, H.; Drachenko, O.; Winnerl, S.; Helm, M.; Walther, M. Quadratic Autocorrelation of Free-Electron Laser Radiation and Photocurrent Saturation in Two-Photon Quantum Well Infrared Photodetectors. *Appl. Phys. Lett.* **2006**, *89*, doi:10.1063/1.2357936.
285. Paiella, R.; Capasso, F.; Gmachl, C.; Sivco, D.L.; Baillargeon, J.N.; Hutchinson, A.L.; Cho, A.Y.; Liu, H.C. Self-Mode-Locking of Quantum Cascade Lasers with Giant Ultrafast Optical Nonlinearities. *Science (80-.).* **2000**, *290*, 1739–1742, doi:10.1126/science.290.5497.1739.
286. Gordon, A.; Wang, C.Y.; Diehl, L.; Kärtner, F.X.; Belyanin, A.; Bour, D.; Corzine, S.; Höfler, G.; Liu, H.C.; Schneider, H.; et al. Multimode Regimes in Quantum Cascade Lasers: From Coherent Instabilities to Spatial Hole Burning. *Phys. Rev. A - At. Mol. Opt. Phys.* **2008**, *77*, 1–18, doi:10.1103/PhysRevA.77.053804.
287. Wang, C.Y.; Kuznetsova, L.; Diehl, L.; Kärtner, F.; Belkin, M.A.; Schneider, H.; Liu, H.C.; Capasso, F. Stable Mode-Locked Pulses from Mid-Infrared Quantum Cascade Lasers. In Proceedings of the Conference on Lasers and Electro-Optics/Quantum Electronics and Laser Science Conference and Photonic Applications Systems Technologies; Optica Publishing

Group: San Jose, California, 2008; p. CPDA11.

288. Schneider, H.; Maier, T.; Walther, M.; Liu, H.C. Two-Photon Photocurrent Spectroscopy of Electron Intersubband Relaxation and Dephasing in Quantum Wells. *Appl. Phys. Lett.* **2007**, *91*, 8–11, doi:10.1063/1.2806963.
289. Williams, B.S. Terahertz Quantum-Cascade Lasers. *Nat. Photonics* **2007**, *1*, 517–525, doi:10.1038/nphoton.2007.166.
290. Luo, H.; Liu, H.C.; Song, C.Y.; Wasilewski, Z.R. Background-Limited Terahertz Quantum-Well Photodetector. *Appl. Phys. Lett.* **2005**, *86*, 1–3, doi:10.1063/1.1947377.
291. Tonouchi, M. Cutting-Edge Terahertz Technology. *Nat. Photonics* **2007**, *1*, 97–105, doi:doi.org/10.1038/nphoton.2007.3.
292. Jiang, X.; Li, S.S.; Tidrow, M.Z. Study of Intersubband Transition in Quantum Dots and Quantum Dot Infrared Photodetectors. *Phys. E Low-Dimensional Syst. Nanostructures* **1999**, *5*, 27–35, doi:10.1016/S1386-9477(99)00026-0.
293. Levine, B.F. Quantum-Well Infrared Photodetectors. *J. Appl. Phys.* **1993**, *74*, doi:10.1063/1.354252.
294. Tang, S.; Chen, T.; Lin, S.; Tu, H. Intersubband Transitions in the Quantum Dot Layers for Quantum Confined Intersubband Transitions in the Quantum Dot Layers for Quantum Confined Photodetector. **2010**, doi:10.5772/8860.
295. Asuero, A.G.; Sayago, A.; González, A.G. The Correlation Coefficient: An Overview. *Crit. Rev. Anal. Chem.* **2006**, *36*, 41–59, doi:10.1080/10408340500526766.

Acknowledgements

As with any piece of research that results in the production of a thesis, on the cover there should be not only the name of the researcher, but also the names of all those unsung heroes, those who to varying degrees provided assistance, encouragement and guidance, and without whom I would not have succeeded. I am very grateful to all those people, my heroes, who have given me so much of their time, love and energy. There are so many people I would like to thank. I am so grateful for the time these people have given me to produce this thesis and finish my doctorate. Firstly, I must thank my supervisor at Scuola Normale Superiore, Professor Miriam Serena Vitiello for her infinite help, support, mastery, and effort throughout this process. Secondly, I must thank my scientific trainer and senior colleague Leonardo Viti who stood with me for entire duration of my PhD without whom it was impossible to achieve this goal. Finally, without the support and love of my family and friends I know I could not have accomplished this thesis. Significantly, an enormous thanks must go to my parents and unique sister who are literally my soul, and I am most indebted to them not only for my PhD, but also for entire my life. I am also most grateful to my lovely wife Somayeh Asadi who has brought love, strength, passion and bravery to my life and paved for me all this way long step-by-step and patiently. The last but not the least, a big thanks should be dedicated to those friends who have never left me alone in the ups-and-downs of this unforgettable way, especially Riccardo Nifosi, Omer Arif, Neeraj Mishra, Tohid Farajollahpour, Ayush Tyagi, and Guido Menichetti.